NMR STUDY ON Mn (II) CONTAMINANTS on LITHIUM-ION BATTERIES

NMR Studies of the Impact of Mn(II) contaminants on Electrolyte Dynamics in Manganese-Rich Lithium Ion Batteries using both Diffusometry and *Operando* Spectroscopy Methods

BY RUNZE ZHENG, B.SC

A Thesis Submitted to the School of Graduate Studies in Partial Fulfillment of the Requirements for the Degree Master of Science

Lay Abstract

The increasing maturity of lithium battery technology has also promoted the advancement of the electric vehicle manufacturing industry. As an excellent new energy material, the application and development of lithium batteries will be the main trend in the future. However, while improving battery capacity and energy density, lithium batteries also face many challenges.

The entire thesis work discusses how electrolyte degradation at high temperatures and high voltages accelerates the dissolution of transition metal manganese ions in NMC materials. The dissolution of manganese ions into the electrolyte creates a competitive effect with lithium ions, thereby reducing the performance of lithium batteries. Here, NMR technology was used to measure the negative effect of manganese ions on the self-diffusion coefficient of lithium ions in the electrolyte. Additionally, a set of *operando* experiments conducted at different discharge rates demonstrated the changes in mossy lithium and the solid electrolyte interface during the charge and discharge phases caused by pulse discharge. This also proved that such experimental designs can track the impact of manganese ions on the solid electrolyte interface and test the dissolution behavior and impact of manganese ions under different charge and discharge rates.

Abstract

Nickel-manganese-cobalt oxide (NMC) cathode materials have been applied in most Li-ion batteries, but there are nevertheless some concerns regarding the stability of this material. High voltage and high temperature during charging have been shown to accelerate the dissolution of NMC due to the release of more acidic components because of rapid electrolyte decomposition. Mn-contaminants ($Mn^{2+)}$ are hypothesized to diminish the diffusion coefficient of Li^+ in the electrolyte attributed to the competitive interaction between Mn^{2+} ions and Li^+ ions. With characterizations including ^7Li and ^1H pulsed field-gradient nuclear magnetic resonance (PFG-NMR) spectroscopy, we demonstrated the Mn (II)-contaminants effect on diffusion coefficient on Li^+ dynamics. Under the influence of deliberate manganese salt-additive to the electrolyte, the coin cell shows a capacity fading and unstable charging behavior. The PFG-NMR measurements also validated our hypotheses, as the results showing that Mn-containment causes decrease ~15% in the diffusion coefficient on Li-self diffusion. The activation energy for lithium-ion transport over the temperature range of (273 K - 303 K), was not changed by the presence of the Mn-contaminant electrolyte, which indicates the Mn (II) does not affect the Li-ion transport mechanism. The relative test also includes comparisons with other contamination, such as iron contamination from stain-less steels spacers and copper contamination from the current collector. Additionally, the lithium self-diffusion coefficient was tested before and after charging using a full battery configuration. In electrolytes containing manganese contaminants, a more significant decrease in the diffusion coefficient was observed after charging. Ideally, *operando* experiments can be used to observe the impact of manganese ions on the SEI. By combining both types of experiments, a closer approximation to the actual application conditions of market-used batteries can be achieved.

Acknowledgment

First, I would like to thank my advisor, Dr. Gillian Goward, for her guidance and support. She has continually guided me on how to think, write, and understand problems, not only in the lab but also in choosing research topics. Most importantly, I am grateful to her for giving me the opportunity to delve deeper into my interests in nuclear magnetic resonance and batteries, and for helping me achieve a deeper understanding in the field of chemistry.

Additionally, I would like to thank my other committee member, Dr. Yurij Mozharivskyj, for teaching me solid-state knowledge. This has effectively helped me understand the paramagnetic effects involved in my thesis topic related to lithium and has also enabled me to analyze some uncertain behaviors.

I want to thank all the members of my group for their support. I really enjoy the feeling of presenting in the group; every time, I can confidently showcase my experimental results and receive many insightful suggestions for my experiments. I am also grateful for everyone's help and guidance during my experiments. When I first joined the group, it was thanks to your assistance that I was able to integrate smoothly.

Most importantly, I want to thank Dr. Mengyang and Dr. Kevin Sander from our group for their guidance. I am grateful for their exhaustive teaching of NMR knowledge and their tireless help in solving problems during my NMR experiments.

I also want to thank my parents and my girlfriend. Their support has been my motivation to persevere. My parents' trust and my girlfriend's companionship have been a tremendous source of encouragement over the past two years.

Table of Content

List of figures

List of Table

List of Nomenclature

B_0	Applied magnetic field along the z-axis
E_a	Activation energy
ΔE	Energy difference between the ground and excited state
BMS	Bulk magnetic susceptibility (in chapter 2) Battery management system (in chapter 4)
BOD	Bottom of Discharge
CC	Constant current
CEI	Cathode-electrolyte interphase
CV	Constant Voltage
D	Diffusion coefficient
DFT	Density functional theory
DMC	Dimethyl Carbonate
EC	Ethylene Carbonate
ESI-MS	Electrospray ionization – mass spectrometry
EV	Electric Vehicle
FID	Free Induction decay
I	Spin quantum number

LFP	Lithium Iron Phosphate
LIB	Lithium Ion Battery
NMC	Nickel manganese cobalt oxide
NMR	Nuclear Magnetic resonance
OCV	Open circuit Voltage
PD	Pulse Discharge
PEEK	Polyetheretherketone
PFG-NMR	Pulse Field Gradient-NMR
RF	Radio frequency
SE	Spin-echo
SEI	Solid-Electrolyte interphase
TOC	Top of Charge
M	magnetization

Declaration of Academic Achievement

Kevin J. Sanders designed and operand the cartridge cell mentioned in Chapter 4. Mengyang Cui helped with NMR experiment set-up mentioned in Chapter 3. ssNake plotting script is written by Alexander Berno. Both Chapter 3 and Chapter 4 tested materials are prepared by Runze Zheng. All the data acquiring, and processing is done by Runze Zheng

Chapter1

Introduction

1.1 Background & Motivation

Since their development, lithium batteries have seen continuous advancements and breakthroughs in both materials and applications. The high energy density and stability of lithium batteries have made them integral to various aspects of daily life, including electric vehicles (EVs), mobile phones, and electronic devices. Although the production of EVs[1,2], particularly the batteries, can consume a significant amount of energy and result in higher initial emissions, studies show that over the entire lifecycle of the vehicle, electric vehicles generally produce fewer total emissions compared to conventional vehicles. Data released by various countries indicate a noticeable decrease in greenhouse gas emissions since 2020, underscoring the environmental benefits of transitioning to electric mobility[3,4].

In addition, the advancement of lithium battery technology has also driven the development of energy storage systems for renewable energy. For example, solar and wind power generation is intermittent and unstable, but lithium batteries can effectively store excess electricity and provide a stable power supply during peak demand periods. This not only improves energy utilization efficiency but also reduces dependence on fossil fuels, further lowering carbon emissions.

Lithium batteries are secondary batteries that rely on the movement of Li^+ ions between the positive and negative electrodes to complete the charge and discharge process. Lithium batteries exhibit excellent performance. Common types of secondary batteries include lithium batteries, lead-acid batteries, nickel-cadmium batteries, and nickel-metal hydride batteries. Compared to other secondary batteries, lithium batteries have a higher energy density and longer cycle life. The energy density can reach 100-200 Wh/kg, and the cycle life exceeds 1000

cycles, far surpassing other secondary batteries. Additionally, lithium batteries offer advantages such as fast charging, high-power discharge, and good environmental performance.

Moreover, with the advancement of technology, the recycling and reuse of lithium batteries are constantly improving, reducing the potential environmental hazards of lithium batteries. By cycling valuable metals such as lithium, cobalt, and nickel, not only does this contribute to the sustainable use of resources, but it also lowers the production cost of batteries and the demand for raw materials.

With the maturation of lithium battery technology, various advanced experimental instruments are being used to characterize lithium battery materials. Nuclear Magnetic Resonance (NMR) spectroscopy, X-ray spectroscopy, and X-ray diffraction (XRD) are widely employed to observe the chemical changes in lithium batteries. Among them, NMR is a particularly powerful experimental method. It can be used to observe both liquid-electrolyte batteries and the developing all-solid-state batteries through different NMR experiments. Additionally, advanced NMR experiments can also image the internal environment of the battery.

However, there are still many inherent issues with lithium batteries that need to be addressed. For example, controlling the degradation of electrolytes and the growth of various solid electrolyte interphases (SEI) layers[5,6] are ongoing challenges. These issues can affect the battery's performance, longevity, and safety[7,8].

1.2 Li-Ion Batteries

Lithium-ion batteries are composed of several key components: two electrodes (cathode, or positive electrode, and anode, or negative electrode), electrolyte, and separator. Common cathode materials include NMC (Nickel Manganese Cobalt), LFP (Lithium Iron Phosphate), and LMO (Lithium Manganese Oxide)[9]. The typical anode material is graphite, while lithium metal is used as anode in half-cell setups. The separator is typically made of polyolefin microporous membranes such as PE (Polyethylene), PP (Polypropylene), or their composite membranes. Electrolytes are classified into two types: solid-state and liquid. Solid-state electrolytes are

usually polymers or fully solid oxides or sulfides. Liquid electrolytes often use a mixed solvent system with $LiPF_6$ in ethylene carbonate, propylene carbonate, and low-viscosity dimethyl carbonate.

Different cathode materials offer varying energy densities, stabilities, and lifespans, but the fundamental operation of a lithium battery remains the redox (reduction-oxidation) reactions of lithium ions. When the battery charges, lithium ions are released from the cathode and move through the electrolyte to the anode. The anode, typically made of graphite with a layered structure, contains many micropores where provide space for lithium ions to embed (intercalation process). The more lithium ions embedded, the higher the charging capacity. Conversely, during discharge (when the battery is in use), the embedded lithium ions leave the graphite and return to the cathode. The more lithium ions that return to the cathode, the higher the discharge capacity. To illustrate, in electric vehicles, lithium batteries discharge to convert electrical energy into mechanical energy to power the vehicle (lithium ions move from the anode to the cathode), and charging returns the lithium ions to their original state at the cathode[10,11]. Table 1 shows that manganese-rich cathode materials (NMC LMO) have significant advantages in cost and application. Additionally, compared to other transition metals, manganese ions are relatively cheaper[12].

Cathode Material	Energy Density (Wh/kg)	Cycle Life (cycles)	Thermal Stability	Cost	Common Applications
Lithium Cobalt Oxide (LCO)	150-200	500-1000	Moderate	High	Mobile phones, laptops
Lithium Manganese Oxide (LMO)	100-150	300-700	High	Moderate	Power tools, medical devices
Lithium Iron Phosphate (LFP)	90-120	1000-2000	Very High	Low	Electric buses, grid storage
Lithium Nickel Manganese Cobalt Oxide (NMC)	150-220	1000-2000	Moderate to High	Moderate	Electric vehicles, energy storage
Lithium Nickel Cobalt Aluminum Oxide (NCA)	200-250	500-1000	Moderate	High	Electric vehicles

Table 1. Performance Comparison of Popular Cathode Materials on the Market

Charging Process:

- **Cathode Reaction (Oxidation Reaction)**:

$$LiCoO_2 \rightarrow Li_{1-x}CoO_2 + xLi^+ + xe^- \quad (1.1)$$

- **Anode Reaction (Reduction Reaction)**:

$$xLi^+ + xe^- + C \rightarrow Li_xC \quad (1.2)$$

Discharging Process:

- **Cathode Reaction (Reduction Reaction)**:

$$Li_{1-x}CoO_2 + xLi^+ + xe^- \rightarrow LiCoO_2 \quad (1.3)$$

- **Anode Reaction (Oxidation Reaction)**:

$$Li_xC \rightarrow C + xLi^+ + xe^- \quad (1.4)$$

Battery health has become a significant concern as lithium batteries are widely used in electronic products. Common issues with lithium batteries include poor stability, flammability, risk of explosion, excessive growth of lithium dendrites leading to short circuits, electrolyte degradation, and the growth of solid electrolyte interphases, which affect battery life. The first two problems are more understandable and are common with liquid electrolytes.

Figure 1 Components of Rechargeable Li-ion Batteries. Reprinted with permission from Reverse Engineering, 2018, 204. Copyright © March 2018, Nature Electronics

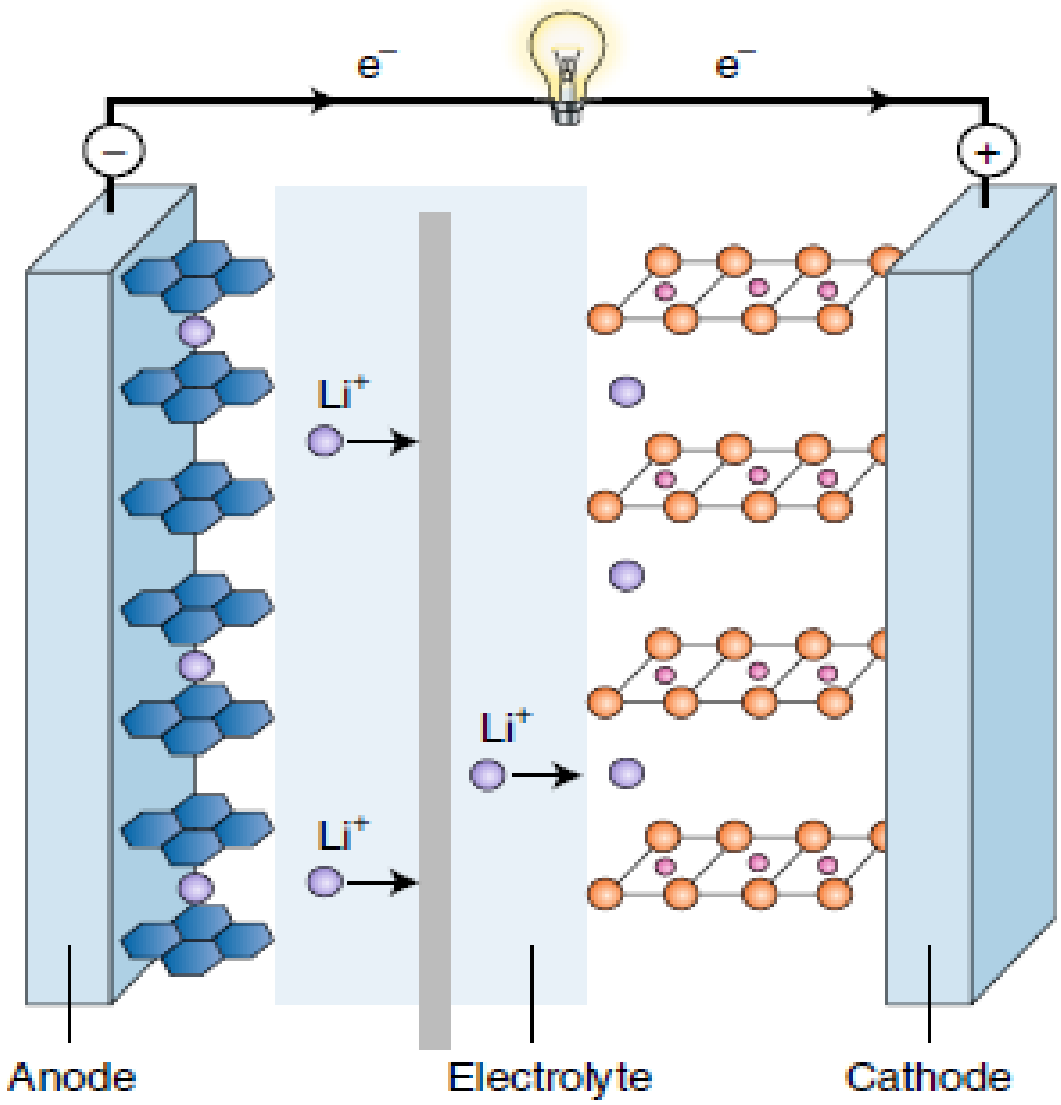

Lithium dendrites[13] are irregular lithium deposits. During charging, lithium ions deposit unevenly on the anode surface, forming irregular metal lithium dendrites. Under certain kinetic conditions, the tip of the dendrite grows faster than its radial expansion, resulting in a one-dimensional fibrous structure. Dendrites can appear as needle-like, mossy, or tree-like structures. Their growth can have various impacts on the battery, most notably piercing the separator and causing short circuits, or less noticeably, forming dead lithium deposits that reduce battery efficiency.

Electrolyte degradation refers to the decomposition of traditional electrolytes when the operating voltage exceeds 4.5V[14]. This occurs because commonly used organic carbonate solvents, such as linear carbonates—DMC (Dimethyl Carbonate), EMC (Ethyl Methyl Carbonate), DEC (Diethyl Carbonate)—and another cyclic carbonate, EC (Ethylene Carbonate), are not stable at high voltages. Their low oxidation potentials cause them to oxidize and decompose under high voltage, which reduces the performance of lithium-ion batteries and generates hydrofluoric acid, impacting the battery's lifespan.

The solid electrolyte interphase forms when lithium-ion batteries are charged and discharged for the first time[15]. During this process, a small amount of polar aprotic solvents in the electrolyte undergoes a reduction reaction after gaining some electrons, combining with lithium ions to form an interfacial film about 100-120 nm thick. This film is known as the SEI. The SEI typically forms at the solid-liquid interface between the electrode material and the electrolyte. Therefore, two types of solid electrolyte interphases are formed: one on the cathode surface during discharge (CEI)[16], and another on the anode surface during low-voltage charging (SEI)[16]. As the SEI thickness increases to the point where it becomes dense enough that neither electrons nor ions can easily penetrate, a passivation layer forms, inhibiting further redox reactions[15]. The composition of the SEI varies depending on the electrolyte composition but generally includes Li2O, LiF, LiCl, Li2CO3, LiCO2-R, alkoxides, and non-conductive polymers. The formation of the SEI during the initial charge-discharge cycle consumes some lithium ions, resulting in an increase in the battery's irreversible capacity and a decrease in the charging and discharging efficiency of the electrode material. This explains the detrimental effects of the SEI, as it consumes lithium ions that would otherwise contribute to the battery's capacity.

Figure 2 In lithium-ion batteries, the breathing behavior of the solid electrolyte interphase (SEI) occurs during the charge and discharge processes studied by using X-Ray Photoelectron Spectroscopy. The voltage is represented on the y-axis, while time is represented on the x-axis. The battery configuration is a half cell with Lithium metal vs. $LiCoO_2$. Reprinted with permission from Energy Storage Materials, 2018, Vol 14, 1-7. Copyright © 2018, Elsevier

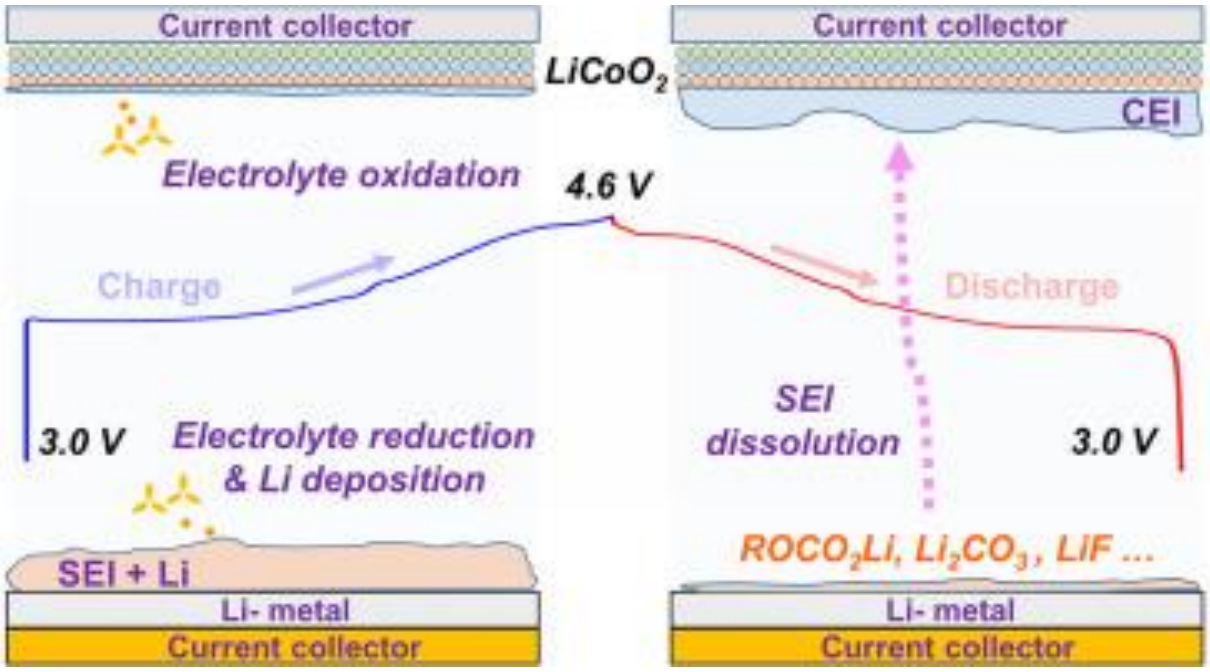

1.3 Manganese-dissolution & competing behavior

In recent years, lithium-ion batteries have been undergoing various breakthroughs and innovations in different directions, addressing issues such as limited range, long charging times, safety concerns, and high battery costs. As of 2022, the global sales penetration rate of electric vehicles has increased from 1% in 2018 to 14%[17,18]. The innovation in lithium-ion batteries is undoubtedly a powerful support for this trend of automotive electrification. However, to further promote electric vehicles on a large scale, the cost of battery assembly must fall below $100/KWh to approach the cost parity with internal combustion engines while still offering a certain level of fast-charging capability[1,2]. The best way to increase battery density[19] at similar costs[20] is to enhance the energy storage capacity of the battery. The most straightforward method is to change the chemical composition of the cathode material. Currently, there are two mainstream and mature types on the market: ternary lithium-based materials and lithium iron phosphate-based materials[21]. In this experiment, ternary lithium-based materials are the main focuses. This type of cathode material includes two types: NMC and NCA[22]. An interesting point is that by

sacrificing cobalt content to increase nickel content in the NMC battery material, the average energy density of the battery can be increased from 150Wh/kg (NMC111) to 210Wh/kg (NMC811). However, the cobalt content directly affects the thermal stability of the battery material, and from a raw material perspective, the cost of manganese is much lower than the cost of nickel. Therefore, in this context, NMC111 ($LiNi_xMn_yCo_zO_2$ with x=y=z=0.33) can be considered the most stable and market-demanding cathode material.

NMC exhibits excellent performance in terms of capacity, stability, and safety. Due to the extensive use of NMC cathodes in the last two decades[23,24], many previously unconsidered issues have emerged. However, with continuous cycling and aging of the battery, electrolyte degradation is inevitable. The hydrofluoric acid produced by electrolyte degradation[25] facilitates the dissolution of transition metals[26,27] in the anode. Consequently, manganese and nickel ions become contaminants in the electrolyte. Nickel ions tend to deposit on the electrode surface through parasitic reactions, while most manganese ions dissolve into the electrolyte. The amount of Manganese ion affects the capacity of NMC materials, and the lower cost and lower toxicity of manganese ions compared to the other two transition metals make it more favored. Therefore, the dissolution of manganese ions becomes an unavoidable contamination during battery cycling.

To visualize the impact of manganese ions on the electrolyte, Wang's work[28] mentions directly adding divalent manganese contaminants ($MnTFSI_2$) into a common $LiPF_6$ electrolyte. Over the same period, the container with manganese contaminants exhibited a significant color change. The same paper also used Density Functional Theory (DFT) calculations and Electrospray Ionization (ESI-MS) to calculate and simulate the Mn^{2+} solvation structure in a carbonate-based electrolyte under manganese-contaminated conditions. Thus, in terms of electrolyte, the presence of manganese ions results in a competitive effect between manganese and lithium ions. Since the working principle of lithium batteries relies on the conduction of lithium ions at different sites in the electrolyte. Therefore, the involvement of manganese ions leads to a competitive relationship with lithium ions, resulting in a decrease in the self-diffusion coefficient of lithium ions, thereby reducing the battery conductivity (increasing internal impedance) and decreasing battery capacity.

Figure 3 The typical first solvation sheath structures of Mn^{2+} that exist in liquid solutions can be detected by Electrospray Ionization Mass Spectrometry in gaseous state after partial desolvation of the cations. Reprinted with permission from Nature Communications, 2019, 3423, 10(1). Copyright © 2019, Nature Communications

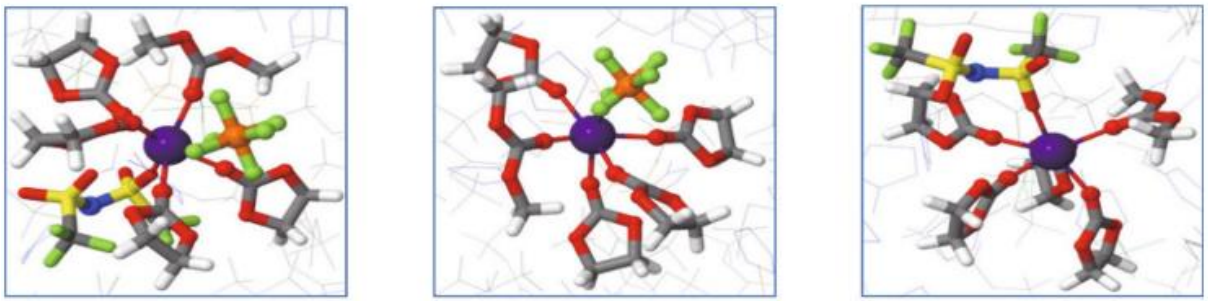

Transition metals like manganese (Mn), nickel (Ni), and cobalt (Co) play crucial roles in the performance and stability of lithium-ion batteries. These metals, often used in cathode materials such as NMC, can significantly influence both the electrochemical properties and the NMR parameters of the batteries. Transition metals can dissolve from the cathode during cycling, leading to capacity fade. To be more specific on the mechanism of transition metal dissolutions, Mn[29] can dissolve from $LiMn_2O_4$, especially at high voltages and in the presence of HF, which is formed from electrolyte decomposition. This dissolution results in the loss of active material from the cathode and deposition on the anode, causing impedance growth and capacity reduction. The presence of transition metals, particularly in their ionic forms like Mn^{2+}, Ni^{2+}, and Co^{2+}, may accelerate the decomposition of the electrolyte[30,31]. This process often involves the interaction of these metal ions with the electrolyte solvents, leading to the formation of unwanted side products that further degrade the electrolyte and electrode interfaces. Transition metals in different oxidation states participate in redox reactions during battery operation. For instance, Mn can exist in multiple oxidation states (Mn^{2+}, Mn^{3+}, Mn^{4+}), affecting the overall electrochemical performance and stability of the battery. These redox reactions are integral to the charge and discharge processes of the battery but can also lead to structural instability and capacity fading over time.

NMR spectroscopy and diffusometry are important tools that have been used in characterization of lithium ion battery performance by many groups[32–36]. In this thesis, we will utilize ^{7}Li spectroscopy, relaxometry and diffusometry to characterize the impact of paramagnetic ions on lithium ion diffusion in the electrolyte and to monitor the changes in mossy lithium and the solid-electrolyte interphase (SEI+CEI) during *operando* experiments, both using manganese-rich cathode materials. Study[37] show that the higher the concentration of dissolved transition metals, the greater the changes in relaxation times38 (see Chapter 2) in liquid samples. Initially, to simulate two stages during actual battery usage, two different concentrations of manganese ions were added to commonly used electrolytes: 1% manganese ion contaminants (first stage of manganese ion dissolution) and 5% manganese ion contaminants (later stage of manganese ion dissolution). These concentrations were chosen based on two papers by Clare Grey, which observed significant relaxation time changes starting with the low concentration group, and the high concentration group is assumed to reflect the level of contamination that an actual battery would experience after 500 cycles. The introduction of manganese ions is thought to decrease the self-diffusivity rate of lithium ions in the electrolyte, based on molecular dynamics simulations[28] and it is hypothesized that this reduction increases with higher manganese ion concentrations. Additionally, temperature variation experiments can measure the activation energy of lithium ion mobility in manganese-containing electrolytes. This can help determine if the introduction of manganese ions alters the dynamic mechanisms of lithium ions in the electrolyte.

Manganese ion contaminants dissolving into the electrolyte can trigger competitive effects. In the entire battery structure, other transition metals such as copper and iron (originating respectively from the current collector and the stainless-steel coin cell casing and spacer) may also impact the lithium self-diffusion coefficient. Currently, no other literature that mention the effects of these two transition metals dissolving into the electrolyte.

1.4 Application of different discharge methods

Fast charging has become a significant challenge in testing battery performance[39]. Due to the demand for faster energy replenishment in various applications (from consumer electronics to electric vehicles), achieving fast charging at different rates has become a critical research topic. However, the impact of discharging at different rates on battery performance is equally important but has not been sufficiently understood.

Pulse discharging[40] is an alternative method to regular discharging, and tests have shown that it can extend battery life and improve durability. This technique involves discharging the battery at short intervals instead of continuously, which may help reduce some of the stress on the battery components. However, it remains unclear which specific battery components are affected by discharging at different rates. Common fast charging (high charging rates) can quickly reach the required capacity, but it also exacerbates the accelerated growth of the SEI mentioned earlier and increases the number of non-reducible lithium ions (dead lithium) in the battery. Both factors, from an electrochemical performance perspective, can reduce the battery's lifespan and effective capacity. Therefore, changing the discharge rate during the discharge phase is also likely to affect these two aspects. Pulse discharging has rarely been tested in liquid-electrolyte cell structures to track changes in each component. It is hypothesized here that high current discharging may accelerate the formation and decomposition of the SEI, leading to uneven or more fragile SEI formation, and may trigger side reactions involving the decomposition of the electrolyte, causing changes in the composition accumulating on the SEI layer. For lithium metal, high current may lead to the formation of lithium dendrites, and the surface of the lithium metal will produce mossy lithium products of varying thickness. These behaviors may exhibit uniform breathing behavior with traditional charging and discharging methods: the SEI thickens with charging and is reduced with discharging, while mossy lithium increases with charging and is partially reduced with discharging[39]. Therefore, to track these potentially changing quantities, it is necessary to collect NMR data while gathering charging and discharging performance data.

1.5 Thesis outline

Based on the previous content, the impact of manganese ions on the electrochemical performance of batteries has been extensively studied. However, there have been no tests on the changes in self-diffusion coefficients due to competitive effects. PFG-NMR is well-suited for testing the diffusion coefficients of electrolytes containing manganese ions at different temperatures, and experimental data collected can be used to calculate the activation energy for lithium ion diffusion in the electrolyte. Additionally, the pencil cell design allows for testing the effects of manganese ions on batteries. On the other hand, the *operando* experimental setup can help observe morphological changes in the battery. This includes a set of experiments comparing pulse discharge with constant current discharge. The combination of half-cells used in *operando* experiments has been widely studied, but further experiments are needed to understand the influence of manganese ions with paramagnetic effects on *operando* experimental data.

Chapter 2 summarizes some basic NMR theories and provides a brief introduction to the subsequent NMR experiments.

Chapter 3 mainly explains the effects of manganese ions on the electrolyte and discusses the changes in electrolytes containing manganese ions before and after charging and discharging in actual batteries. It also presents electrochemical experimental results to demonstrate the impact of manganese ion intervention on battery capacity.

Chapter 4 briefly describes the changes in lithium metal and electrolyte under pulse discharge and constant current charging and discharging in *operando* experiments using cartridge cells. It also discusses the formation of mossy lithium, SEI, and CEI during the charging and discharging process.

Chapter 5 provides a summary of the entire thesis and outlines the future plan.

1.6 Reference

1. Jiang, B.-H., Hsu, C.-C., Su, N.-W. & Lin, C.-C. A Review of Modern Electric Vehicle Innovations for Energy Transition. *Energies (Basel)* **17**, 2906 (2024).

2. Yang, C. & Shi, H. J. Prospects of battery assembly for electric vehicles based on patent analysis. *International Journal of Low-Carbon Technologies* **18**, 1134–1139 (2023).

3. Lamb, W. F., Wiedmann T., Pongratz J., *et al.* A review of trends and drivers of greenhouse gas emissions by sector from 1990 to 2018. *Environmental Research Letters* vol. 16 Preprint at https://doi.org/10.1088/1748-9326/abee4e (2021).

4. Ahmed, M., Shuai, C. & Ahmed, M. Analysis of energy consumption and greenhouse gas emissions trend in China, India, the USA, and Russia. *International Journal of Environmental Science and Technology* **20**, 2683–2698 (2023).

5. Peled, E. & Menkin, S. Review—SEI: Past, Present and Future. *J Electrochem Soc* **164**, A1703–A1719 (2017).

6. Wang, A., Kadam, S., Li, H., Shi, S. & Qi, Y. Review on modeling of the anode solid electrolyte interphase (SEI) for lithium-ion batteries. *npj Computational Materials* vol. 4 Preprint at https://doi.org/10.1038/s41524-018-0064-0 (2018).

7. Goodenough, J. B. & Park, K. S. The Li-ion rechargeable battery: A perspective. *Journal of the American Chemical Society* vol. 135 1167–1176 Preprint at https://doi.org/10.1021/ja3091438 (2013).

8. Blomgren, G. E. The Development and Future of Lithium Ion Batteries. *J Electrochem Soc* **164**, A5019–A5025 (2017).

9. Manthiram, A. A reflection on lithium-ion battery cathode chemistry. *Nature Communications* vol. 11 Preprint at https://doi.org/10.1038/s41467-020-15355-0 (2020).

10. Manthiram, A. An Outlook on Lithium Ion Battery Technology. *ACS Cent Sci* **3**, 1063–1069 (2017).

11. Goodenough, J. B. How we made the Li-ion rechargeable battery: Progress in portable and ubiquitous electronics would not be possible without rechargeable batteries. John B. Goodenough recounts the history of the lithium-ion rechargeable battery. *Nature Electronics* vol. 1 204 Preprint at https://doi.org/10.1038/s41928-018-0048-6 (2018).

12. Ahmed, S., Nelson, P. A., Gallagher, K. G., Susarla, N. & Dees, D. W. Cost and energy demand of producing nickel manganese cobalt cathode material for lithium ion batteries. *J Power Sources* **342**, 733–740 (2017).

13. Takeda, Y., Yamamoto, O. & Imanishi, N. Lithium dendrite formation on a lithium metal anode from liquid, polymer and solid electrolytes. *Electrochemistry* **84**, 210–218 (2016).

14. Liao, Y., Zhang H., Peng Y., *et al.* Electrolyte Degradation During Aging Process of Lithium-Ion Batteries: Mechanisms, Characterization, and Quantitative Analysis. *Advanced Energy Materials* vol. 14 Preprint at https://doi.org/10.1002/aenm.202304295 (2024).

15. Solchenbach, S., Hong, G., Freiberg, A. T. S., Jung, R. & Gasteiger, H. A. Electrolyte and SEI Decomposition Reactions of Transition Metal Ions Investigated by On-Line Electrochemical Mass Spectrometry. *J Electrochem Soc* **165**, A3304–A3312 (2018).

16. Zhang, J. N., Li Q., Wang Y., *et al.* Dynamic evolution of cathode electrolyte interphase (CEI) on high voltage LiCoO2 cathode and its interaction with Li anode. *Energy Storage Mater* **14**, 1–7 (2018).

17. Zhou, Y., Wang M., Hao H., *et al.* Plug-in electric vehicle market penetration and incentives: a global review. *Mitig Adapt Strateg Glob Chang* **20**, 777–795 (2015).

18. Khaleel, M., Nassar Y., El-Khozondar H., *et al.* International Journal of Electrical Engineering and Sustainability (IJEES) https://ijees.org/index.php/ijees/index Electric Vehicles in China, Europe, and the United States: Current Trend and Market Comparison.

19. Shahjalal, M., Roy P., Shams T., *et al.* A review on second-life of Li-ion batteries: prospects, challenges, and issues. *Energy* **241**, (2022).

20. Curry, C. *Lithium-Ion Battery Costs and Market Squeezed Margins Seek Technology Improvements & New Business Models*. (2017).

21. Tran, M. K., Dacosta, A., Mevawalla, A., Panchal, S. & Fowler, M. Comparative study of equivalent circuit models performance in four common lithium-ion batteries: LFP, NMC, LMO, NCA. *Batteries* **7**, (2021).

22. Das, D., Manna, S. & Puravankara, S. Electrolytes, Additives and Binders for NMC Cathodes in Li-Ion Batteries—A Review. *Batteries* vol. 9 Preprint at https://doi.org/10.3390/batteries9040193 (2023).

23. Baccouche, I., Jemmali S., Manai B., *et al.* Li-ion battery modeling and characterization: An experimental overview on NMC battery. *International Journal of Energy Research* vol. 46 3843–3859 Preprint at https://doi.org/10.1002/er.7445 (2022).

24. Malik, M., Chan, K. H. & Azimi, G. Review on the synthesis of LiNixMnyCo1-x-yO2 (NMC) cathodes for lithium-ion batteries. *Materials Today Energy* vol. 28 Preprint at https://doi.org/10.1016/j.mtener.2022.101066 (2022).

25. Heider, U., Oesten, R. & Jungnitz, M. *Challenge in Manufacturing Electrolyte Solutions for Lithium and Lithium Ion Batteries Quality Control and Minimizing Contamination Level*. *Journal of Power Sources* vol. 81 www.elsevier.comrlocaterjpowsour.

26. Lüchtefeld, J., Hemmelamnn H., Wachs S., *et al.* Effect of Water Contamination on the Transition Metal Dissolution in Water-Enriched Electrolyte: A Mechanistic Insight into a New Type of Dissolution. *Journal of Physical Chemistry C* **126**, 17204–17211 (2022).

27. Banov, K., Breddemann, U., Khodeir, M. & Novák, P. Impact of Trace Nickel in the Electrolyte on the Electrochemistry of Positive Electrodes for Lithium-Ion Batteries. *J Electrochem Soc* **170**, 120515 (2023).

28. Wang, C., Xing L., Vatamanu J., *et al.* Overlooked electrolyte destabilization by manganese (II) in lithium-ion batteries. *Nat Commun* **10**, 3423 (2019).

29. Delacourt, C., Kwong A., Liu X., *et al.* Effect of Manganese Contamination on the Solid-Electrolyte-Interphase Properties in Li-Ion Batteries. *J Electrochem Soc* **160**, A1099–A1107 (2013).

30. Lüchtefeld, J., Lee M., Hemmelmann H., *et al.* Contribution of Electrolyte Decomposition Products and the Effect of Temperature on the Dissolution of Transition Metals from Cathode Materials. *ACS Omega* **8**, 32606–32614 (2023).

31. Solchenbach, S., Hong, G., Freiberg, A. T. S., Jung, R. & Gasteiger, H. A. Electrolyte and SEI Decomposition Reactions of Transition Metal Ions Investigated by On-Line Electrochemical Mass Spectrometry. *J Electrochem Soc* **165**, A3304–A3312 (2018).

32. Ohkubo, T., Gobet M., Sarou-Janian V., *et al.* Self-diffusion coefficient of lithium in molten xLi 2O-(1 - X)B 2O 3 system using high-temperature PFG NMR. *Chem Phys Lett* **530**, 61–63 (2012).

33. Bazak, J. D., Allen, J. P., Krachkovskiy, S. A. & Goward, G. R. Mapping of Lithium-Ion Battery Electrolyte Transport Properties and Limiting Currents with In Situ MRI. *J Electrochem Soc* **167**, 140518 (2020).

34. Krachkovskiy, S., Dontigny M., Rochon S., *et al.* Determination of Binary Diffusivities in Concentrated Lithium Battery Electrolytes via NMR and Conductivity Measurements. *Journal of Physical Chemistry C* **124**, 24624–24630 (2020).

35. Kaysan, G., Rudszuck T., Trapp L., *et al.* Recent applications of NMR diffusion experiments. in *Annual Reports on NMR Spectroscopy* vol. 107 47–93 (Academic Press Inc., 2022).

36. Kärger, J. & Ruthven, D. M. Diffusion in nanoporous materials: Fundamental principles, insights and challenges. *New Journal of Chemistry* vol. 40 4027–4048 Preprint at https://doi.org/10.1039/c5nj02836a (2016).

37. Allen, J. P. & Grey, C. P. Determining the oxidation states of dissolved transition metals in battery electrolytes from solution NMR spectra. *Chemical Communications* **59**, 1677–1680 (2023).

38. Allen, J. P. & Grey, C. P. Solution NMR of Battery Electrolytes: Assessing and Mitigating Spectral Broadening Caused by Transition Metal Dissolution. *Journal of Physical Chemistry C* **127**, 4425–4438 (2023).

39. Weiss, M., Ruess R., Kasnatscheew J., *et al.* Fast Charging of Lithium-Ion Batteries: A Review of Materials Aspects. *Advanced Energy Materials* vol. 11 Preprint at https://doi.org/10.1002/aenm.202101126 (2021).

40. Yang, N., Zhang, X. & Li, G. State of charge estimation for pulse discharge of a LiFePO4 battery by a revised Ah counting. *Electrochim Acta* **151**, 63–71 (2015).

Chapter2

Nuclear Magnetic Resonance theory

2.1 NMR fundamentals

The entire thesis experiment revolves around the analysis of collected nuclear magnetic resonance (NMR) data. This thesis mainly covers 1D ^{1}H, ^{7}Li NMR, PFG-NMR, and ^{7}Li *Operando* NMR, which is defined as the simultaneous collection of electrochemistry and NMR data. The characteristics and specific settings of these these experiments will be detailed in sections 2.2 and 2.3. The basic principle of PFG-NMR (Pulsed Field Gradient NMR) is to use magnetic field gradients to encode the signals of nuclei in liquid samples. After self-diffusion, the changes in the encoded signals are collected. *Operando*-NMR is simpler to understand; it involves collecting 1D spectra while simultaneously charging and discharging the battery sample. These two types of experiments have been widely applied in various lithium battery tests. The former is highly effective for measuring lithium self-diffusion rates, while the latter has been combined with many different charge-discharge algorithms to test the performance of lithium batteries.

Regarding nuclear magnetic resonance (NMR), the theory of NMR spectroscopy is based on the spin quantum number[41,42]. The spin quantum number (I) describes the intrinsic angular momentum of electrons, which is related to the atomic mass number (the number of protons and neutrons) and the atomic number (the number of protons). Elements with odd atomic numbers or odd mass numbers exhibit nuclear spin. For example, the H atom has an odd atomic mass and an odd atomic number. It has been calculated that its spin is equal to 1/2 and it will exhibit an NMR spectrum[43].

Every element has a charged nucleus, and when the spins of neutrons and protons in the nucleus are not paired, the net spin of the nucleus generates a magnetic dipole along the spin axis. The net magnitude of this dipole is called the nuclear magnetic moment. The internal structure of the molecule is determined by the symmetry and distribution of the magnetic dipoles. The principle behind NMR spectroscopy is based on the spin of atomic nuclei that can generate

a magnetic field. When there is no external magnetic field, the spins of the nuclei are randomly oriented; however, when an external magnetic field (B_0) is applied to the sample, the spins in the nucleus align either with or against the direction of the applied magnetic field. The external magnetic field induces an energy difference (ΔE) between the excited state and the ground state. Energy transfer occurs at a wavelength equivalent to the radio frequency. When the spin returns to its initial ground state, it emits the absorbed radio frequency, and this emitted radio frequency provides the NMR signal of the corresponding nucleus. The emitted radio frequency is proportional to the strength of the applied magnetic field. This energy splitting induced by the external magnetic field is called Zeeman splitting[44]. In nuclear magnetic resonance, to maximize this energy level splitting, the external magnetic field strength is increased as much as possible to collect higher quality NMR spectra. This emitted radio frequency provides the NMR signal of the corresponding nucleus. The emitted radio frequency is proportional to the strength of the applied magnetic field.

The angular momentum (or spin) and the magnetic moment $\vec{\mu}$are proportional, which is expressed by Eq. 2.2:

$$\vec{\mu} = \gamma \vec{I} \tag{2.1}$$

Where γ is the gyromagnetic ratio (the gyromagnetic ratio is the ratio of the nuclear magnetic moment to the angular momentum) and$\vec{I}$is the spin angular momentum.

Additionally, the previously mentioned energy difference is the product of the magnetic moment $\vec{\mu}$ and the applied external field B_0:

$$\Delta E = -\vec{\mu} \cdot B_0 \tag{2.2}$$

$$\mu = g_n \mu_n [I(I+1)]^{\frac{1}{2}} = \gamma h [I(I+1)]^{\frac{1}{2}} \quad (2.3)$$

$$\mu_z = g_n \mu_n m_I = \gamma h m_I \quad (2.4)$$

where magnetic moment can be separated out one component magnetic moment $\vec{\mu}$ in the direction of z. This magnetic moment can be defined as the Equation 2.4 by suing the nuclear spin parameter. By combining equations 2.2 and 2.4, we can derive equation 2.5, which verifies the Zeeman splitting[45,46] shown in the figure 4. Without the influence of an external magnetic field, the electrons are randomly distributed. However, when the magnetic field is applied, as shown in the figure 4 on the right, they split into two energy levels corresponding to parallel and antiparallel alignments.

$$E = -\gamma h m_I B_0 \quad (2.5)$$

Figure 4. Schematic diagram of Zeeman energy level splitting. The lower part shows the two states before and after the intervention of the external magnetic field. Before the intervention, the states are freely distributed, and after the intervention, they split into two energy levels in the positive and negative directions.

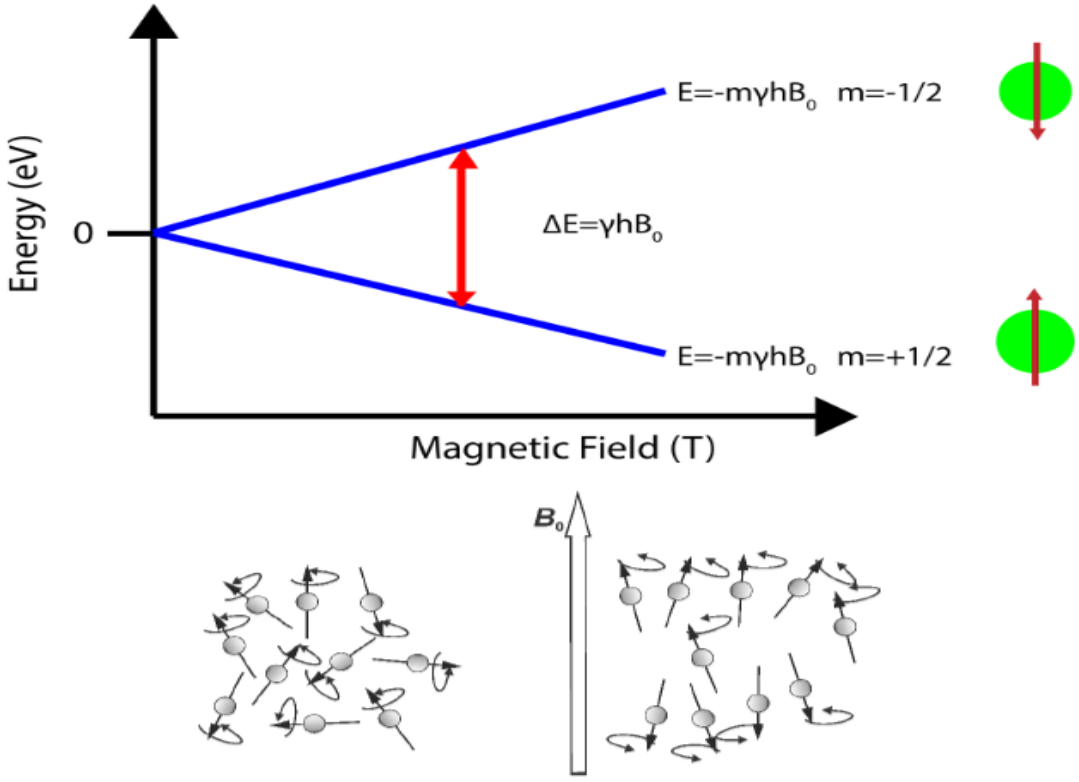

If the specific energy between the two levels can be determined, it is theoretically possible to apply appropriate electromagnetic radiation to activate the transition from the lower energy level to the higher energy level. At this point, the energy can be expressed as the product of Planck's constant and the radiation frequency, which can then be transformed into equation 2.6. And it can be converted into the Larmor frequency in radians per second (equation 2.7).

$$v = \frac{(\gamma B_0)}{2\pi} \tag{2.6}$$

$$\omega = -\gamma B_0 \tag{2.7}$$

In nuclear magnetic resonance, a classical model of the motion of a magnetic moment in a uniform magnetic field is often used (under the condition of constant total energy). A torque is applied to the magnetic moment, attempting to align it parallel to the magnetic field. However,

this torque can only change the angular momentum perpendicular to the magnetic field B_0, ultimately resulting in a circular motion around the axis of the magnetic field, forming a conical shape as shown in the figure 5. This motion is called precession, and this example of precession is widely known as Larmor precession. The angular velocity that induces this precession is the previously mentioned Larmor frequency.

Figure 5. Schematic diagram of Larmor precession. The magnetic moment moves in a circular motion along the direction of the magnetic field, following the dotted line.

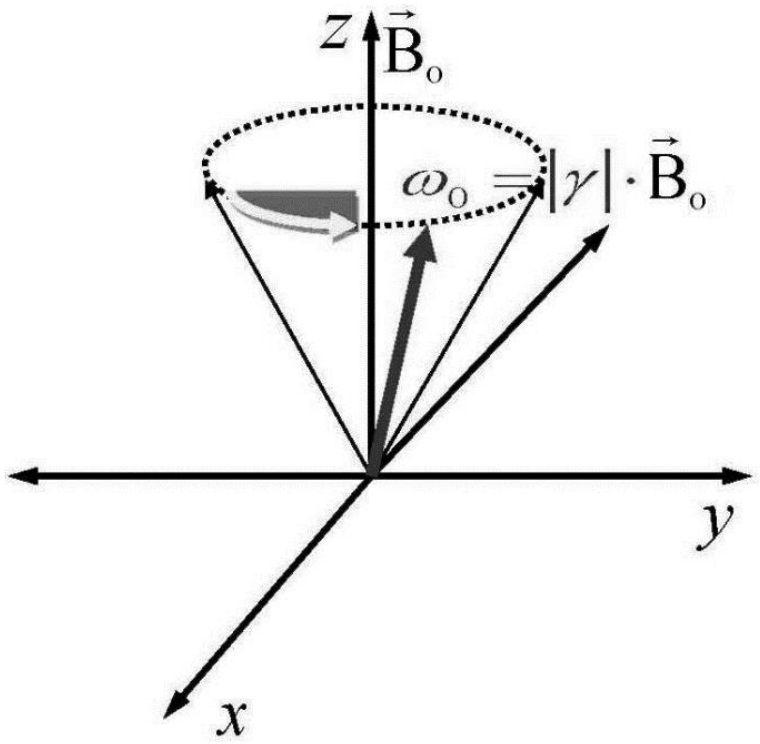

$$M = \sum \mu = \gamma B \tag{2.8}$$

When mentioning precession, it is necessary to refer to M , which is the total magnetic moment or magnetization. In the context of NMR experiments, the sample and magnetic

moment are influenced by the internal arrangement of individual nuclear spins. Therefore, a new quantity, M_0, is introduced, representing the equilibrium value of the sample when placed in a magnetic field. Bloch later discovered that the decay from M to M_0 is exponential. During this decay, the components of M parallel and perpendicular to M_0 decay at different rates, characterized by the relaxation times T_1 and T_2 , respectively. The methods for measuring these two relaxation times will be explained later in the text. Before introducing these measurement methods, it is necessary to discuss the effect of a pulse of radiation on an NMR spectrometer. In pulse experiments, an oscillating radiofrequency (r.f.) magnetic field pulse is applied for a certain period and then turned off. The frequency of this r.f. pulse is set close to the resonance frequency of the target nuclei to produce a magnetic field similar to that received in the direction perpendicular to the magnetization. Intuitively, in the rotating reference frame, the nuclear magnetization will precess in a fixed direction under the influence of the pulse. During the time period $\tau_p$that the pulse is applied, it will precess through an angle $\gamma B\tau$. As shown in the figure 6, a 90-degree pulse will rotate M by 90 degrees to lie on the y'-axis, while a 180-degree pulse will place it along the $-z$ -axis.

$$\frac{dM_z}{dt} = -\frac{(M_z - M_0)}{T_1} \tag{2.9}$$

$$\frac{dM_x}{dt} = -\frac{M_x}{T_2}, \ \frac{dM_y}{dt} = -\frac{M_y}{T_2} \tag{2.10}$$

Figure 6. The left side shows the conversion of the magnetic moment from the Z-axis to the y'-axis under the influence of a 90-degree pulse. The right side shows the conversion of the magnetic moment from the Z-axis to the -Z-axis under the influence of a 180-degree pulse. Reprinted with permission from IOP Science, 2010, 43, 213001. Copyright © 2010, Journal of Physics D: Applied Physics

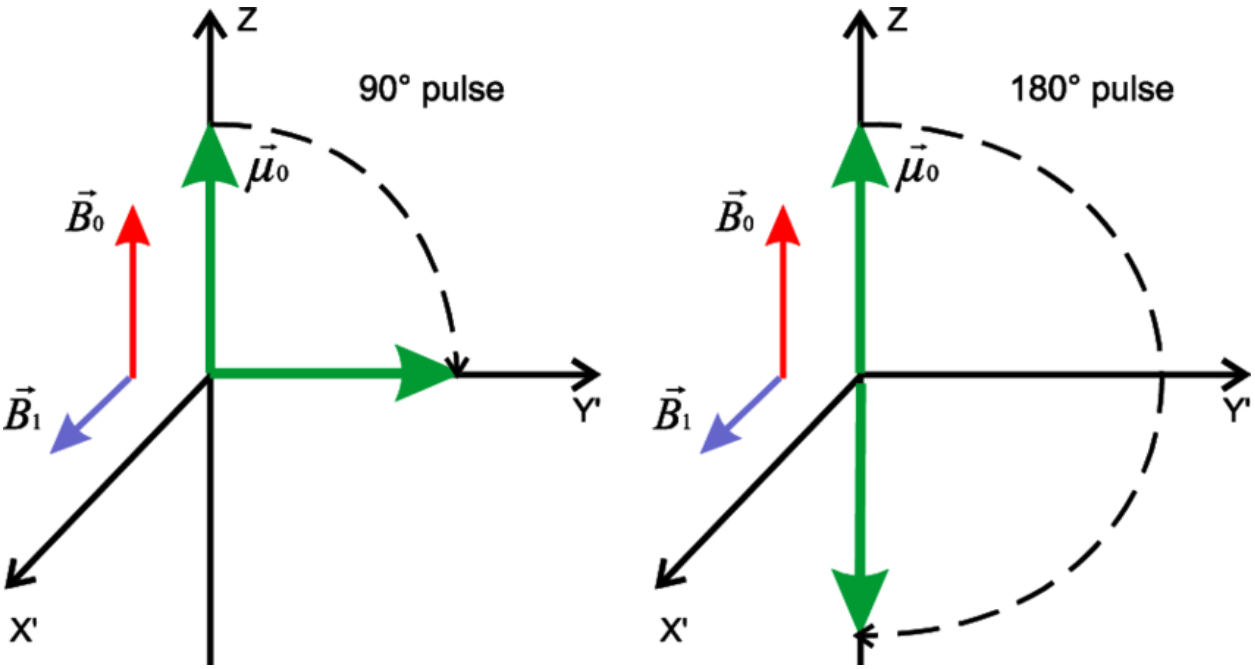

A pulse can be set in any direction without losing any magnetization magnitude. After the pulse, M will slowly return to the Boltzmann equilibrium state. According to equations 2.9 and 2.10, this can be expressed by the following formulas. T_1 and T_2 are the relaxation times mentioned earlier, representing the spin-lattice (180-degree pulse) and transverse (90-degree pulse) relaxation times, respectively. Because these relaxation processes are first-order kinetic motions, $T_1^{-1}$and T_2^{-1} are the relaxation rate constants.

$$M_z(t) - M_0 = [M_z(0) - M_0] \exp\left(\frac{-t}{T_1}\right) \tag{2.11}$$

$$M_y(t) = M_y(0) \exp\left(\frac{-t}{T_2}\right) \tag{2.12}$$

Figure 7. The first step is the simulated behavior of the magnetic moment in the magnetic field, followed by the free induction decay (FID) signal collected after relaxation. Finally, the FID is transformed into the experimental spectrum collected in nuclear magnetic resonance (NMR) through Fourier transformation.

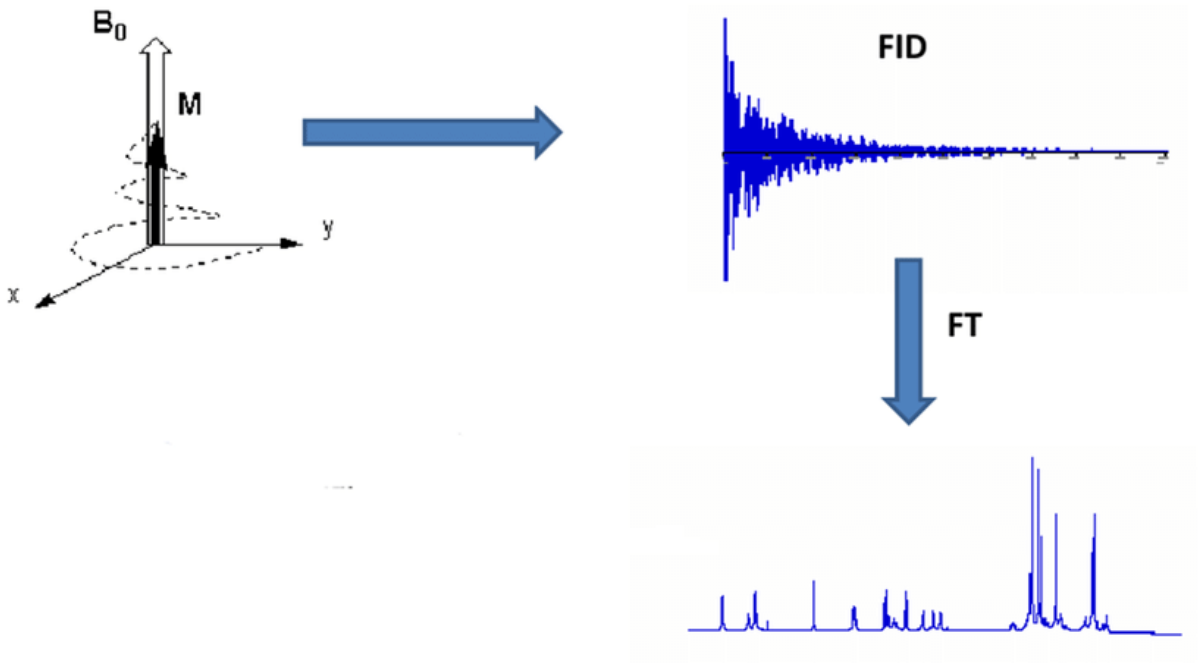

The decay that occurs during relaxation, observed as changes over the time axis, is recognized as free induction decay (FID). If all conditions are set properly, the information collected from the FID represents the signal throughout the entire relaxation process. However, to convert the FID into the commonly seen spectrum and to gather more useful information, a Fourier transform is required. In 1966[47], Ernst and Anderson achieved the Fourier transformation of the FID into a spectrum that represents the same information. Simply put, this transformation converts the time-domain FID into a frequency-domain spectrum.

Inversion Recovery is an experiment for measuring the T_1 relaxation time. A 180-degree pulse can activate spin-lattice relaxation, but since there is no magnetization along the y-axis, no signal can be collected. Therefore, an additional 90-degree pulse, often called the read pulse, is applied to monitor the decay caused by relaxation.

The experiment is called inversion-recovery[48,49] because it starts with a 180-degree pulse to invert the magnetization and then waits for it to recover on its own. The pulse sequence is represented as $[180^\circ - \tau - 90^\circ(FID) - T_d]_n$. Here, T_d is the delay time, which needs to be set

longer than the expected T_1 value to ensure that the Boltzmann population has started to reestablish before the next 180-degree pulse begins.

Figure 8. Schematic diagram of the Inversion Recovery experiment. The pulse sequence starts with a 180-degree pulse for inversion, followed by a waiting period for recovery along the -Z axis, and then a 90-degree reading pulse to collect the signal. The lower part shows the fitted curve from the IR experiment.

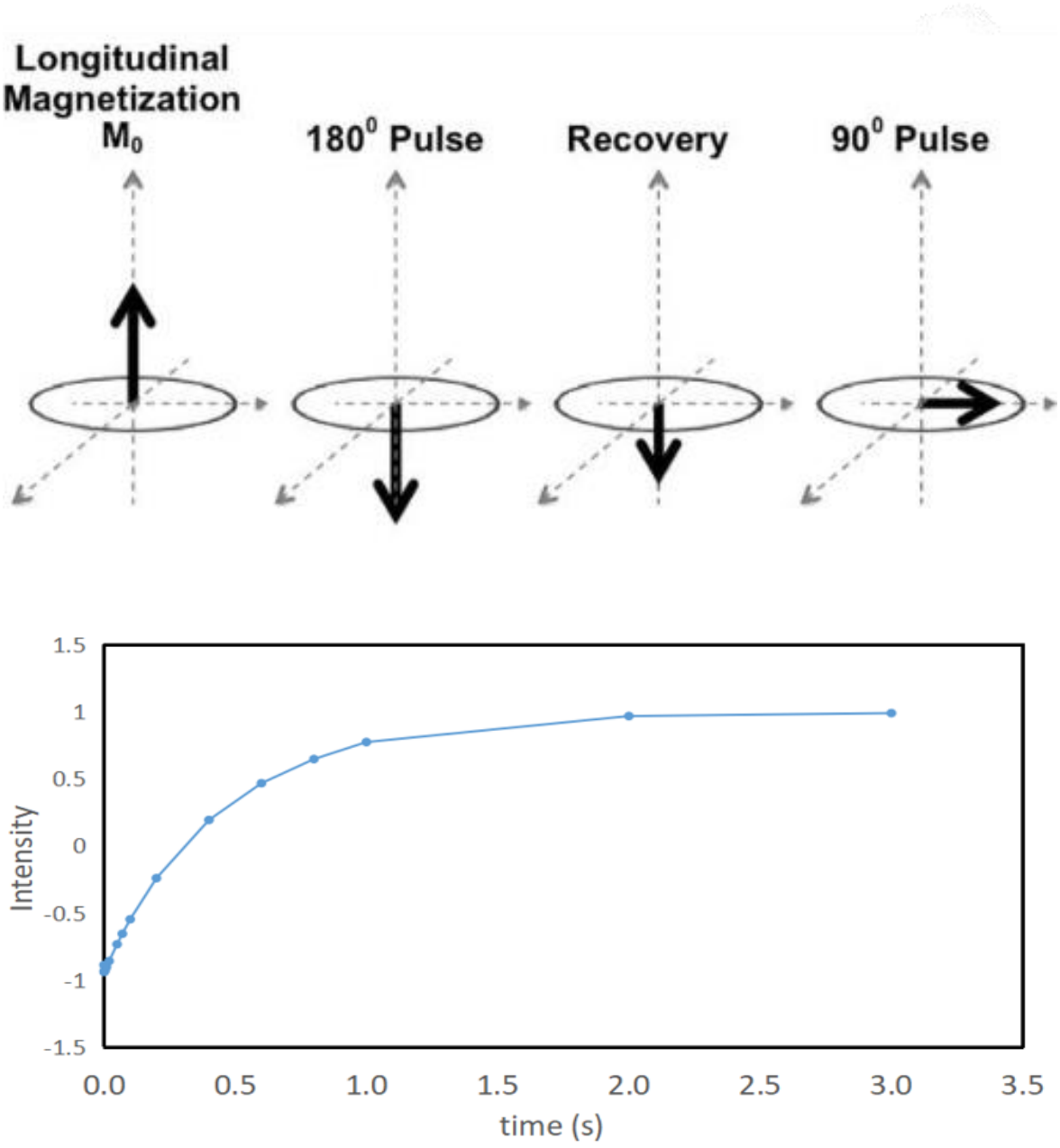

After the first 90-degree pulse is applied, transverse relaxation begins. However, due to field inhomogeneities, different magnetization vectors will spread out in various directions following Larmor precession. Hahn first attempted this experimental design and successfully introduced a series of pulses, leading to the observation of a spin-echo phenomenon. As shown in the figure 9, the 90-degree pulse rotates the magnetization to the y-axis, where the signal decays irregularly. Then, a 180-degree pulse is applied to invert the magnetization, causing the vectors to move in the same direction again. By continuously applying 180-degree pulses, this sequence is known as the Carr-Purcell-Meiboom-Gill (CPMG) experiment[50]. Ultimately, the collected spin-echo signals can be used to calculate the relaxation time.

$$90 - [\tau - 180^{\circ} - \tau - echo]_n$$

Figure 9. This is the pulse sequence of the CPMG experiment and the diffusion behavior of the signal in the horizontal direction. It starts with a 90-degree pulse that transfers the signal to the readable XY plane, followed by continuous 180-degree pulses to create spin-echo signals. The collected experimental data can be transformed into the exponential decay graph shown at bottom.

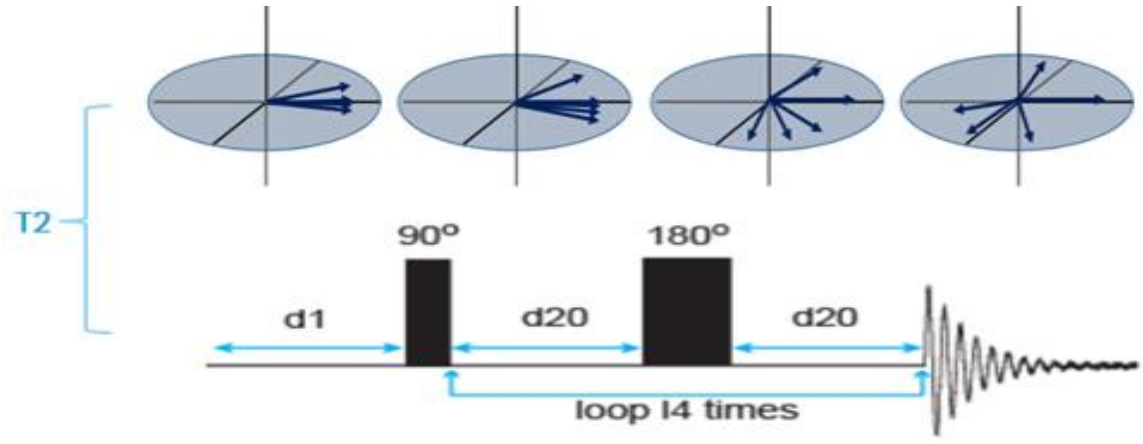

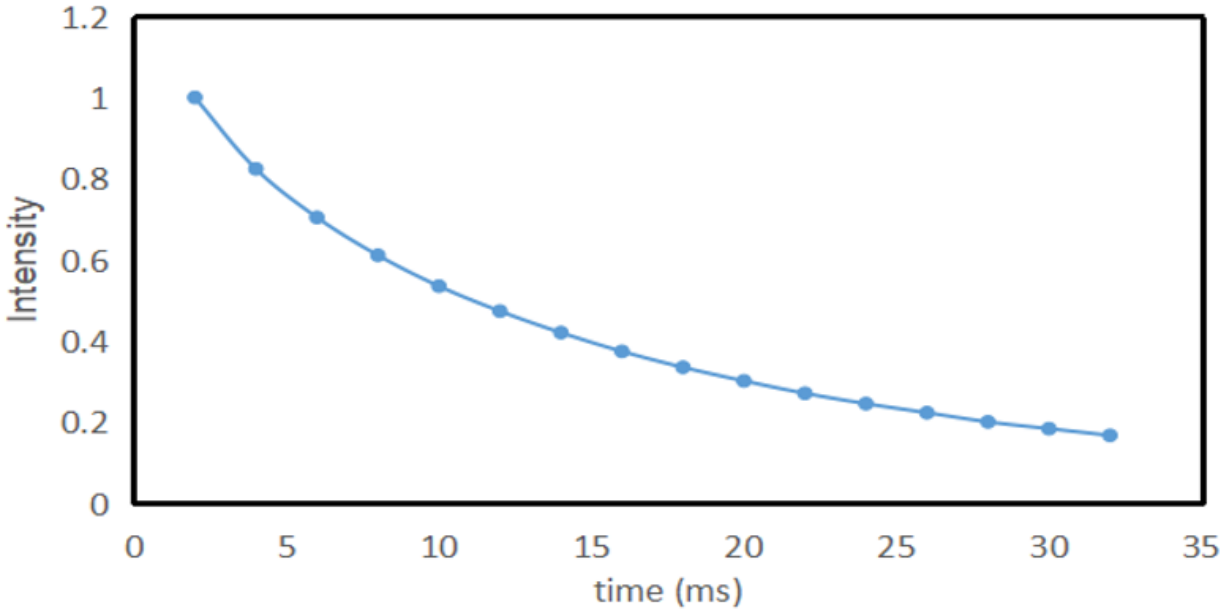

2.2 Pulsed-Field Gradient NMR

PFG-NMR (Pulsed Field Gradient Nuclear Magnetic Resonance) is a widely applied technique[35,51–53] that allows for the labeling of each signal in an experiment. ^{1}H and ^{7}Li PFG-NMR were both applied in this thesis. The former can effectively track the self-diffusion coefficients of carbonate-based solvents, while the latter can track the self-diffusion coefficients of lithium ions. The specific experimental details are as follows: By comparing the changes in signal intensity after a diffusion period, it calculates the nuclear self-diffusion rates. This technique was developed in the 1960s by Stejskal and Tanner[54], using the same theoretical principles as MRI to encode signals with gradients[36,55]. The experiment can be most intuitively understood by looking at the sequence. The PFG-SE sequence begins with a 90-degree read pulse, followed by the application of the first gradient to encode the signals. At exactly $\frac{\Delta}{2}$, a 180-degree pulse is applied to generate a spin-echo signal, reducing the inhomogeneity effects of the field on the signal. Finally, a second gradient pulse of the same strength is applied to decode the signals.

Figure 10. The upper part of the figure shows the simplest SE sequence in PFG-NMR, which is a gradient experiment based on spin-echo. The signal distribution in the lower part can be

analyzed accordingly. The first gradient encodes each signal, and after the diffusion time ends, another gradient is applied to decode each signal and compare the collected signal intensity.

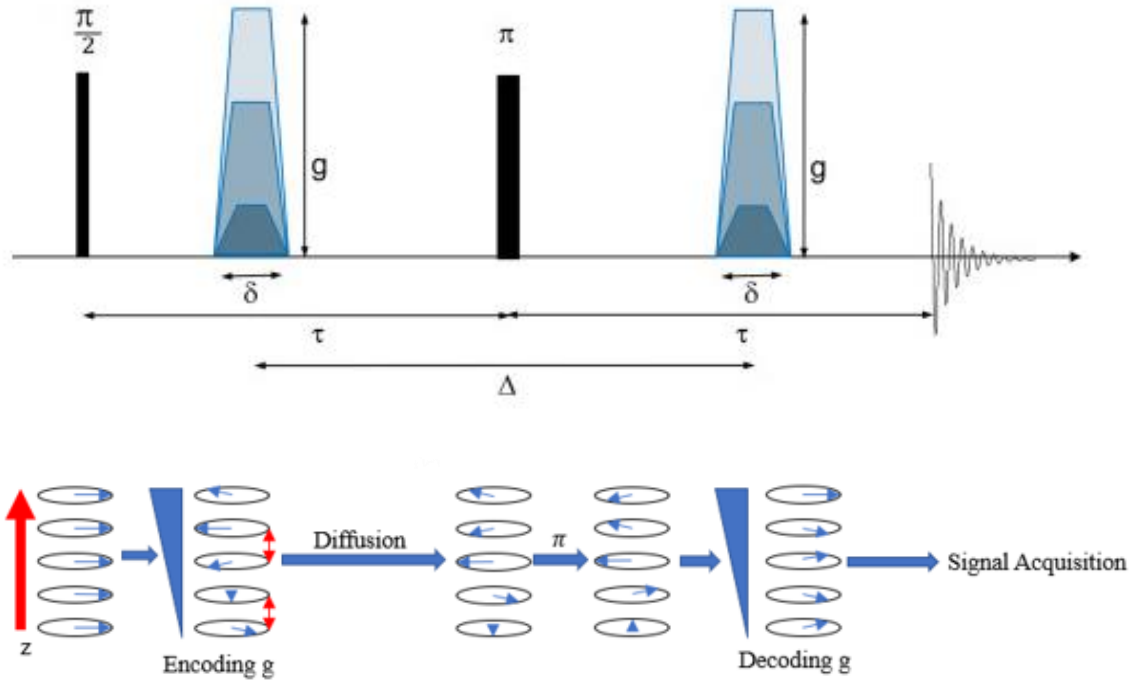

Figure 11. The upper part of the figure shows the FID curves of 1M LiCl collected under 16 different gradient strengths. Through Fourier transformation and fitting to the Stejskal-Tanner equation, the diffusion curve is obtained, as shown in the lower part.

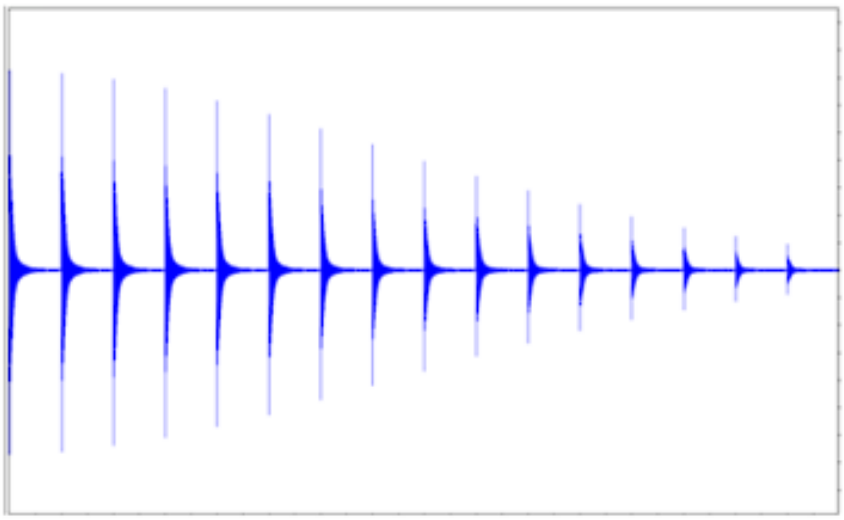

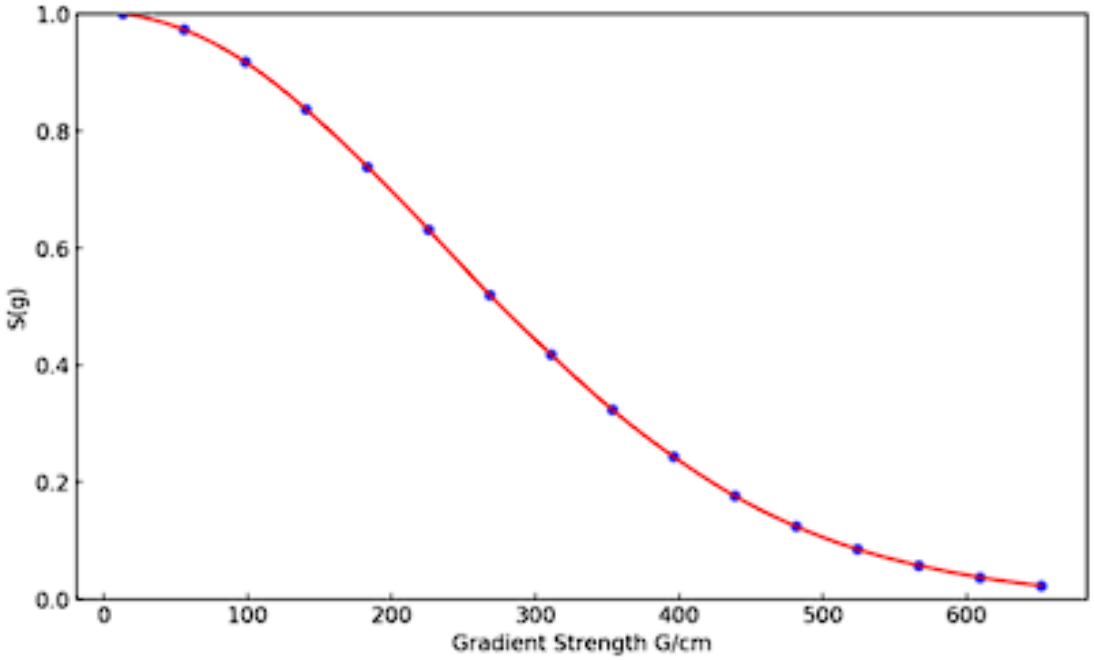

$$b = -\gamma^2 \delta^2 g^2 \left(\Delta - \frac{\delta}{3}\right) \tag{2.13}$$

$$\frac{S}{S_0} = \exp\left[-\gamma^2 \delta^2 g^2 \left(\Delta - \frac{\delta}{3}\right) D\right] \tag{2.14}$$

The figure 11 above shows the FID collected from the PFG-NMR experiment and its transformed schematic, based on the famous Stejskal-Tanner equation. As seen, this equation is derived from the signal decay due to diffusion, with the denominator representing the signal without the gradient applied, and D representing the diffusion coefficient. Since the power also exhibits exponential decay b , as shown in equation 2.13, and equation 2.14 displays the Stejskal-Tanner equation. When the constants in the equation remain unchanged, it can be observed that the signal intensity decays in a Gaussian manner with increasing gradient strength g .

Designing a series of variable temperature experiments to measure PFG-NMR not only allows for observing the effect of temperature on the self-diffusion coefficient but also enables the calculation of the activation energy for diffusion motion[56]. After collecting diffusion coefficients at different temperatures, the Arrhenius equation can be used to calculate the slope[57] between temperature and diffusion coefficient D .

E_a: Activation energy R : Universal gas constant, T : Temperature and x : corrected factor

$$\ln(D) = \frac{E_a}{R} \cdot \left(\frac{1}{T}\right) + x \tag{2.15}$$

Here, the definition of activation energy can be modeled using lithium batteries. If the lithium-ion diffusion coefficient affects the transportation mechanism of lithium ions in the battery, then changes in activation energy indicate changes in this transportation mechanism.

As the performance requirements in the battery industry become increasingly stringent, the kinetics of lithium ions have become more worthy of study, leading to the growing popularity of PFG-NMR experiments. Both ^{7}Li PFG-NMR and ^{1}H PFG-NMR were applied in this experiment. The former can test the diffusion behavior of lithium ions in the electrolyte samples of the battery, helping us understand the migration rate and mechanism of lithium ions. The latter can study the diffusion coefficient of solvent molecules to analyze the dynamics of the solvent and the properties of the electrolyte. The practicality of ^{7}Li PFG-NMR experiments is very high, as it can

observe both solid and liquid samples. For liquid electrolyte samples, to ensure uniformity, they are placed in NMR tubes of fixed size. However, for the electrolyte in actual batteries, a pencil cell design is used (detailed in section 3.2). This design ensures the uniformity of the electrolyte within the battery and maintains good signal strength and stability in the magnet. Furthermore, the size of the pencil cell is designed to fit the inner coil precisely, allowing direct testing of the electrolyte without disassembling the battery.

2.3 *Operando* NMR Experiment

Operando NMR experiments involve placing a battery in a magnet for measurement while simultaneously connecting it to instruments that collect its electrochemical performance[58]. This technique has become increasingly widely used because it allows for the accurate detection of the chemical environment and performance of the battery at each stage of charge and discharge. The previously mentioned pencil cell and cartridge cell can be applied to *operando* experiments because they exhibit stable performance within the magnet. A representative experiment is Trease's work in 2012[59], where a bag cell design was used for NMR experiments and tested the effect of different orientations of the battery within the magnet on chemical shifts. It was observed that when the battery is positioned parallel to the magnetic field, a peak for lithium metal appears at 270 ppm, and the electrolyte peak appears at -1.5 ppm. This setup is also used in the ^{7}Li *operando* experiments of this thesis. There are differences in the magnetic susceptibility of the materials inside the battery, which can lead to local magnetic field inhomogeneity within the battery. This effect is called the Bulk Magnetic Susceptibility effect. The orientation of the battery placement affects the distribution of the local magnetic field, resulting in different chemical shifts.

Figure 12. This figure shows the chemical shift variations of the bag cell in the magnet according to the direction of the applied magnetic field. Vertically, when parallel to the magnetic field, the green peak at 0 degrees shows 270 ppm representing lithium metal and -1.5 ppm representing the electrolyte. The black peak indicates the horizontal direction, perpendicular to the magnetic field, showing a 90-degree angle with 240 ppm representing lithium metal, and split peaks at

2.5 ppm and -10 ppm coming from the electrolyte. Reprinted with permission from Solid State Nuclear Magnetic Resonance, 2012, 42, 62-70. Copyright © 2019, Elsevier

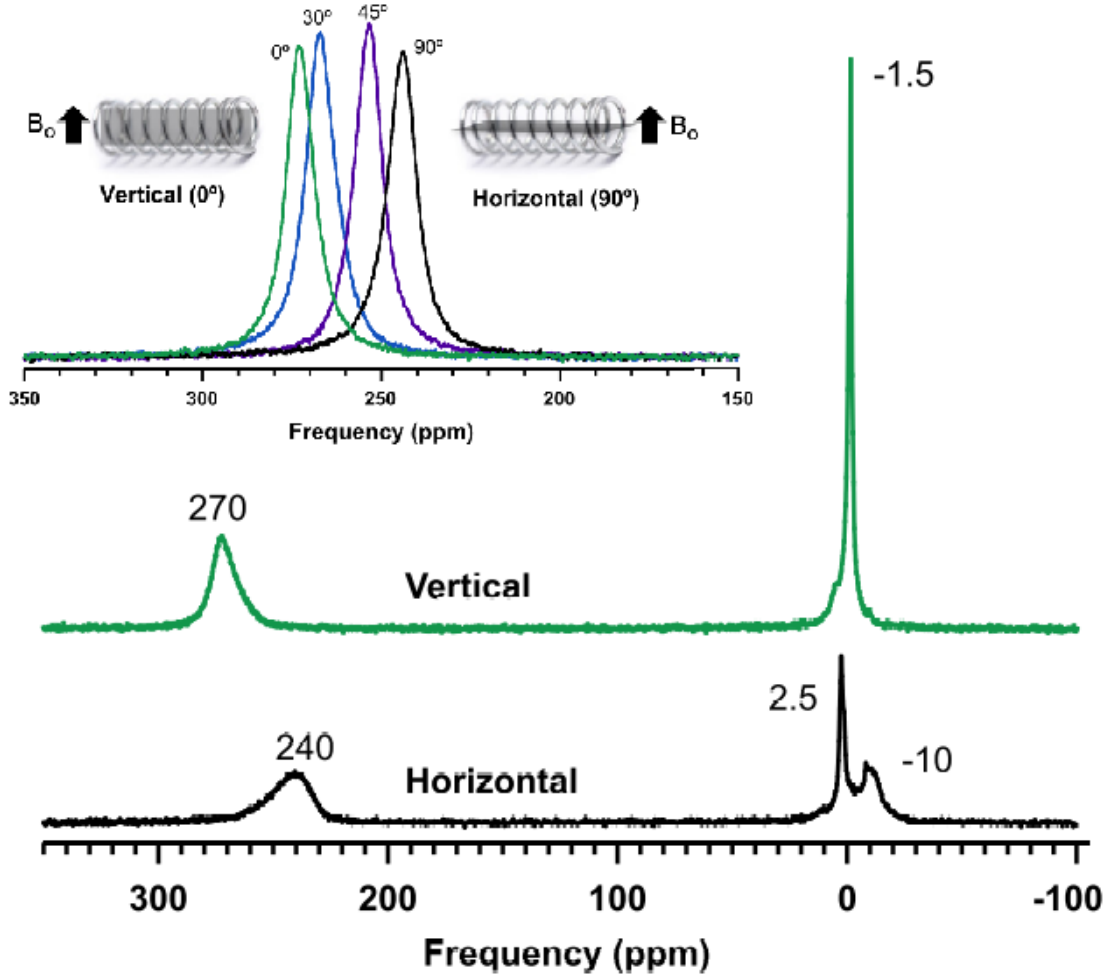

In this thesis, we utilized the cartridge cell design developed by our group (see Section 4.2 for details). This cell is placed between a set of parallel-plate resonators and then positioned vertically within the magnet. The cell casing is made of polyetheretherketone material, which ensures the cell's seal integrity while also providing good signal strength in NMR data. The *operando* experiments align well with the testing requirements mentioned earlier (Section 1.4), allowing for the simultaneous collection of cycling data and monitoring of SEI/CEI and mossy lithium. These quantities need to be distinguished by fitting the signals in the *operando* experiment slices, as both form a small shoulder peak next to the main peak (see Section 4.3.1

for details). Although the changes in SEI and mossy lithium are minimal between cycles, the cartridge cell design can still capture these changes clearly.

2.5 Reference

41. James, T. L. *Chapter 1 Fundamentals of NMR*.

42. Levitt, M. H. ..*Spin Dynamics, 2nd Edition*. (John Wiley & Sons, Ltd: Chichester, UK, 2008).

43. Karge, H. G. & Weitkamp, J. *Molecular Sieves Adsorption and Diffusion*.

44. Callaghan, P. T. *Principles of Nuclear Magnetic Resonance Microscopy*. (Oxford University Press: Oxford, UK, 1991).

45. Morgan, G. G. & Kühne, I. A. Molecular magnetochemistry. *Practical Approaches to Biological Inorganic Chemistry* 69–119 (2020) doi:10.1016/B978-0-444-64225-7.00003-1.

46. Ozerov, R. P. & Vorobyev, A. A. Elements of Quantum Mechanics. *Physics for Chemists* 423–496 (2007) doi:10.1016/B978-044452830-8/50009-X.

47. Bartholdi, E. & Ernst, R. R. Fourier spectroscopy and the causality principle. *Journal of Magnetic Resonance (1969)* **11**, 9–19 (1973).

48. Eaton, S. S. & Eaton, G. R. Multifrequency Pulsed EPR and the Characterization of Molecular Dynamics. in *Methods in Enzymology* vol. 563 37–58 (Academic Press Inc., 2015).

49. Karunakaran, C. & Balamurugan, M. Advances in Electron Paramagnetic Resonance. *Spin Resonance Spectroscopy: Principles and applications* 229–280 (2018) doi:10.1016/B978-0-12-813608-9.00005-8.

50. Moudrakovski, I. L. Recent advances in solid-state NMR of alkaline earth elements. in *Annual Reports on NMR Spectroscopy* vol. 79 129–240 (Academic Press Inc., 2013).

51. Hayamizu, K. 7Li spin-echo NMR diffusion studies. in *Annual Reports on NMR Spectroscopy* vol. 98 57–123 (Academic Press Inc., 2019).

52. Johnson, S. G. *A PFG NMR Experiment for Accurate Diffusion and Flow Studies in the Presence of Eddy Currents*. *JOURNAL OF MAGNETIC RESONANCE* vol. 93.

53. Han, K. S., Bazak J., Chen Y., *et al.* Pulsed Field Gradient Nuclear Magnetic Resonance and Diffusion Analysis in Battery Research. *Chemistry of Materials* vol. 33 8562–8590 Preprint at https://doi.org/10.1021/acs.chemmater.1c02891 (2021).

54. Stejskal, E. O. & Tanner, J. E. Spin diffusion measurements: Spin echoes in the presence of a time-dependent field gradient. *J Chem Phys* **42**, 288–292 (1965).

55. Stallmach, F. & Galvosas, P. Spin Echo NMR Diffusion Studies. *Annual Reports on NMR Spectroscopy* vol. 61 51–131 Preprint at https://doi.org/10.1016/S0066-4103(07)61102-8 (2007).

56. Haaks, M., Martin, S. W. & Vogel, M. Relation of short-range and long-range lithium ion dynamics in glass-ceramics: Insights from Li 7 NMR field-cycling and field-gradient studies. *Phys Rev B* **96**, (2017).

57. Van Der Ven, A., Bhattacharya, J. & Belak, A. A. Understanding Li diffusion in Li-intercalation compounds. *Acc Chem Res* **46**, 1216–1225 (2013).

Chapter 3

NMR Study on the Impact of Transition Metal Dissolution on Electrolytes

3.1 Introduction

An unavoidable reality in lithium batteries is the degradation of the electrolyte, which produces hydrofluoric acid in the process. This acid is not only a harmful substance but also damages the electrolyte itself. Because NMC111 is composed of three different transition metals, it provides a good opportunity for hydrofluoric acid[14,60] to act as a carrier for dissolving transition metals. The dissolution of manganese and nickel is relatively prominent and has already attracted some attention. Due to nickel's dissolution being more related to some parasitic reactions and its tendency to deposit on the solid electrolyte interphase layer[61,62] in aging cells, the impact of manganese ions on the electrolyte is more noteworthy.

In cathode materials, manganese ions primarily exist in the trivalent form because of their higher stability in the structure and their ability to form stable layered crystal structures. However, under high voltage conditions, the resulting high temperatures can induce the Jahn-Teller effect, causing the asymmetric distribution of electrons in the complex to change, thereby lowering the overall system's energy to reach a more stable state. This is manifested as the trivalent manganese ions spontaneously reducing from a high-spin d4 electronic configuration to a divalent manganese ion d5 configuration to avoid the Jahn-Teller effect caused by high temperatures. Additionally, trivalent manganese ions are very unstable in solution, and the interaction between solvent molecules in the electrolyte and divalent manganese ions is stronger, which further proves that divalent manganese ions are the most stable state in the electrolyte[63,64]. Secondly, there are chemical reactions between the electrolyte and the electrode material. Once Mn^{2+} dissolves into the electrolyte, it reacts with components in the electrolyte, such as carbonate-based organic solvent. Mn^{2+} can combine with anions in the electrolyte (e.g., PF_6^- or

$TFSI^-$) to form stable solvation strucutre[28,65]. These complexes diffuse in the electrolyte, further affecting the chemical properties and stability of the electrolyte. Additionally, surface deposition and interfacial reactions occur as the dissolved Mn^{2+} ions deposit at the electrode surface and the electrolyte interface, forming an interfacial layer containing manganese compounds. This interfacial layer may consist of manganese oxides (such as MnO or Mn_2O_3) or fluorides (such as MnF_2). These deposits increase the interfacial resistance[15,28,64] between the electrode and the electrolyte, reducing the electrochemical performance of the battery. During the cycling of the battery, the dissolved Mn^{2+} can continuously dissolve and redeposit on the electrode surface. This dissolution-redeposition cycle leads to the gradual depletion of the electrode material, reducing the battery's capacity and cycle life.

In summary, the dissolution of manganese ions negatively impacts battery performance[64] and can be summarized into four concerns:

1. **Reduced Electrolyte Stability**: The dissolution of manganese ions reacts with components in the electrolyte, leading to decreased chemical stability of the electrolyte. For example, Mn^{2+} can react with solvent molecules (such as ethylene carbonate, EC) and salts (such as $LiPF_6$) in the electrolyte, altering their structure and reaction energy, thereby accelerating the decomposition of the electrolyte.
2. **Increased Interfacial Impedance Due to Electrode Surface Deposition**: Dissolved manganese ions deposit on the electrode surface, forming oxides or fluorides of manganese. These deposits increase the interfacial impedance between the electrode and the electrolyte, reducing the battery's conductivity and charge-discharge efficiency.
3. **Decreased Lithium-Ion Mobility**: The presence of dissolved manganese ions in the electrolyte affects the mobility of lithium ions. Studies have shown that manganese ions can reduce the diffusion coefficient and transference number of lithium ions in the electrolyte, thereby affecting the overall performance and lifespan of the battery[66].
4. **Capacity Fade**: The dissolution of manganese ions leads to the loss of active material, causing battery capacity fading. This effect is particularly pronounced when the battery

operates at high voltages, as manganese ions in the electrode material are more prone to dissolution, significantly affecting the cycle life of the battery.

From the perspective of nuclear magnetic resonance (NMR), the paramagnetic properties of manganese ions alter the chemical environment of the electrolyte. The presence of manganese ions causes chemical shift changes in the NMR spectra. Due to their paramagnetic nature, manganese ions (especially Mn^{2+}) generate strong local magnetic fields, which affect the chemical shifts of nearby atoms. This effect is known as the paramagnetic chemical shift[67]. The chemical shifts caused by the paramagnetic nature of manganese ions are generally much larger than those of diamagnetic atoms of similar size.

The paramagnetic nature of manganese ions also leads to broadening of NMR signals. The unpaired electrons interact with the nuclear spins, causing the NMR signal to broaden—a phenomenon known as paramagnetic broadening. The local magnetic fields generated by unpaired electrons make the NMR signals uneven, resulting in broadened signals in the spectra. Moreover, the presence of manganese ions significantly affects the relaxation times of other nuclei in the electrolyte. Paramagnetic ions accelerate the relaxation process of nuclear spins, leading to shortened T1 time[68,69] (around This occurs because unpaired electrons can effectively transfer energy to the nuclear spins through dipole-dipole interactions[70].

The following experimental data validates the paramagnetic effects caused by manganese ions. Electrolytes containing manganese were observed to have broader peaks, and the lithium self-diffusion coefficient in the manganese-containing electrolyte was slower compared to the pure lithium electrolyte. However, the activation energy for lithium diffusion remained unchanged.

3.2 Experimental

A battery-grade electrolyte, consisting of 1M $LiPF_6$ in a 1:1 weight ratio of EC/DMC, was obtained from Sigma-Aldrich. This electrolyte is stored within an argon-filled glovebox and utilized as the base (reference) electrolyte. Contaminants of various concentrations are

introduced into this base electrolyte: a high-concentration mixture including 0.05 M $Mn(CF_3O_3S)_2$, 0.05 M anhydrous $CuCl_2$, 0.05 M anhydrous $FeCl_2$, 0.1 M Li(TFSI), and 0.1 M anhydrous LiCl; and a low-concentration mixture featuring 0.01 M $Mn(CF_3O_3S)_2$, 0.01 M anhydrous $CuCl_2$, 0.01 M anhydrous $FeCl_2$, 0.02 M Li(TFSI), and 0.02 M anhydrous LiCl. A 1 M LiCl solution is formulated to act as a reference standard for calibrating the ^7Li NMR, and Sodium trimethylsilylpropanesulfonate (DSS) in Deuterium oxide is used for calibrating the chemical shift position in proton NMR.

Sample	Additive
1M $LiPF_6$ in EC/DMC (1:1 wt%)	Reference electrolyte
1M $LiPF_6$ in EC/DMC (1:1 wt%)	+ $Mn(CF_3O_3S)_2$
1M $LiPF_6$ in EC/DMC (1:1 wt%)	+ Li(TFSI)
1M $LiPF_6$ in EC/DMC (1:1 wt%)	+ anhydrous $CuCl_2$
1M $LiPF_6$ in EC/DMC (1:1 wt%)	+ anhydrous $FeCl_2$
1M $LiPF_6$ in EC/DMC (1:1 wt%)	anhydrous LiCl

Table 2. Electrolyte samples tested in the experiment. The green reference electrolyte is a commonly used electrolyte, and different colors represent different transition metal environments. Additionally, similar anion electrolytes are used as reference points for activation energy calculations, marked in blue.

The pencil cell is another design improved many times, and this cell geometry has been applied for some *operando* experiment [71]. The entire battery is made of PEEK material, with two identical nodes at both ends. Any material current collector (such as copper, aluminum, and titanium) can be placed inside the nodes. Inside the battery, there is a pre-drilled cylindrical area. This area can be used to place an electrolyte, either solid or liquid. Due to the concentrated internal space and good contact with the electrodes after assembly, the battery size fits perfectly inside an NMR coil. This allows NMR experiments to better observe the chemical environment changes of the electrolyte inside the battery. During different charging and discharging stages, the Li concentration in the internal electrolyte varies to some extent. Based on the uniformity of the internal cylindrical area, NMR spectroscopy can divide the electrolyte into several equal regions under different gradient strengths, allowing observation of the chemical environment of Li ions in each region.

Figure 13. Design and parameters of the pencil cell, with detailed assembly order as follows: the threaded position on the left corresponds to the first node in the lower diagram (aluminum current collector). In the upper diagram, the green and gray sections on the right sequentially represent the NMC811 electrode. The 2mm wide middle section contains the electrolyte (with two internal glass-fiber separators). The far right shows the graphite anode and copper current collector node.

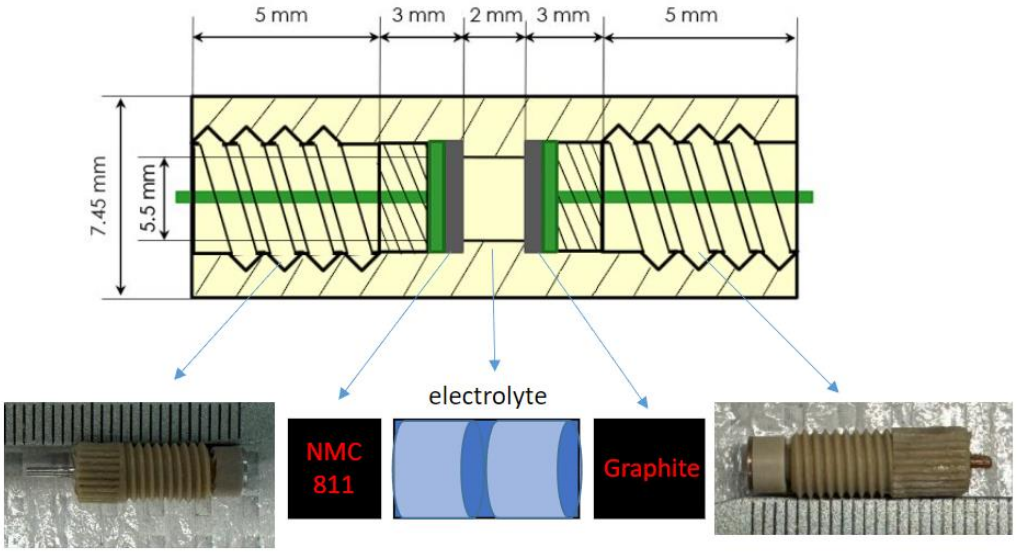

The assembly of the pencil cell[33,71] is shown in the figure 13 above, with $LiNi_{0.8}Mn_{0.1}Co_{0.1}O_2$ (NMC811, 21.9 mg/cm², 4.0 mA h/cm²) as the cathode and graphite (13.61 mg/cm², 4.5 mA h/cm²) as the anode. The electrolyte, as shown in the table above, consists of an electrolyte containing 0.01 M manganese ions and a reference electrolyte, which were respectively used in two pencil cells for a comparative experiment. The initial tests of the assembled cells were not ideal. Without any separator added to the electrolyte, the battery could not be successfully charged, and there was leakage of the electrolyte. After improvements and continuous testing, it was determined that the nodes at both ends of the battery needed to be pre-sealed with epoxy to prevent leakage. Additionally, during the assembly process, two pieces of glass fiber were added to the electrolyte to serve as separators, aiming to improve the contact between the electrodes and the electrolyte.

After the assembly was completed in the glove box, the pencil cell was left stationary on the bench for 4 hours to check the battery's stability and sealing. The open-circuit voltage (OCV) was measured around 300 mV using a voltmeter. At this point, the entire battery was placed into the probe coil to measure the lithium self-diffusion coefficient of the electrolyte using NMR at room temperature before starting the charging process. To ensure the battery could survive through two charge-discharge cycles, a relatively safe rate (C/20), which is 0.03 mA, was used for charging and discharging the battery. There was a 12-hour resting period before starting the charging. The charging conditions were set as commonly used for batteries: 2.7 V as the lower cutoff voltage and 4.2 V as the upper cutoff voltage. After successfully completing two charge-discharge cycles, the battery was collected, and the lithium self-diffusion coefficient of the electrolyte was measured again using NMR.

The coin cell uses the same materials as the pencil cell, but with different electrolyte choices: 0.01 M manganese ion, 0.05 M manganese ion contaminated electrolyte, and reference electrolyte. The assembly of each battery is identical, utilizing a double-layer Celgard 2325 separator and 140 μL of electrolyte. Unlike the pencil cell charging setup, the coin cell undergoes 50 charging cycles. At the end, the discharge capacity of the battery will be compared under different concentrations of manganese ion contamination.

NMR experiments were conducted using a Bruker Ascend 300WB with Avance III HD instrument at 7.05 T with a nominal ^{7}Li frequency of 116.7 MHz. For samples packed in NMR tubes, chemical shift calibration was performed using a 1M LiCl sample, and temperature calibration was done using methanol and ethylene glycol for the 273-308K temperature range. The samples with different concentrations packed in NMR tubes were tested directly, with the testing comprising Inversion Recovery experiments to measure T1 relaxation times and PFG-NMR to measure lithium self-diffusion rates (gradient strength ranging from 13 to 650 G/cm). For the two sets of pencil cell tests, the diffusion coefficient was measured using PFG-NMR experiments at room temperature only.

Date	Tube	T		
Mar 06 2023	5mm	278 K-298 K		
Chiller Power	Target Gas Flow	Standby Gas Flow		
Strong	600 lph	100 lph		
		Methanol		
Exp No.	Targeted T	Delta Chemical shift	Calculated T	Water
1	278	1.73	280.71	10
2	283	1.69	285.15	10
3	288	1.64	290.59	15
4	293	1.60	294.85	20
5	298	1.55	300.08	25
		Ethylene Glycol		
Exp No.	Targeted T	Delta Chemical shift	Calculated T	Water
1	298	1.65	299.69	25
2	303	1.6	304.71	30
3	308	1.55	309.72	35

Table 3. Temperature calibration based on methanol and ethylene glycol chemical shift value between 278K- 308K

Figure 14. Temperature Calibration- plots for Ethylene glycol & Methanol (in nuclear magnetic resonance after connecting the BCU unit and water tank. The calibration NMR experiment temperature settings are as follows: cooling unit output power set to strong, gas flow set to 600 lph, and standby gas flow set to 100 lph. The temperature calibration range is from 273K to 303K,

using two chemical solvents, methanol and ethylene glycol, to calibrate the temperature based on their chemical shifts at different temperatures.)

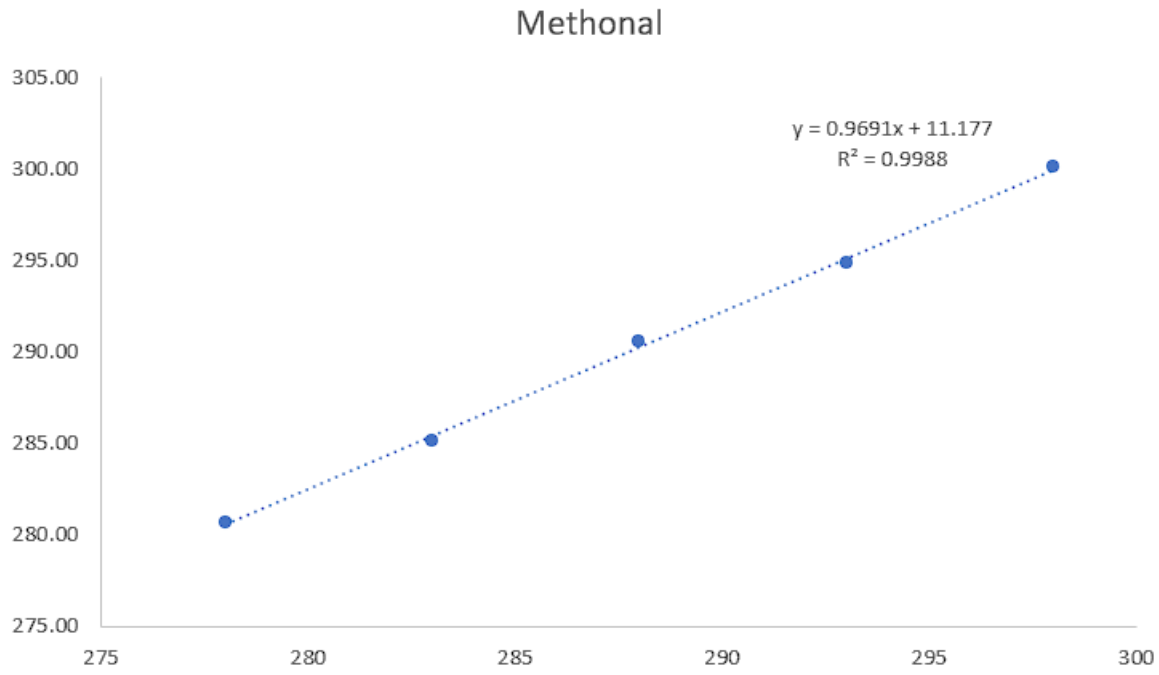

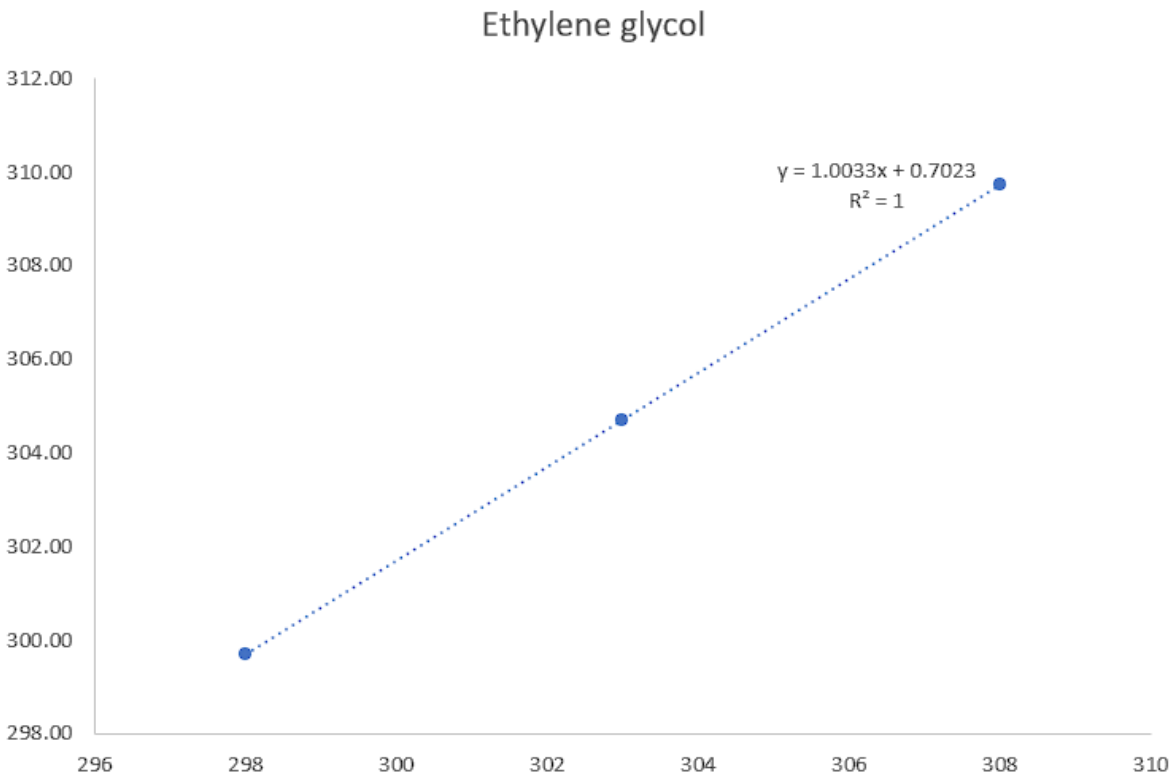

3.3 Results

3.3.1 Electrochemical results

The electrochemical tests were conducted using an Arbin instrument. In the coin cell tests, the electrolyte containing 0.01 M manganese ions did not show significant differences in discharge capacity compared to the reference electrolyte over 50 cycles. However, the introduction of 0.05 M manganese ions led to non-chargeable electrochemical performance along the 50 cycles time scale, shown in Figure 15 . Although the capacity stabilized afterward, it was clear that the discharge capacity was nearly depleted. This confirmed our initial hypothesis that the presence of manganese ions affects the battery's capacity. Interestingly, a small amount of manganese ions did not cause a significant change.

Similarly, the pencil cells successfully cycled with the 0.01 M manganese-contaminated electrolyte and the reference electrolyte. Both had comparable discharge capacities in the first cycle, but it was evident that the two batteries experienced different stages during the cycling process. The presence of manganese ions introduced more complex stages in the cycling process, possibly due to the formation of a different solid electrolyte interface (SEI) or manganese ion deposition, compared to the reference electrolyte. This is currently a hypothesis and requires further experiments to validate this behavior.

Figure 15. Coin Cell Testing results on discharge capacity changes of lithium batteries in different electrolyte environments, with charge cycles on the x-axis.

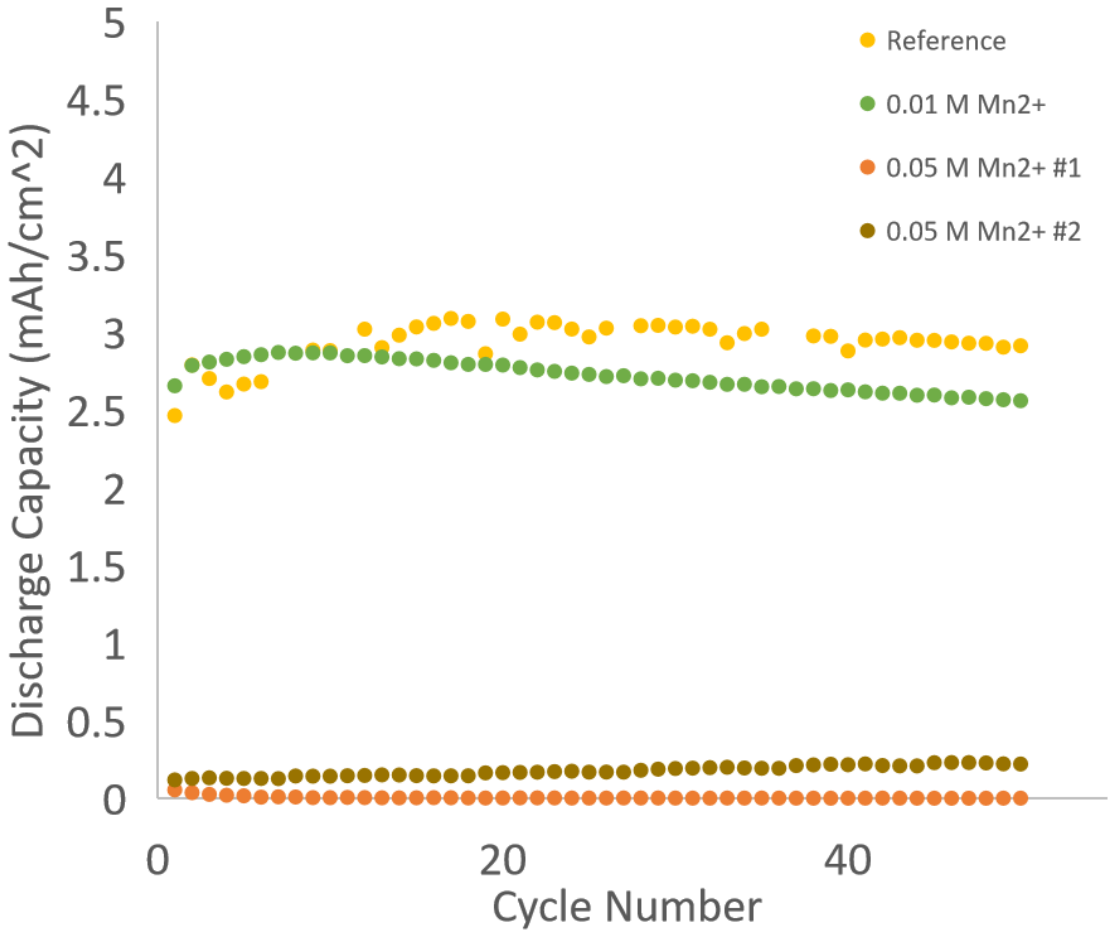

The higher the concentration of dissolved manganese ions, the greater the impact on battery performance. The charge-discharge performance with 0.01 M manganese ions can still maintain a stable state, but overall, it shows a noticeable downward trend compared to pristine electrolyte. High concentrations of manganese ion contamination (0.05 M) heavily limit the battery life at the start. Additionally, in the initial stage, it requires a longer discharge time to reach 2.7 V. It is hypothesized that this extra discharge stage is needed for the reduction of some solid electrolyte interface layers. Subsequent data also measure the impact of manganese ions on the electrolyte from the perspective of different concentrations.

3.3.2 1D Scan and T1 Relaxation time

For ^{7}Li NMR, electrolytes with high and low concentration contaminants were subjected to diffusion tests under different temperature ranges. Through the 1-dimensional spectrum, it can be clearly observed that electrolytes contaminated with manganese have a positive shift shown in Figure 16. The unpaired electrons in transition metals produce a magnetic moment that can interact with nearby nuclear spins, leading to a shift in the resonance frequency. This interaction can be either through dipolar coupling or through the Fermi-contact interaction. For Mn^{2+}, it has unpaired d-electrons that can give rise to Para-magnetism. This can influence the chemical shift of nearby nuclei, resulting in a paramagnetic shift.

The presence of Mn^{2+} ions, which are paramagnetic due to their unpaired electrons, significantly affects the relaxation processes in NMR. Paramagnetic ions like Mn^{2+} can induce faster relaxation of nearby nuclear spins, leading to shorter T1 (longitudinal relaxation time)[10,11] in the sample containing Mn^{2+}. In the sample without Mn^{2+}, relaxation times might be longer, as the relaxation mechanisms are primarily determined by dipole-dipole interactions among nuclear spins or interactions with the lattice, rather than paramagnetic relaxation processes. The shortened relaxation times in the presence of Mn^{2+} ions can lead to broader NMR signals due to faster dephasing of the nuclear spins. This can decrease the resolution of the NMR spectrum, making it harder to distinguish between closely spaced signals. In contrast, the sample without Mn^{2+} may exhibit sharper and more resolved peaks, assuming other factors that affect line width (like molecular motion or homogeneity of the magnetic field) are kept constant. Paramagnetic ions such as Mn^{2+} can also cause shifts in the NMR signals' chemical shift, known as the paramagnetic shift. This effect can complicate the interpretation of the chemical environment around the nuclei. The sample without Mn^{2+} will not exhibit paramagnetic shifts, and its chemical shift values will be primarily influenced by the electronic environment surrounding the nuclear spins.

Similarly, the same level of shift is also present in two other transition metals. Through the electronic configuration, Fe^{2+} has four unpaired electrons, while Cu^{2+} has one unpaired

electron. Theoretically, Fe^{2+} should have a larger paramagnetic shift compared to Cu^{2+}. However, what we observed from the 1-dimensional spectrum is that Cu^{2+} exhibits a larger positive shift in Figure 17. Since the chemical environments of the two electrolytes are similar, with the same cations, the cause of this shift could be due to direct through-space dipolar coupling. This can occur if the unpaired electron of Cu^{2+} has a strong magnetic interaction with the observed nucleus, which could cause a larger shift.

Figure 16. ^{7}Li (at 7.05 T with a nominal ^{7}Li frequency of 116.7 MHz) 1D Spectrum at room temperature, the chemical shift of high-concentration manganese ion dissolved electrolyte shows a positive shift due to the paramagnetic effect. The green peak represents the reference electrolyte, and the 0.1M lithium ion control group electrolyte shows no change in chemical shift.

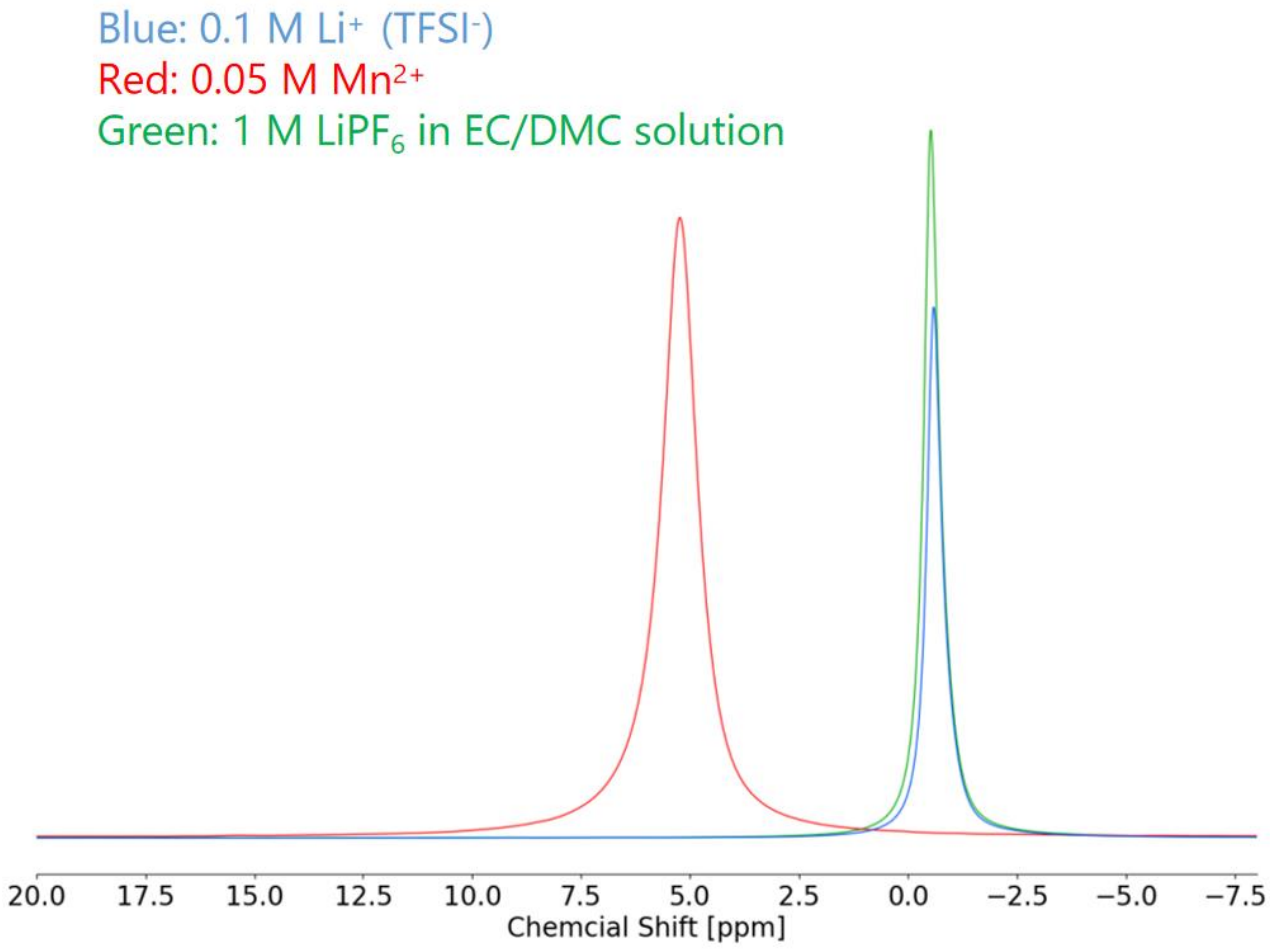

Figure 17. ^{7}Li (at 7.05 T with a nominal ^{7}Li frequency of 116.7 MHz) 1D Spectrum at room temperature, the chemical shift of low-concentration iron ions and copper ions dissolved in the electrolyte shows a positive shift due to the paramagnetic effect. The 0.02M lithium ion control group electrolyte is shown in blue. The other two indicate that copper causes a larger positive change, while iron shows a relatively smaller shift.

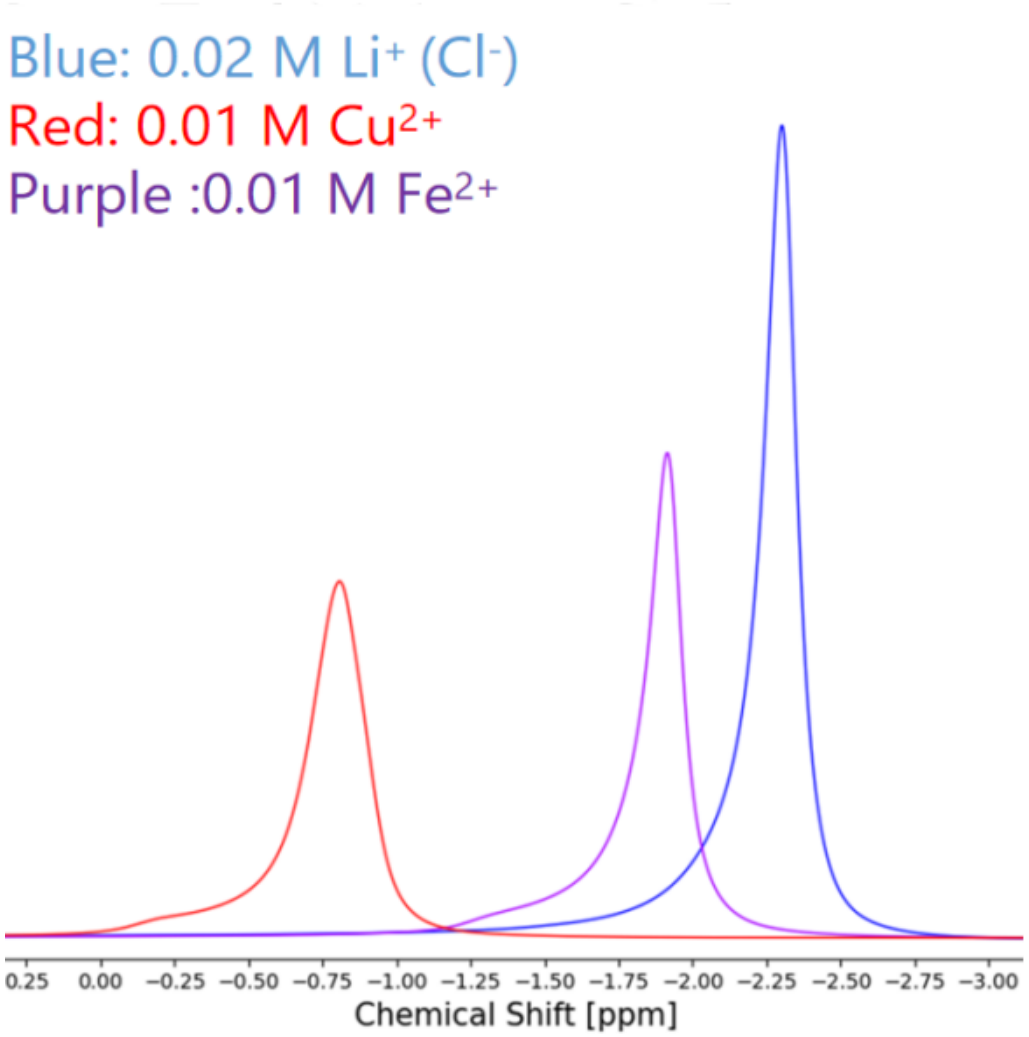

3.3.3 ^{7}Li PFG-NMR on Electrolyte

Through the Arrhenius plot in Figure 18, it can be observed that in the group of high concentration electrolytes, the electrolyte contaminated with manganese shows a significant decrease in the diffusion coefficient. However, by looking at the linear slopes corresponding to each, there is no change in the activation energy of the manganese-containing electrolyte.

In contrast, the decrease is not as pronounced for the electrolyte with low concentration contaminants. In Figure 19, the three linear relationships nearly overlap, showing that at low contaminant concentrations, manganese does not impact the diffusivity of the electrolyte.

Two potential contaminants were also subjected to variable temperature tests under the same two concentration groups. In the electrolyte with a high concentration of copper, $CuCl_2$ did not completely dissolve, and there were noticeable suspensions in the solution. Therefore, there is no comparable data in the high concentration tests for copper. Refer to Figure 19, although data was obtained for high concentration Fe^{2+}, its linear relationship almost overlaps with the base electrolyte. There are two hypotheses about the changes in high concentration Fe^{2+}: one is that Fe^{2+} did not completely dissolve into the electrolyte; the other is that Fe^{2+} does not affect the diffusion coefficient of the electrolyte. In combination with the content in Figure 19, among the low concentration group, the electrolyte containing Fe^{2+} shows the most significant decrease in the diffusion coefficient. This proves that the electrolyte with high concentration Fe^{2+} did not completely dissolve. For the group with low concentration, electrolytes containing Cu^{2+}, Fe^{2+} and Li^{+} all present the same linear slope, so their corresponding activation energies are also the same. However, comparatively, the activation energy of the base electrolyte is lower.

Figure 18. (^{7}Li Result) The two sets of data show the behavior of the high concentration group (0.05M) under varying temperatures. The red color represents the electrolyte containing manganese ions, which shows a significant decline. The purple electrolyte containing iron ions and the control group lithium ion solution exhibit similar behavior, but both are slightly higher than the reference electrolyte.

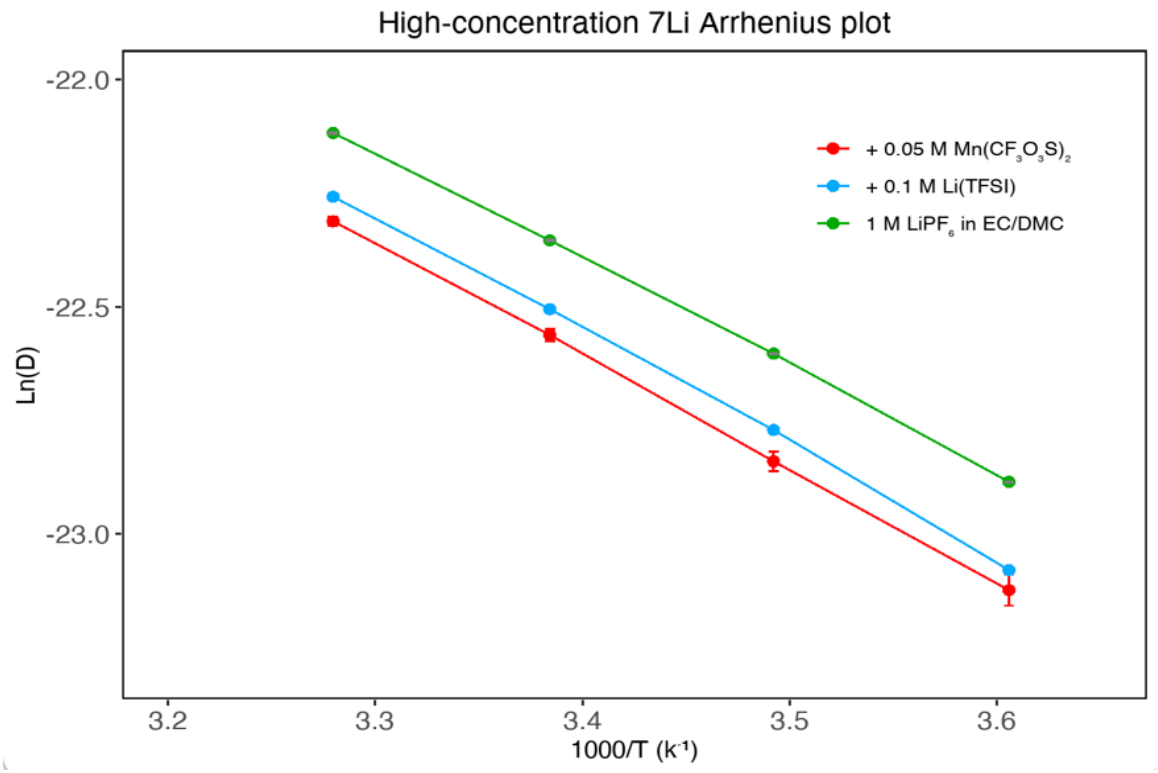
High-concentration 7Li Arrhenius plot
-22.0
-22.5
-23.0
Ln(D)
3.2
3.3
3.4
3.5
3.6
1000/T (k⁻¹)
+ 0.05 M Mn(CF3O3S)2
+ 0.1 M Li(TFSI)
1 M LiPF6 in EC/DMC

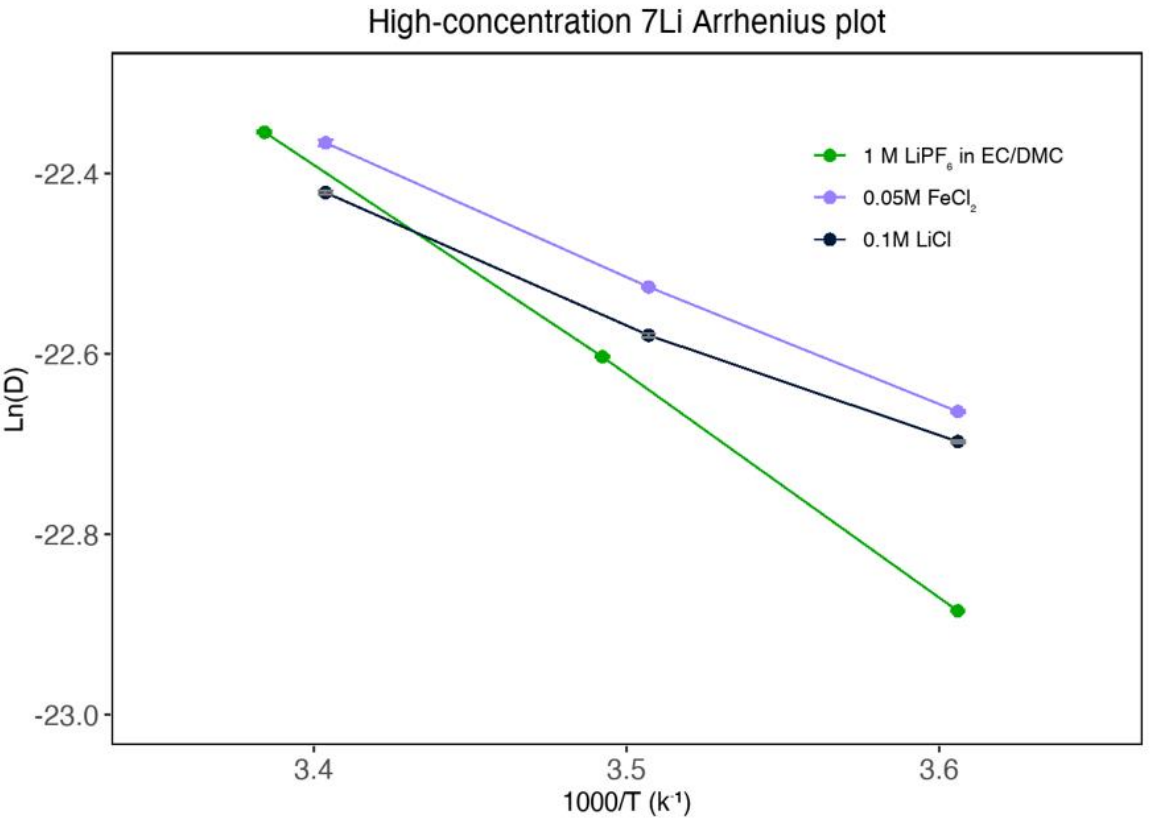
High-concentration 7Li Arrhenius plot
-22.4
-22.6
-22.8
-23.0
Ln(D)
3.4
3.5
3.6
1000/T (k⁻¹)
1 M LiPF6 in EC/DMC
0.05M FeCl2
0.1M LiCl

Figure 19. (^{7}Li Result) The two sets of data represent the behavior of the low concentration group under varying temperatures. Manganese ions show a significant difference at low temperatures, with all groups becoming very close at higher temperatures. Copper ions and iron ions both exhibit a marked decline in behavior at low concentrations, with the decline being more pronounced for iron ions.

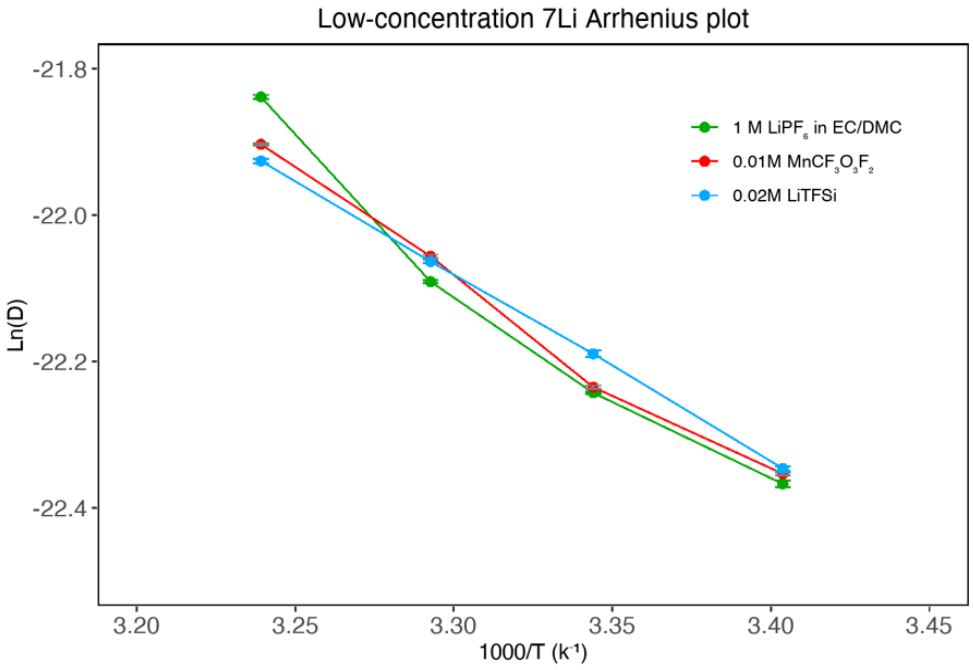

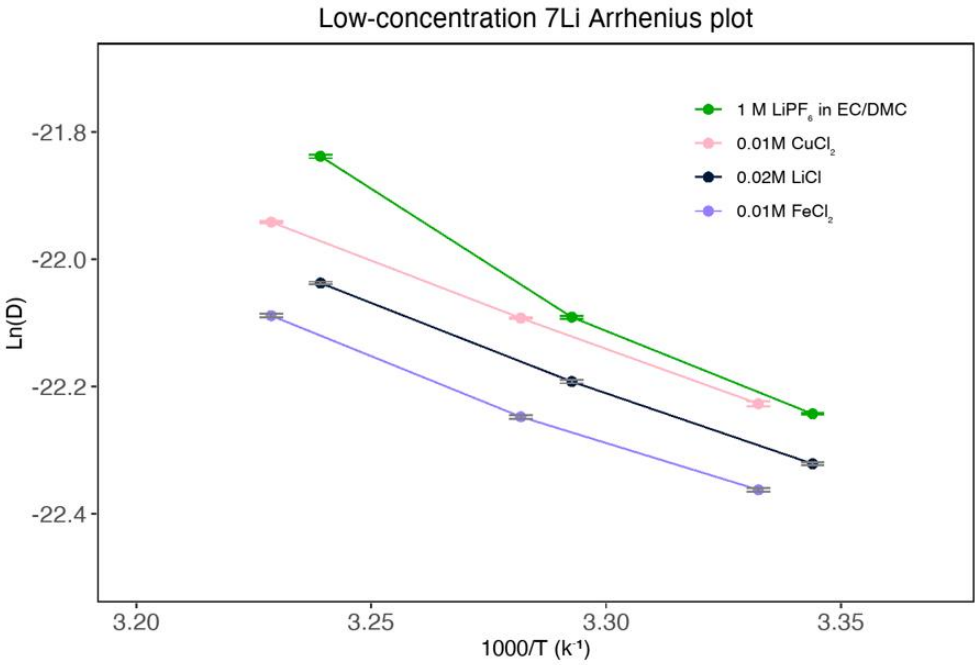

3.3.4 Variable temperature experiment & activation Energy

Combining all the ^{7}Li data and the summary in the table, it can be observed that electrolytes contaminated with transition metals affect the diffusion of Li-ion in the electrolyte at different concentrations. Moreover, in the low concentration group, the contaminants also increase the activation energy for diffusion. Interestingly, in Table 4, contaminants containing Fe^{2+} have a faster T1 relaxation time. Theoretically, the involvement of Fe^{2+} should not have such a significant effect on the value of T1. This is because Fe^{2+} has an electronic configuration of $3d^6$ which results in a partially filled d-orbits. In most coordination environments, Fe^{2+} tends to adopt a high- spin state which will have a relatively small magnetic moment.

Sample	T1 Relaxation (ms)	Ea (eV)
1 M $LiPF_6$ in EC/DMC	1750 ± 0.6	(0.203±0.003)
+ 0.05 M Mn^{2+}	31 ± 0.1	(0.215±0.002)
+ 0.1 M Li^{+} (TFSI)	1440 ± 0.8	(0.217±0.005)
+ 0.05 M Fe^{2+}	1056 ± 0.4	(0.178±0.02)
+ 0.1 M Li^{+} (Cl)	1876 ± 0.6	(0.176±0.02)

Table 4. (^{7}Li Result) At a temperature of 303K, the T1 relaxation time of each sample is given in milliseconds (ms), along with the activation energy required for lithium ion diffusion within a fixed temperature range (top: 278-303K, bottom: 278-298K).

Sample	T1 Relaxation (ms)	Ea (eV)
1 M $LiPF_6$ in EC/DMC	1750 ± 0.6	(0.203±0.003)
+ 0.01 M Mn^{2+}	280 ± 0.4	(0.24±0.02)
+ 0.01 M Li^{+} (TFSI)	1850 ± 0.5	(0.220±0.002)
+ 0.01 M Cu2^{+}	1100 ± 0.3	(0.237±0.004)
+ 0.01 M Fe^{2+}	260 ± 0.7	(0.23±0.02)
+ 0.02 M Li^{+} (Cl)	1730 ± 0.9	(0.234±0.009)

Table 5. (^{7}Li Result) At a temperature of 278K, the T1 relaxation time of each sample is given in milliseconds (ms), along with the activation energy required for lithium ion diffusion within a fixed temperature range (top: 293-308K, bottom: 293-208K).

Sample	ΔD (m^2/s)	Percentage loss
+ 0.05 M Mn^{2+}	-3.68E-11	-14.84%
+ 0.05 M Fe^{2+}	-2.30E-12	-1.17%

Table 6. (^{7}Li Result) At a temperature of 293K, the changes in the diffusion coefficient caused by the dissolution of high-concentration transition metal ions into the electrolyte, and the percentage change compared to the reference electrolyte.

Sample	ΔD (m^2/s)	Percentage loss
+ 0.01 M Mn^{2+}	-1.03E-11	-4.46%
+ 0.01 M Cu^{2+}	-3.22E-11	-9.82%
+ 0.01 M Fe^{2+}	-7.26E-11	-22.14%

Table 7. (^{7}Li Result) At a temperature of 298K, the changes in the diffusion coefficient caused by the dissolution of low-concentration transition metal ions into the electrolyte, and the percentage change compared to the reference electrolyte.

3.3.5 ^{1}H PFG-NMR on electrolyte

Wang's work[28] mentioned the propensity of Mn and anions in forming solvation sheaths in carbonate electrolyte. This paper used tests of EC's electron affinity with Li^{+} and Mn^{2+} to illustrate that EC is the substance with which Mn^{2+} is more favorable to form a solvation sheath in the electrolyte. This is also a reason contaminant can compete with Li-ions in the electrolyte. Similarly, using proton diffusion experiments with the electrolyte containing Mn^{2+} as a reference. If the electrolyte containing Cu and Fe shows the same diffusion loss on EC and DMC, it can be preliminarily inferred what causes the decrease in diffusion in their electrolytes. The chemical environment in the electrolyte was observed by examining the chemical shift of the EC and DMC peaks.

Figure 20. The ^{1}H (at 7.05 T with a nominal ^{1}H frequency of 300 MHz) NMR spectra collected at room temperature show two peaks representing EC and DMC in the electrolyte. The diffusion coefficients of each peak were fitted separately to compare the changes.

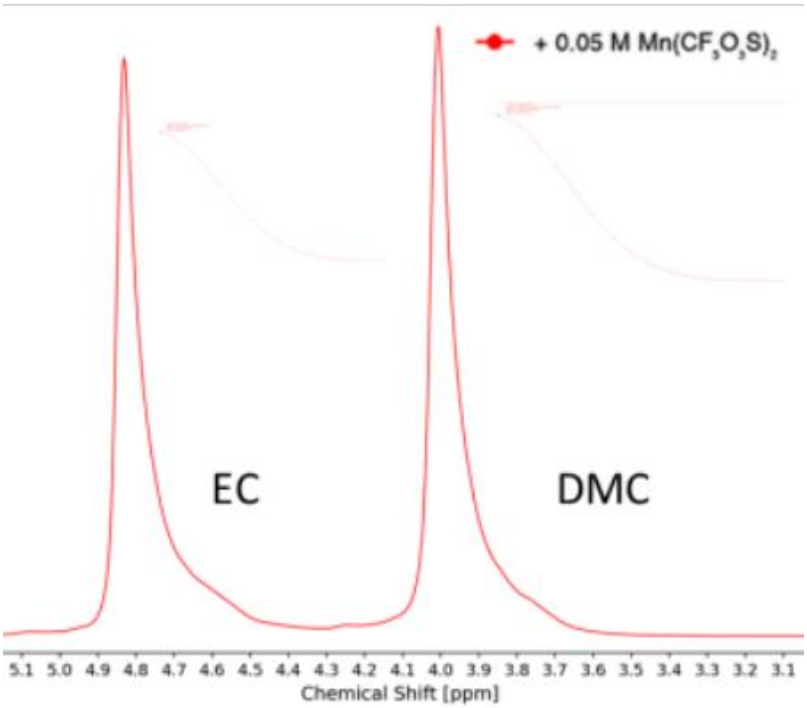

Sample	T1 Relaxation (ms) @ RT	T1 Relaxation (ms) EC	T1 Relaxation (ms) DMC
1 M LiPF6 in EC/DMC	(2333±0.9)	(1939±0.4)	(2791±0.1)
+0.01 M Mn^{2+}	(132.1±0.2)	(150.3±0.1)	(116.7±0.3)
+ 0.01 M Cu^{2+}	(579.8±0.4)	(570.1±0.5)	(600.6±0.3)
+0.01 M Fe^{2+}	(1257±0.7)	(1022±0.5)	(1522±0.6)
+ 0.02 M Li^{+} (Cl)	(2039±0.8)	(1751±0.5)	(2410±0.1)

Table 8. (Proton NMR Results) At room temperature, the changes in T1 relaxation time caused by the dissolution of low-concentration transition metal ions into the electrolyte, and the respective changes in EC and DMC.

Sample	Chemical Shift EC (ppm)	Chemical Shift DMC (ppm)	D (EC) m^2/s	D (DMC) m^2/s
1 M $LiPF_6$ in EC/DMC	4.72	3.89	(4.72±0.07) E-10	(5.82±0.09) E-10
+ 0.01 M Mn^{2+}	4.83	3.99	(4.50±0.03) E-10	(5.48±0.04) E-10
+ 0.01 M Cu^{2+}	4.71	3.89	(3.20±0.04) E-10	(3.84±0.02) E-10
+ 0.01 M Fe^{2+}	4.84	4.02	(4.39±0.04) E-10	(5.42±0.04) E-10
+ 0.02 M Li^{+} (Cl)	4.71	3.91	(4.38±0.04) E-10	(5.41±0.07) E-10

Table 9. (Proton NMR Results) At room temperature, the chemical shifts and diffusion coefficients of EC and DMC after the dissolution of low-concentration transition metal ions into the electrolyte.

Sample	ΔD (EC) m^2/s	Percentage loss	ΔD (DMC) m^2/s	Percentage loss
+ 0.01 M Mn^{2+}	-2.20E-11	-4.66%	-3.43E-11	-5.89%
+ 0.01 M Cu^{2+}	-1.52E-10	-32.18%	-1.99E-10	-34.13%
+ 0.01 M Fe^{2+}	-3.27E-11	-6.93%	-4.08E-11	-7.01%

Table 10 (Proton NMR Results). At room temperature, the changes in the diffusion coefficients collected for the EC and DMC peaks after the dissolution of low-concentration transition metal ions into the electrolyte, and the percentage change compared to the reference electrolyte.

Through Tables 8 and 9, Fe^{2+} and Mn^{2+} have similar degrees of decrease in EC and DMC, and they also have similar chemical shifts. However, the introduction of copper results in a more pronounced decline in both EC and DMC; and a significant impact on the diffusion data of Li. Based on the diffusion data from proton NMR, we can only speculate that Fe and Mn play similar roles in the electrolyte, while copper does not. Based on the above results, proton NMR cannot intuitively observe whether there is a competitive behavior between copper ions, iron ions, and lithium ions similar to that of manganese ions. Moreover, from a comparative perspective, the impact of copper ions on EC and DMC far exceeds that of the other two transition metals. Therefore, no more diffusion data will be collected using proton NMR, and instead, practical battery tests will be conducted based on the observed performance of manganese ions.

3.3.6 ^{7}Li PFG-NMR on Working cells

The above experiment was conducted specifically on the electrolyte and measured in a homogeneous state within NMR tubes. To simulate the actual conditions of battery usage, a pencil cell design was employed, which is well-suited for testing the chemical environment of the electrolyte.

NMR experiments collected results before and after charging. A comparison revealed that the battery using the reference electrolyte experienced a 6% loss in diffusion coefficient. This reduction could be due to the formation of the solid electrolyte interface (SEI), which consumes some lithium, leading to a certain degree of lithium depletion in the electrolyte. It could also result from the electrolyte degrading slightly during the first two cycles. In contrast, the electrolyte containing 0.01 M manganese ions showed a more significant decrease before and after charging. The bar chart indicated in red represents the presence of manganese ions. The 25% reduction clearly demonstrates that the electrolyte with manganese ions lost a significant amount of lithium available for battery operation, confirming the initial hypothesis of the experiment.

Additionally, during the experimental phase, the spectra collected from the manganese-containing electrolyte under NMR had a very poor signal-to-noise ratio, requiring higher gradient

strengths and a greater number of scans to convert the one-dimensional spectra collected at different gradients into diffusion curves. In simple terms, the paramagnetic effect of 0.01M manganese ions made data collection more difficult, with broader peaks and weaker signal intensity.

It was clearly observed that adding manganese-ions accelerated the electrolyte's degradation. Although the battery could charge normally, the signal intensity was no longer sufficient for data analysis. Due to these considerations, the 0.05 M manganese ion electrolyte previously tested in the NMR tube showed significant effects. Thus, this electrolyte was also tested in the pencil cell, resulting in the battery failing to survive even one charge-discharge cycle.

Figure 21. Comparison of lithium diffusion coefficients in the pencil cell before and after two sets of charge-discharge cycles. On the left is the reference electrolyte, showing a 6% decrease in the diffusion coefficient before (left) and after (right) the charge cycle. On the right is the case with the addition of 0.01M manganese ions, showing a 25% decrease in the diffusion coefficient.

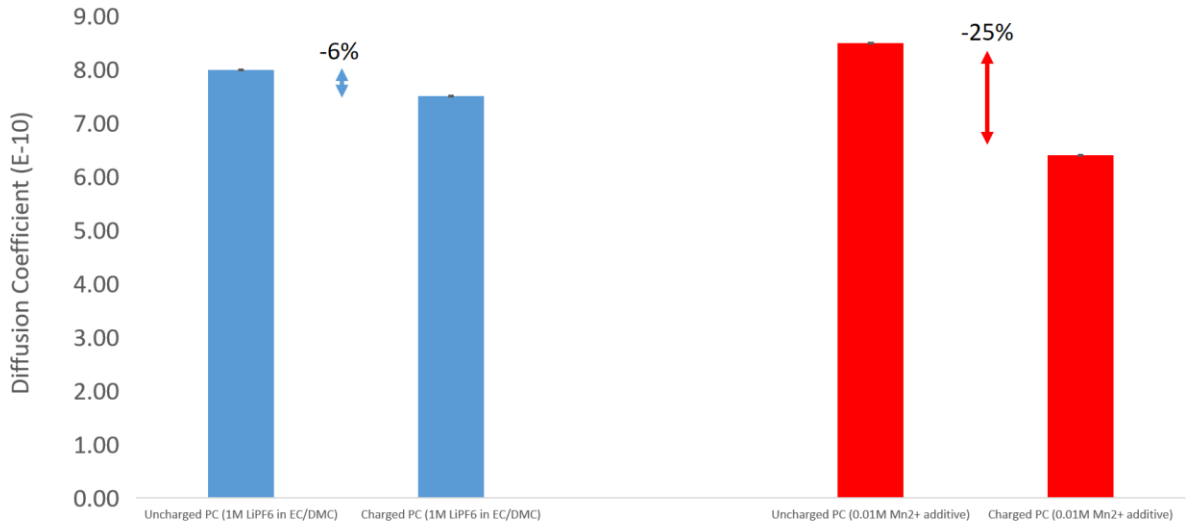

Cell	In NMR tube (electrolyte only)	Pencil cell (before charge)	Pencil Cell (after charge)	T1 Relaxation time (ms)
Pristine electrolyte full cell	D: (8.21±0.06) E-10	D: (7.99±0.01) E-10	D: (7.49±0.08) E-10	2739
+ 0.01 M Mn electrolyte full cell	D: (8.82±0.02) E-10	D: (8.49±0.07) E-10	D: (6.4±0.5) E-10	101
+ 0.01 M Mn electrolyte full cell after 3 weeks	/	D: (5.42±0.03) E-11	/ (really low signal to noise ratio)	26

Table 11. (^{7}Li Result) Changes in the tested electrolyte after different storage periods under the same storage conditions. The electrolyte containing 0.01 M manganese ions showed significant changes when retested three weeks after the end of the experiment, and the collected spectral signal intensity was very low.

3.4 Reference

14. Liao, Y., Zhang H., Peng Y., *et al.* Electrolyte Degradation During Aging Process of Lithium-Ion Batteries: Mechanisms, Characterization, and Quantitative Analysis. *Advanced Energy Materials* vol. 14 Preprint at https://doi.org/10.1002/aenm.202304295 (2024).

15. Solchenbach, S., Hong, G., Freiberg, A. T. S., Jung, R. & Gasteiger, H. A. Electrolyte and SEI Decomposition Reactions of Transition Metal Ions Investigated by On-Line Electrochemical Mass Spectrometry. *J Electrochem Soc* **165**, A3304–A3312 (2018).

28. Wang, C., Xing L., Vatamanu J., *et al.* Overlooked electrolyte destabilization by manganese (II) in lithium-ion batteries. *Nat Commun* **10**, 3423 (2019).

32. Ohkubo, T., Gobet M., Sarou-Kanian., *et al.* Self-diffusion coefficient of lithium in molten xLi 2O-(1 - X)B 2O 3 system using high-temperature PFG NMR. *Chem Phys Lett* **530**, 61–63 (2012).

33. Bazak, J. D., Allen, J. P., Krachkovskiy, S. A. & Goward, G. R. Mapping of Lithium-Ion Battery Electrolyte Transport Properties and Limiting Currents with In Situ MRI. *J Electrochem Soc* **167**, 140518 (2020).

34. Krachkovskiy, S., Dontigny M., Rochon S., *et al.* Determination of Binary Diffusivities in Concentrated Lithium Battery Electrolytes via NMR and Conductivity Measurements. *Journal of Physical Chemistry C* **124**, 24624–24630 (2020).

35. Kaysan, G., Rudszuck T., Trapp L., *et al.* Recent applications of NMR diffusion experiments. in *Annual Reports on NMR Spectroscopy* vol. 107 47–93 (Academic Press Inc., 2022).

56. Stallmach, F. & Galvosas, P. Spin Echo NMR Diffusion Studies. *Annual Reports on NMR Spectroscopy* vol. 61 51–131 Preprint at https://doi.org/10.1016/S0066-4103(07)61102-8 (2007).

57. Haaks, M., Martin, S. W. & Vogel, M. Relation of short-range and long-range lithium ion dynamics in glass-ceramics: Insights from Li 7 NMR field-cycling and field-gradient studies. *Phys Rev B* **96**, (2017).

58. Van Der Ven, A., Bhattacharya, J. & Belak, A. A. Understanding Li diffusion in Li-intercalation compounds. *Acc Chem Res* **46**, 1216–1225 (2013).

59. Gachot, G., Ribiere P., Mathiron D., *et al.* Gas chromatography/mass spectrometry as a suitable tool for the li-ion battery electrolyte degradation mechanisms study. *Anal Chem* **83**, 478–485 (2011).

60. Huang, D., Engtraku C., Nanayakkara S., *et al.* Understanding Degradation at the Lithium-Ion Battery Cathode/Electrolyte Interface: Connecting Transition-Metal Dissolution Mechanisms to Electrolyte Composition. *ACS Appl Mater Interfaces* **13**, 11930–11939 (2021).

61. Solchenbach, S., Hong, G., Freiberg, A. T. S., Jung, R. & Gasteiger, H. A. Electrolyte and SEI Decomposition Reactions of Transition Metal Ions Investigated by On-Line Electrochemical Mass Spectrometry. *J Electrochem Soc* **165**, A3304–A3312 (2018).

62. Cabana, J., Kwon, B. J. & Hu, L. Mechanisms of Degradation and Strategies for the Stabilization of Cathode-Electrolyte Interfaces in Li-Ion Batteries. *Acc Chem Res* **51**, 299–308 (2018).

63. Joshi, T., Eom, K., Yushin, G. & Fuller, T. F. Effects of Dissolved Transition Metals on the Electrochemical Performance and SEI Growth in Lithium-Ion Batteries. *J Electrochem Soc* **161**, A1915–A1921 (2014).

64. Von Wald Cresce., Gober M., Borodin O., A. *et al.* Anion Solvation in Carbonate-Based Electrolytes. *Journal of Physical Chemistry C* **119**, 27255–27264 (2015).

65. Komaba, S., Kumagai, N. & Kataoka, Y. *Influence of Manganese(II), Cobalt(II), and Nickel(II) Additives in Electrolyte on Performance of Graphite Anode for Lithium-Ion Batteries*. *Electrochimica Acta* vol. 47 www.elsevier.com/locate/electacta (2002).

66. Allen, J. P., O'Keefe, C. A. & Grey, C. P. Quantifying Dissolved Transition Metals in Battery Electrolyte Solutions with NMR Paramagnetic Relaxation Enhancement. *The Journal of Physical Chemistry C* (2023) doi:10.1021/acs.jpcc.3c01396.

67. Burlamacchi, L. & Tiezzi, E. *PROTON SPIN RELAXATION TIMES (Tt; T2) AND Mn Z+ COMPLEXES IN SOLUTION: PMR AND PULSED NMR STUDIES**. vol. 31 (1969).

68. Böttjer, T., Lehmann, G. & Stockhausen, M. *An Electron Paramagnetic Resonance Study of Mn 2 + Ions Doped in Langbeinites The Cubic (High Temperature) Phase of Some Langbeinites, A 2 B 2 + (S0 4) 3 with 11 Different Combi-Nations of A and B Type Cations, Doped with Mn 2+*. *Z. Naturforsch* vol. 47 (1992).

69. Furman, G. B., Goren, S. D., Meerovich, V. M. & Sokolovsky, V. L. Dipolar nuclear polarization via the spin diffusion of a dipole order. *Journal of Magnetic Resonance* **320**, (2020).

70. Krachkovskiy, S. A., Foster, J. M., Bazak, J. D., Balcom, B. J. & Goward, G. R. *Operando* Mapping of Li Concentration Profiles and Phase Transformations in Graphite Electrodes

by Magnetic Resonance Imaging and Nuclear Magnetic Resonance Spectroscopy. *Journal of Physical Chemistry C* **122**, 21784–21791 (2018).

Chapter4

In *Operando* NMR Study with different discharge algorithms

4.1 Introduction

The previous discussion focused on the materials of the cathode and electrolyte. However, there are many challenges when it comes to the Battery Management System (BMS) of batteries. With the increasing number of electric vehicles, improving charging rates to enhance vehicle utilization has become a key goal for all battery manufacturers. Compared to fast charging[72,73], conventional full charging takes about 6-8 hours, while fast charging increases the charging current, enabling the vehicle to reach the same capacity in a shorter time. The essence of a battery is the redox reaction of lithium ions, and frequent fast charging weakens the battery's ability to reduce. While fast charging is well-discussed so far, rapid discharging is less explored. What impact does changing the discharge rate have on the battery; this is an uncharted gray area. Because all the issues are unknown, testing is needed to determine how changing the discharge rate affects electrochemical performance or the components within the battery. Under this setup, the *operando* experiment setting can perfectly meet this requirement. Specifically, changing the discharge rate refers to discharging the battery in a pulsed manner. This involves discharging the battery rapidly for a period, then resting for a period before discharging rapidly again. The discharge rate is adjusted during these intervals, and the corresponding discharge time is also modified (as shown in the figure 22). This discharge algorithm is known as pulse discharge (PD). Nuclear Magnetic Resonance is a very advantageous technique for observing changes in lithium batteries. As mentioned earlier, NMR can track changes in the electrolyte and lithium metal within the battery. It is hypothesized that lithium batteries might experience different growth rates of the solid electrolyte interphase during pulse discharge. Additionally, the surface morphology of lithium metal may also change. These two points can be considered the biggest challenges faced by fast charging. If the battery can maintain health under the fast discharge algorithm, the most likely reason is changes in these two areas[74].

Figure 22. Diagram showing the difference between pulse discharge and constant discharge, with current on the y-axis and time on the x-axis.

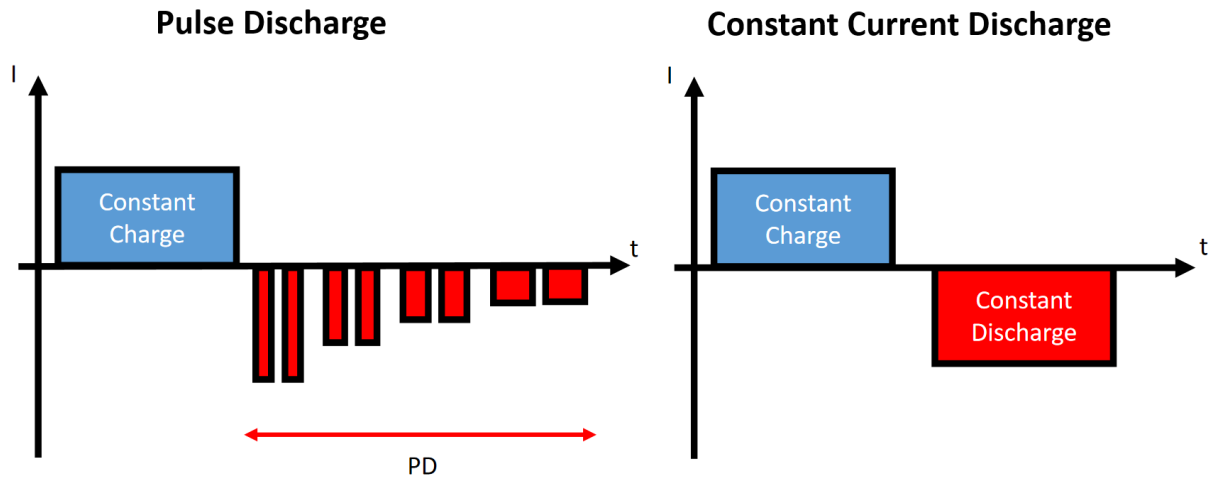

4.2 Experimental

A distribution diagram of a parallel-plate resonator made of PEEK material under B1 magnetic field is shown in the figure 23. The specific design is depicted in Figure at the bottom. As can be seen, this consists of a set of parallel PEEK plates, each 50 mm long and 20 mm wide, with a 7.0 mm gap between them. Capacitors are placed at each end corner, connected to the current to enhance the B1 field between the two plates. A cartridge cell, fitting perfectly, is placed in the 7 mm gap, as shown in Figure 23.

The cartridge cell's size allows it to be vertically placed into the *operando* probe designed by the Dr.Goward group[75]. The working electrode and counter electrode can be connected from both ends of the battery inside the probe to the external Gamry instrument, enabling *operando* experiments (simultaneously achieving charging and discharging while collecting NMR spectra). This battery has good sealing properties and is also made of PEEK material, ensuring the accuracy and stability of the collected NMR spectra. The cartridge cell design perfectly incorporates all the components of a conventional liquid battery: cathode, anode electrolyte, separator, and current

collector (it can also be set up as a three-electrode battery to accommodate an additional reference electrode). This battery, capable of performing *operando* experiments, allows a clear observation of the changes in the electrolyte, lithium metal, and various solid layers inside the battery during different charging and discharging stages and rates. Additionally, using other NMR software (ssNake[76]), the collected spectra can be fitted to quantify the changes in these components.

Figure 23 Top: Parallel-plate resonator RF probe used to hold the cartridge cell.

Bottom: Top and bottom views of the cartridge cell

6. *The design for injecting electrolyte, sealed in advance with resin.*
7. *The location of the current collector wiring.*
8. *The screw position for sealing and closing the battery.*
9. *The reserved O-ring position to enhance sealing.*
10. *The reserved holes to help align the battery during assembly.*

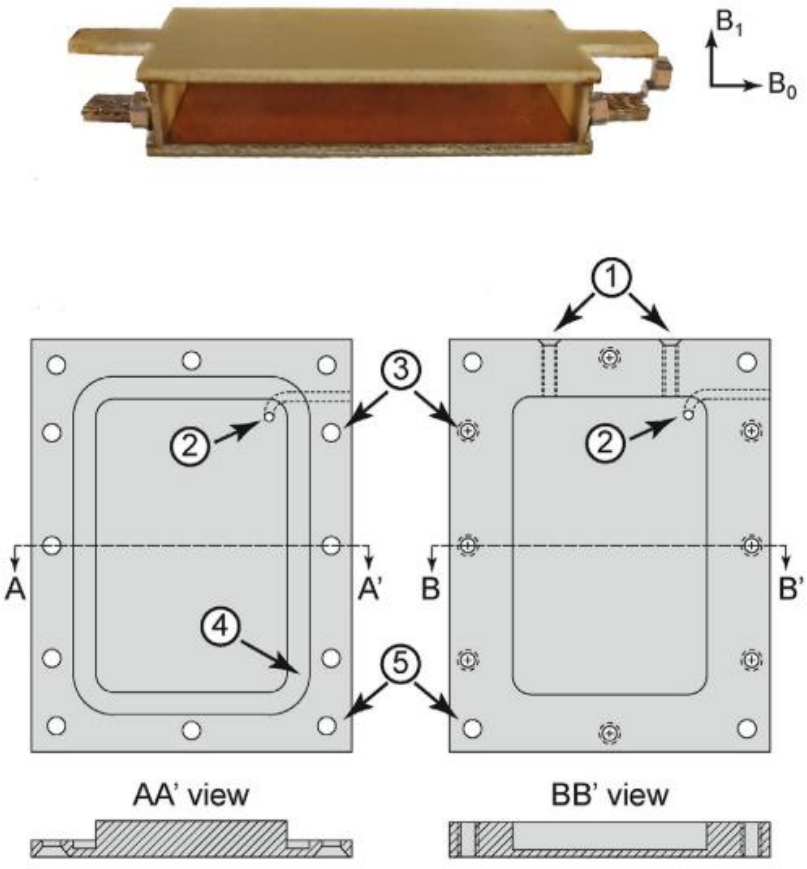

The cartridge cell is designed as a sealed system with the capability to replenish the electrolyte at any time (this function is not needed here and is sealed with Araldite 2014 epoxy resin). Eight PEEK screws are used to ensure the battery's sealing and good contact, and an ethylene propylene diene monomer (EPDM) rubber O-ring[75,77] is used to seal the position marked as number 4 in Figure 23, ensuring that the battery maintains good sealing after pressure is applied.

Figure 24. Diagram of the field strength distribution calculated for the parallel-plate resonator. The dashed line indicates the placement area of the cartridge cell, ensuring a uniform field strength.

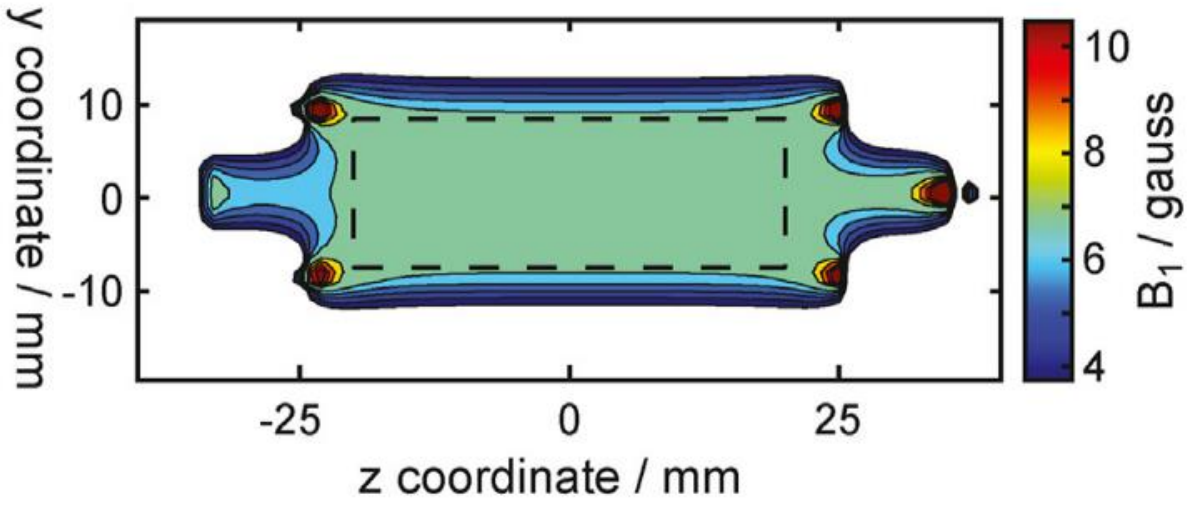

The materials intended for the cartridge cell preparation include cathode LiNi0.5Mn0.3Co0.2O2 (NMC532, 1.8 mAh/cm²) and a uniformly thick piece of lithium metal weighing approximately 0.1 g as the anode. It's important to note the size relationships of the electrodes to ensure the successful charging of this half-cell. The size control of materials is as follows: NMC532 (1.4*2.5 cm²) < lithium metal < separator (2.1*3.2 cm²) (represented by a copper current collector of the same size in the figure 24).

Before assembly, all battery components are vacuum stored in a 120°C oven for over 15 hours to ensure all moisture is removed. The assembly process is carried out in an Ar-filled glove box, using two pre-prepared separators and a total of 300 µL electrolyte. Typically, the cartridge

cell configuration includes placing an aluminum current collector on the cathode and a copper current collector under the anode. This design promotes good contact within the battery. However, for this project, which tests a half-cell (where the lithium metal thickness is greater than that of the anode), therefore, during the assembly process, the copper current collector was removed to ensure good sealing. Subsequent NMR data proved the feasibility of this optimization.

Figure 25. Diagram of the electrode sizes in the battery, with the copper current collector used as a size reference (it is the same size as the separator). On the right is the NMC532 cathode.

After preparing the cartridge cell, it will be placed into the previously mentioned parallel-plate RF probe, and then inserted into the NMR magnet. The copper and aluminum wires at both ends of the battery are connected to the pre-designed counter electrode and working electrode ports on the probe. Two external wires will then connect the probe ends to the Gamry Interface 1000E potentiostat for electrochemical testing. While charging and discharging, NMR spectra will be collected, defined here as an *operando* NMR experiment.

Electrochemically, both tests start with a C/20 formation cycle. The cell will charge at a constant current rate of C/20 up to 4.2V, then rest under open circuit voltage conditions for 30 minutes. It will then discharge at a constant current rate of C/20 down to 2.7V, followed by another 30-minute rest under open circuit voltage conditions, and then repeat the cycle. The formation cycle consists of only two cycles, and both batteries in the comparative experiment are identical in this regard. The difference lies in the conventional charge-discharge stage. Specifically, only the discharge phase differs. Each charging cycle involves charging at a constant

current to 4.2V, followed by a constant voltage phase until the current drops to C/6, and then a 30-minute rest under open circuit voltage conditions before discharging. One battery undergoes pulse discharge, while the other undergoes constant current discharge down to 2.7V.

The NMR experiment is conducted at room temperature using a Bruker Avance III HD wide-bore instrument at 7.05 T with a nominal ^{7}Li frequency of 116.7 MHz. One-dimensional spectra will be collected and calibrated to 0 ppm based on the electrolyte peak position. The Ernst angle (pulse tip angle of 30 degrees) and recycle delay will be set to 500 ms, based on the T1 relaxation times of lithium metal and the electrolyte, to achieve the best signal-to-noise ratio. For the constant current discharge, NMR spectra will be collected every three minutes, while for the pulse discharge, spectra will be collected every minute. The collected 1D spectra will then be fitted using ssNake.

4.3 Results and Discussion

4.3.1 ^{7}Li *Operando* Experiment

The essence of the ^{7}Li *operando* experiment in this work is to continuously collect 1D spectra during the charge and discharge processes. As shown in the figure 26, there are two peaks: one from the -15 to 10 ppm region, representing the electrolyte peak, marked in gray, and the other from the 250 to 290 ppm region, representing the lithium metal peak[58,59], marked in green. The spectrum shown in the figure 26 is captured during discharge. By fitting the gray peak with ssNake, it can be observed that this gray peak consists of an electrolyte peak (blue) and a broad peak of the solid electrolyte interphase (SEI) layer (orange) around 0 ppm. The green peak can be split into a metallic lithium peak (brown) and a mossy lithium peak formed during charging (red).

Discussing the two peaks separately, as shown in the figure 27, the three stages within the first charge-discharge cycle of the battery are displayed in overlapping colors: the initial state (green), the top of charge (blue), and the bottom of discharge (yellow). On the left side, representing the breathing changes of lithium metal, at the start, no mossy lithium is formed, so

the shoulder at the lower right is not visible. The fully charged state shows the highest signal intensity, as mossy lithium has grown to its most saturated state in this cycle. As the battery discharges again, the signal decreases but remains higher than the initial state because some mossy lithium has accumulated on the metallic lithium surface. On the other side, the electrolyte region starts with the lowest signal intensity. Charging the battery causes lithium in the electrolyte to deposit onto the anode surface, forming a solid electrolyte layer, which appears as a small shoulder on the lower left of the peak. By the end of discharge, the electrolyte is fully reduced, and the solid electrolyte layer has formed, resulting in the highest signal intensity.

Figure 26. A one-dimensional spectrum of ^{7}Li collected during the charging process, categorized by color into two main regions: green (lithium metal) at 270 ppm and gray (electrolyte) at 0 ppm. The fitted data show lithium metal and mossy lithium on the sides, with the solid electrolyte interface and electrolyte on the right.

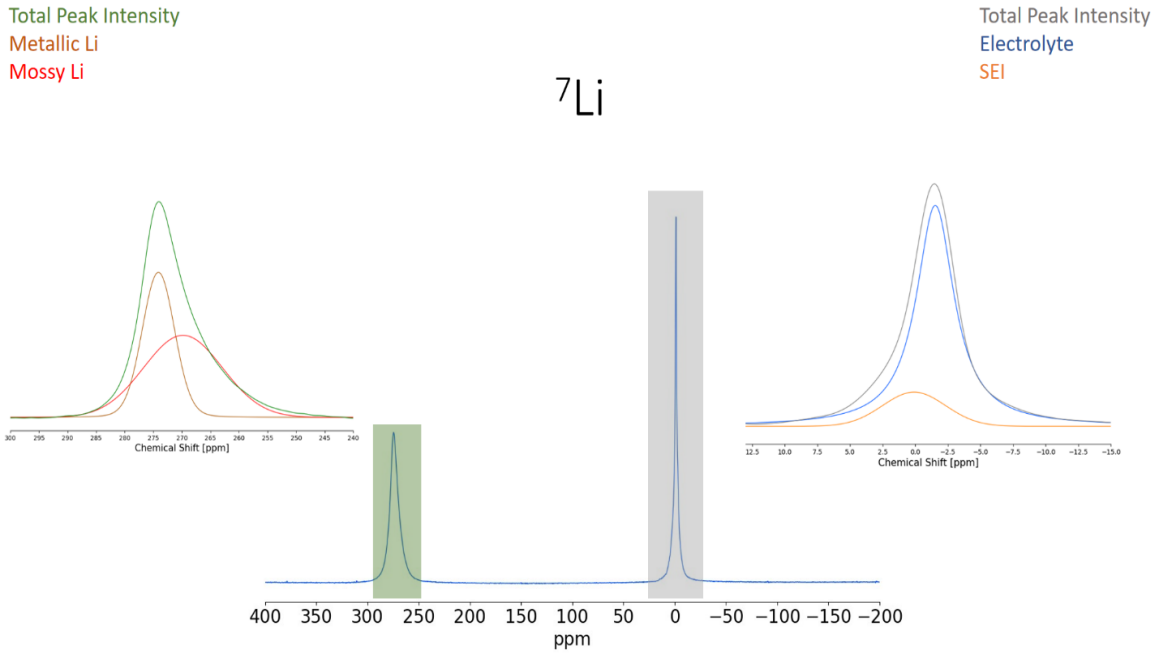

Figure 27. On the left is the one-dimensional spectrum of the lithium metal region peak at different stages of charge and discharge in the first cycle of the battery. The bottom left shows

the fitting of the mossy lithium morphology. On the right is the one-dimensional spectrum of the electrolyte region peak at different stages of charge and discharge in the first cycle of the battery.

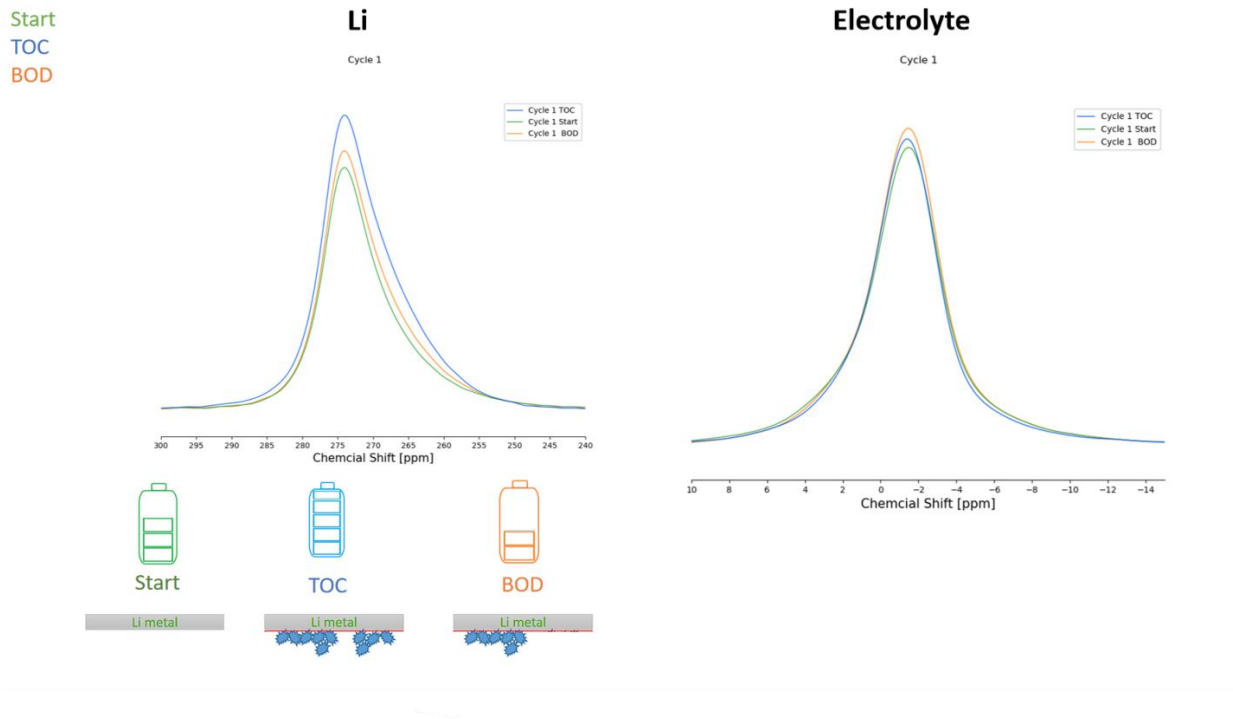

The quantification of changes in intensity across the ^{7}Li spectra show oscillatory behavior at both the Li-metal region and electrolyte region. The changes are small but measurable and indicate a breathing-mode behavior at both interfaces.

The assembly sequence of the battery is shown in Figure 28. Since there is no similar data model to refer to, lithium metal is used as the anode in the battery to help us obtain a quantitative reference from the initial NMR data. Taking Figure 29 as an example, this is a schematic diagram of the lithium metal peak region at the end of charging. The blue line represents the original data, and the black line represents the sum of the fitted green peak (originating from the lithium metal anode) and the red peak (originating from mossy lithium). The fitting result may have some degree of variation, but the fitting process is automatically completed on ssNake software using the multi-fit sequence designed by Alexander, ensuring the consistency of the fitting results. It can be seen from Figure 29 that mossy lithium forms on the

lithium metal anode during the charging phase, so we can observe the fitting result of the red peak 2, which is a Gaussian curve at 265 ppm, in the corresponding NMR slice. Similarly, Figure 30 shows the fitted data of the electrolyte region, where it can be seen that the integral of the fitting result mainly comes from the contribution of the electrolyte. Additionally, during the charging process, SEI forms, displayed as a Gaussian signal at 0 ppm.

Figure 28 shows the assembly sequence of the cartridge cell, with the electrolyte added between each layer.

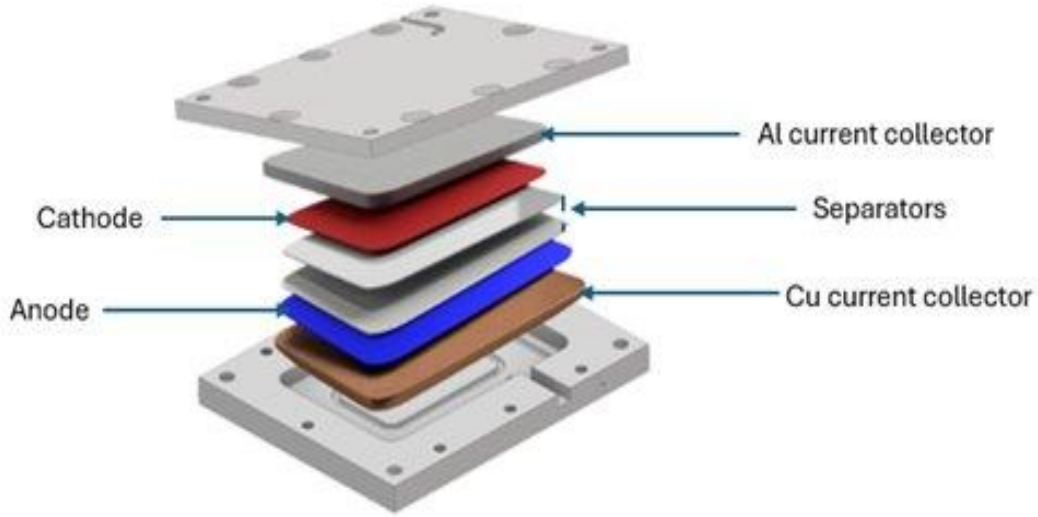

Figure 29 shows the ssNake fitting results for the lithium metal region. The signal of peak 1 (green) represents the lithium metal anode, while the signal of peak 2 (red) represents mossy lithium.

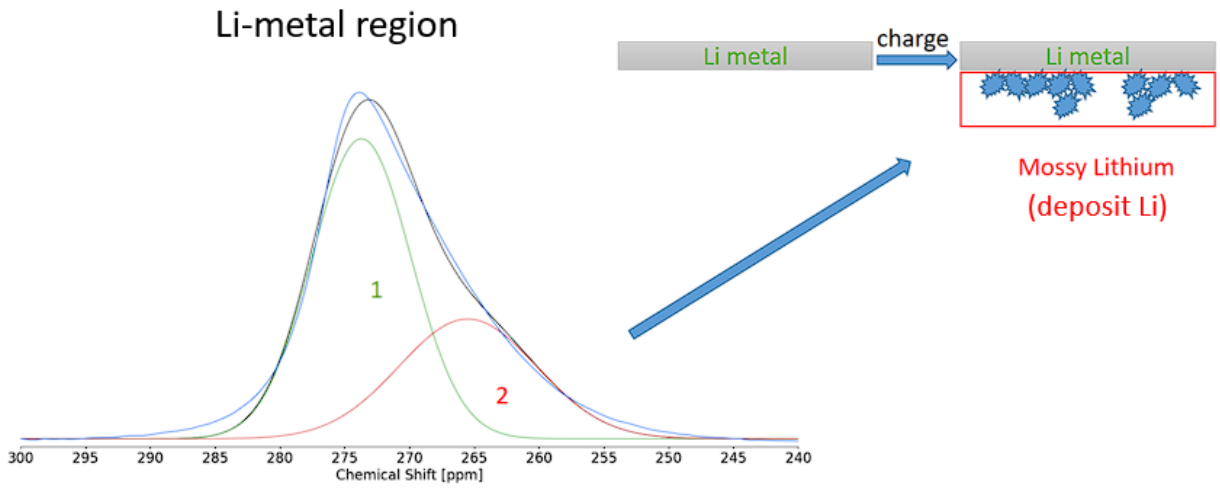

Figure 30 shows the ssNake fitting results for the electrolyte region. The signal of peak 1 (green) comes from the electrolyte, while peak 2 (red) represents the formed SEI.

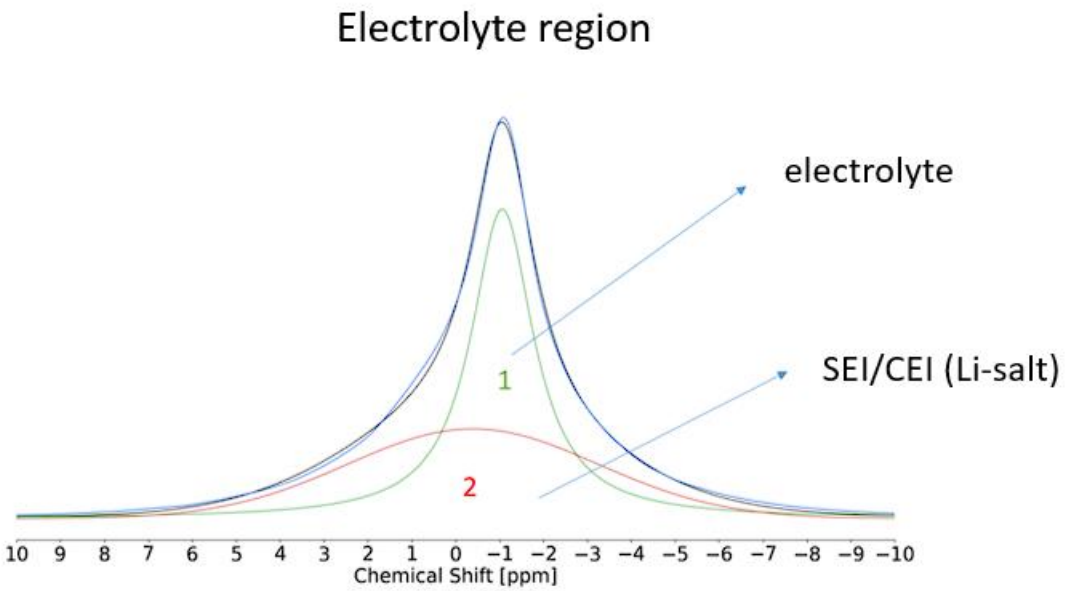

4.3.2 Fitting results

The experimental data are presented as comparative experiments. On the left side, the charging behavior of pulse discharge and the fitted data results on ssNake are shown, while on

the right side, the constant discharge is used as a control. Different colors of dashed lines are used in the images to mark the different charge and discharge phases to help distinguish the changes. Only the first five cycles are shown here, and it is clearly observed that the first two cycles behave differently from the last three cycles. Although both batteries underwent the same formation cycle before running the comparative tests, only the uniformly changing cycles 3, 4, and 5 are compared here. Under the fitted PD conditions, the change in the solid electrolyte layers (SEI + CEI) shows an overall downward trend in the fitting results. Therefore, different fitting parameters were used on ssNake, and the comparison results are as follows. The first set of tests used unchecked fitting parameters, while the second set used checked fitting parameters. The comparison shows that the results obtained with unchecked fitting parameters are more consistent with the experimental breathing patterns of SEI and CEI, and the experimental results are more uniform.

Figure 31. Two different fitting methods used during the fitting process. The first method, on the left, shows the trend of the curve with unlocked fitting coefficients. The second method, on the right, uses the average values from the first method's fitting data to fix the line width and chemical shift as constant coefficients for the fitting curve.

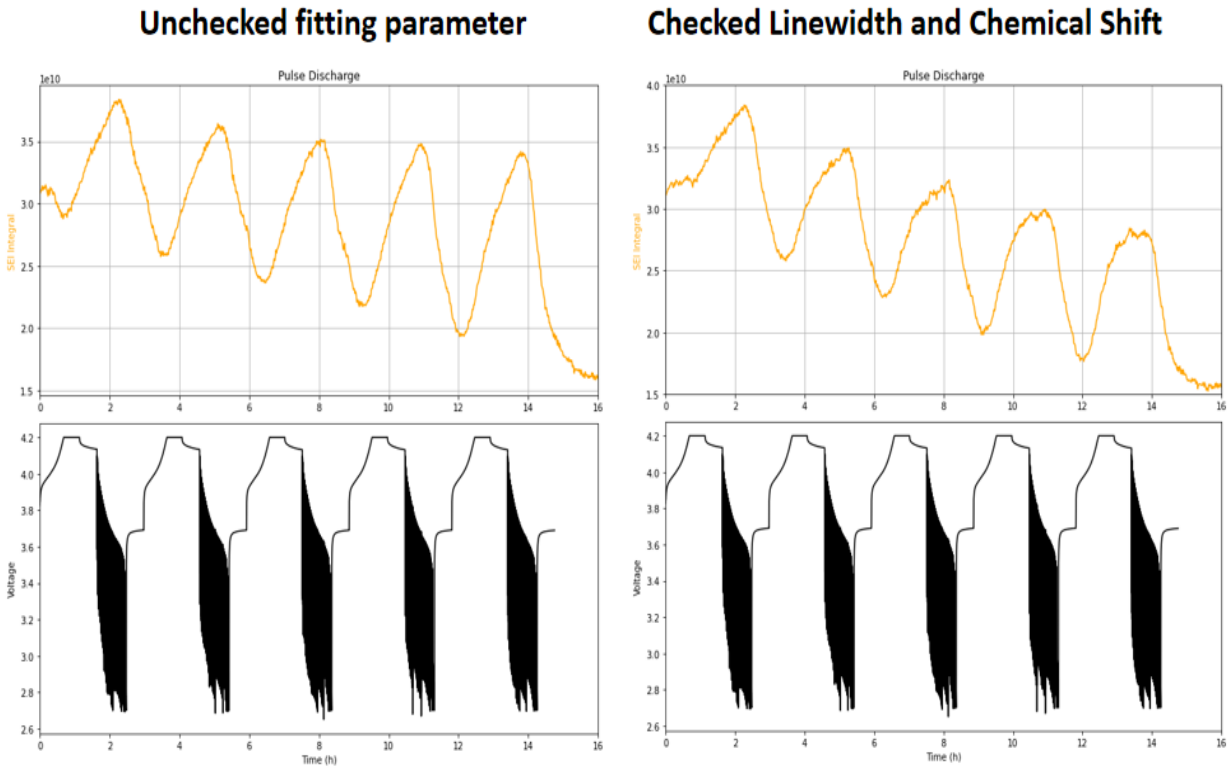

First, we observe the overall change in the peak of the entire -15 to 10 ppm region, which is designated as the electrolyte region peak. Although the electrolyte content of the two batteries was controlled to be the same during assembly, the degree of sealing of the batteries cannot be controlled. Therefore, this section focuses on observing the changes between cycles. Here, it is evident that the intensity changes of the two peaks under two discharge algorithms are synchronized. The blue dashed line represents the start of the discharge phase, where the integral starts to rise, consistent with the discharge phase where lithium ions are reduced into the electrolyte, and the amount of the generated solid layer tends to stabilize. The black solid line indicates the end of discharge, showing a trend where the integral begins to decrease on both sides. The magnitude of change is similar in both cases, approximately 0.1*E^11 on the vertical axis. This indicates that the substances that may be generated in the entire electrolyte region did not change significantly under the PD algorithm.

The second comparison is the electrolyte peak within the electrolyte region. This peak, as mentioned earlier, is a Lorentzian peak and occupies most of the signal in this region. By

observing the trend changes, this peak changes relatively uniformly in each cycle and can maintain the same integral after five cycles as at the start of the third cycle. Moreover, from a temporal perspective, the changes in the electrolyte are similar under both algorithms. The integral shows a downward trend at the beginning of charging and an upward trend at the beginning of discharging, consistent with the conventional behavior of the electrolyte during the charge and discharge phases of the battery.

The third comparison is the change in the solid electrolyte layers. Specifically, this Gaussian peak represents the total change in both SEI and CEI layers. The clear difference under the PD algorithm can be observed through the dashed line; before the end of the PD phase, the SEI and CEI layers already show a decreasing trend. In contrast, under the constant current method, the SEI and CEI layers reach a local maximum at the end of the discharge phase (followed by a decreasing trend as a rest period begins). This observed difference cannot currently be attributed specifically to changes in either CEI or SEI. What can be observed is that the PD discharge method results in greater overall changes in SEI and CEI between each cycle, but these changes can be reversed. Neither discharge method showed significant growth of the solid layers before the end of the first five cycles. The changes in these two solid layers are speculated to be the main difference brought about by the PD discharge method. If the PD discharge method can slow the growth rate of SEI and CEI, this might explain why battery life is extended.

Figure 32. The total integral curves of the fitted SEI and CEI under pulse discharge (left) and constant discharge (right) tests. The brown dashed lines indicate the start of each cycle from the third cycle onwards, the blue dashed lines represent the beginning of the discharge phase in each cycle, and the black solid lines denote the end of the discharge phase in each cycle.

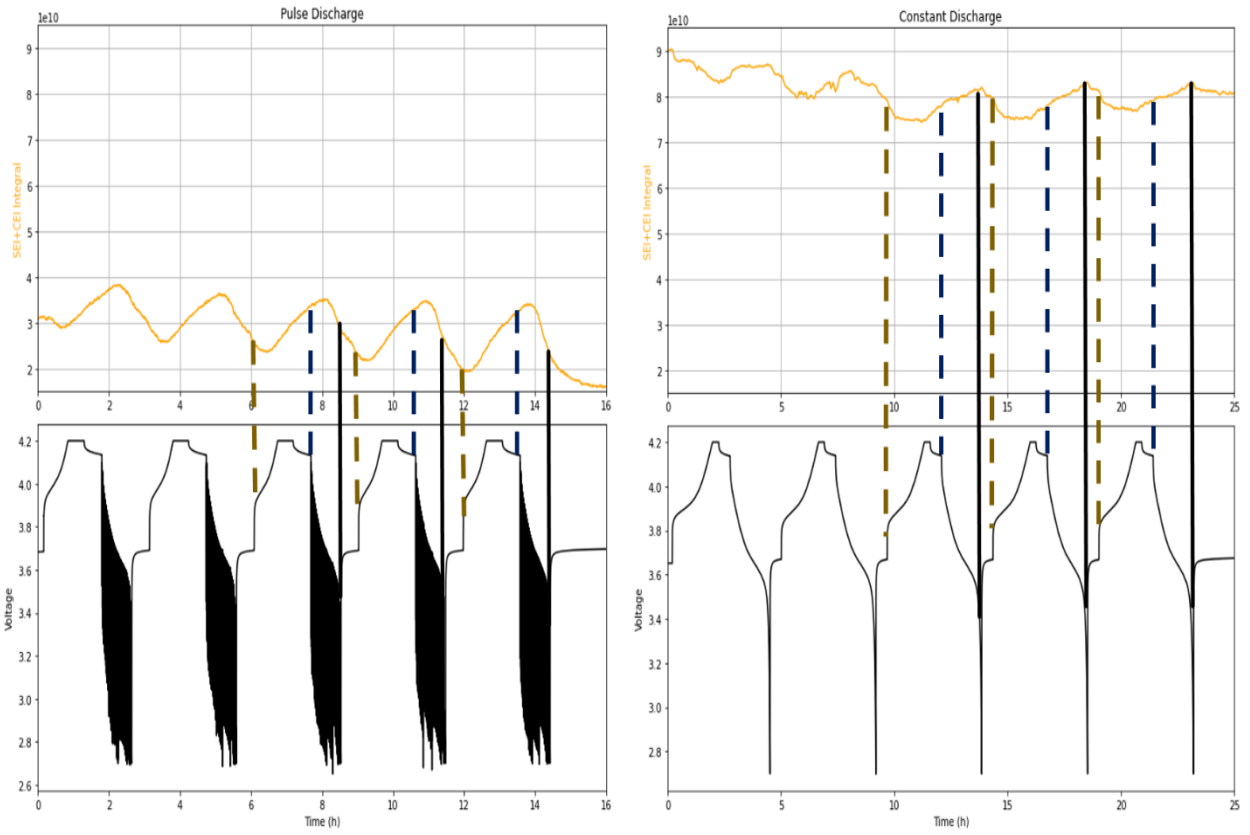

Fourth, the comparison is of the 250 to 290 ppm region, which is classified as the lithium region composed of anode metallic lithium and mossy Li formed on the lithium metal surface during cycling. It is evident that the peak integral changes in the lithium region are very uniform. Starting from the third cycle, the integral under both discharge environments increases with the start of charging, remains unchanged during the CV stage and rest stage, and begins to decrease with the start of discharge. The changes in integral on both sides are approximately 1.2-1.3*E^11.

The fifth comparison is of the changes in metallic lithium. It can be observed that from the start of the charging phase, the integral begins to increase, with a similar growth slope on both sides. However, the decrease in integral shows two stages: from the start of CV to the end of rest, both sides exhibit a relatively slow decline rate. With the beginning of the discharge phase, the integral rapidly decreases to the same level as at the start of the cycle by the end of the discharge phase.

Figure 33. The integral curves of the fitted lithium metal under pulse discharge (left) and constant discharge (right) tests. The brown dashed lines indicate the start of each cycle from the third cycle onwards, and the blue dashed lines represent the beginning of the discharge phase in each cycle.

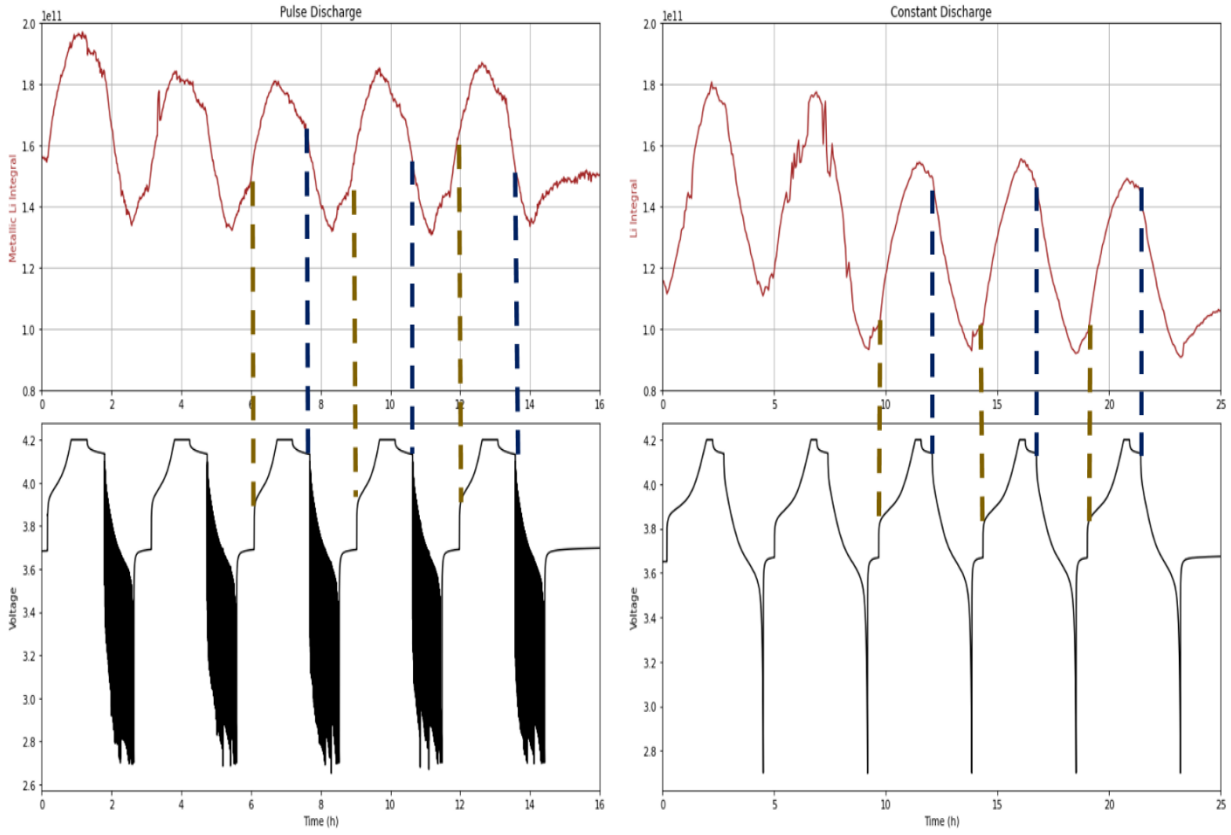

The sixth comparison is of the changes in mossy lithium. During the charging phase, lithium ions flow towards the metallic lithium (anode), forming the SEI layer and some mossy lithium. This growth trend continues until the beginning of the discharge phase. Under constant conditions, the growth and decay rates are the same, and the beginning of the discharge phase coincides with the local maximum of the integral. By the end of each cycle, the mossy lithium can be completely reduced. The difference under PD conditions is that there is a noticeable segment with a different growth rate starting from the CV stage, and at the end of each cycle, a small portion of mossy lithium remains unreduced.

Figure 34. The integral curves of the fitted mossy lithium under pulse discharge (left) and constant discharge (right) tests. The brown dashed lines indicate the start of each cycle from the third cycle

onwards, and the blue dashed lines represent the beginning of the discharge phase in each cycle.

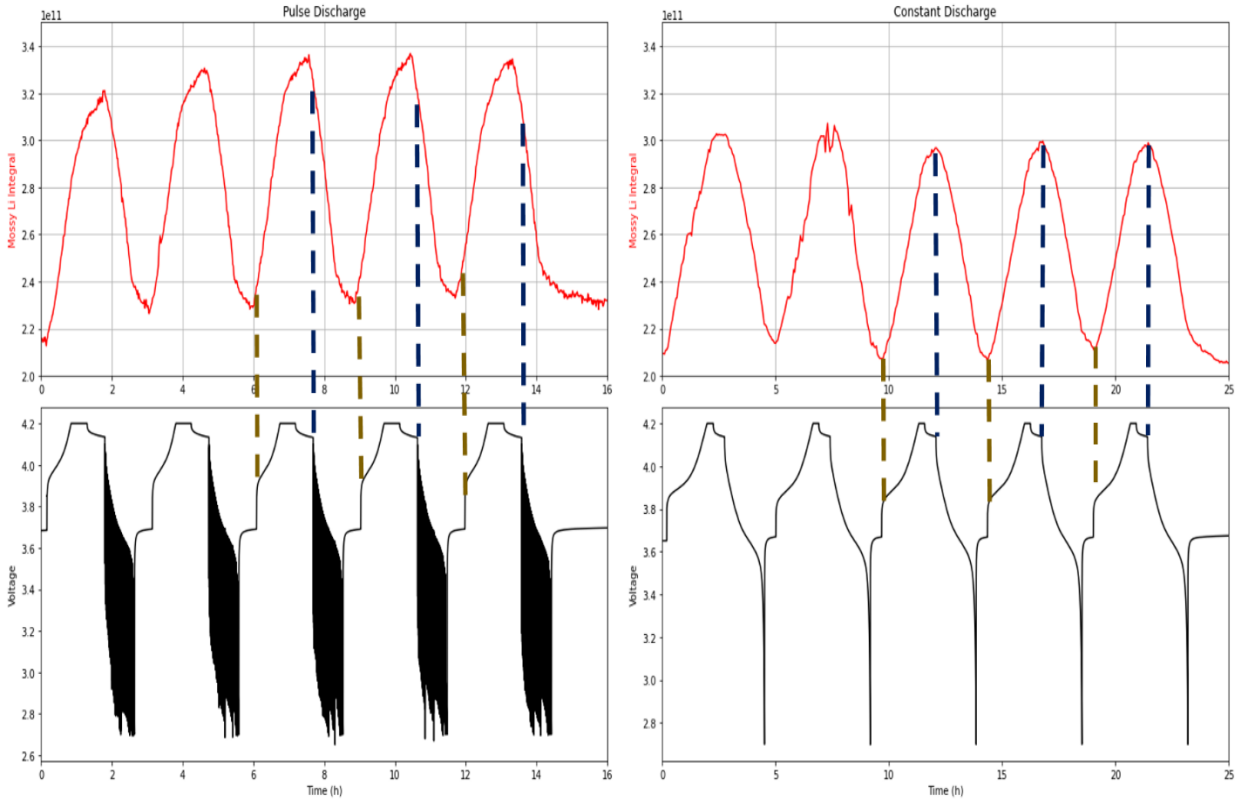

In summary, pulse discharging did not show significant changes in the first five cycles of the battery. As shown in the table, the degree of change in each fitting parameter is similar under the two different discharge conditions. The formula used to calculate the change in integral compares the percentage change from the beginning of cycle 3 to the end of cycle 5.

$$\text{Integral changes} = \frac{(Cycle\ 5\ BOD\ Integral - Cycle\ 3\ Start\ Integral)}{Cycle\ 3\ Start\ Integral} * 100\% \qquad (4.1)$$

The reason for comparing only the last three cycles is that during the *operando* experiments, the battery might produce phase-shifted signals due to the strong magnetic field and pulse, or unstable electrochemical performance collected by Gamry1000 while cell is in the magnet. Because the performance from the third cycle to the fifth cycle was relatively stable, it was used as a reference.

It is noteworthy that the two peaks fitted by the Gaussian function belong to products generated during the charge and discharge cycles and should exhibit breathing behavior (formation and reduction) during the battery cycle. However, in the case of pulse discharge, a small amount of mossy lithium deposition can be observed, and the overall trend of SEI and CEI is decreasing. It is speculated that this is related to the formation and changes in CEI; however, another set of control experiments is needed to verify this.

Content	Constant Charge (NMC 532 vs. Li)			Pulse Discharge (NMC 532 vs. Li)			Difference
	Trend	Between cycles	Integral changes	Trend	Between cycles	Integral changes	
Total peak Integral	CV start to Discharge finish ↑	Uniform changes	+3%	CV start to 2nd PD step finish ↑	Uniform changes	0%	similar
Electrolyte Integral	Charge ↓ Discharge ↑	Uniform changes	+1%	Charge ↓ Discharge ↑	Uniform changes	+3%	similar
Metallic Li Integral	Charge ↑ Discharge ↓	Uniform changes	-12%	Charge ↑ Discharge ↓	Uniform changes	0%	similar
Mossy Li Integral	Charge ↑ Discharge ↓	Uniform changes	+6%	Charge ↑ Discharge ↓	Uniform changes	+2%	similar

Table 12. Summary of the fitting results trends for all components in the cartridge cell during the charge-discharge process, including the behavioral changes between cycles and the calculated percentage change in the integral.

Although the *operando* cell only shows data for 5 cycles here, the battery life can be maintained for a longer period. During the OCV rest stage after the five cycles, each fitted component exhibited a very stable level over these several hours. The electrolyte level remained stable, and in the test, the cartridge cell under constant current testing was left in the magnet for 16 hours without any significant fluctuations in signal intensity or voltage. Additionally, the Coulombic efficiency of the battery during the charge-discharge cycles was also relatively stable.

Figure 35. Cycles 6-21 under pulse discharge testing, showing that the battery still maintains normal charge and discharge.

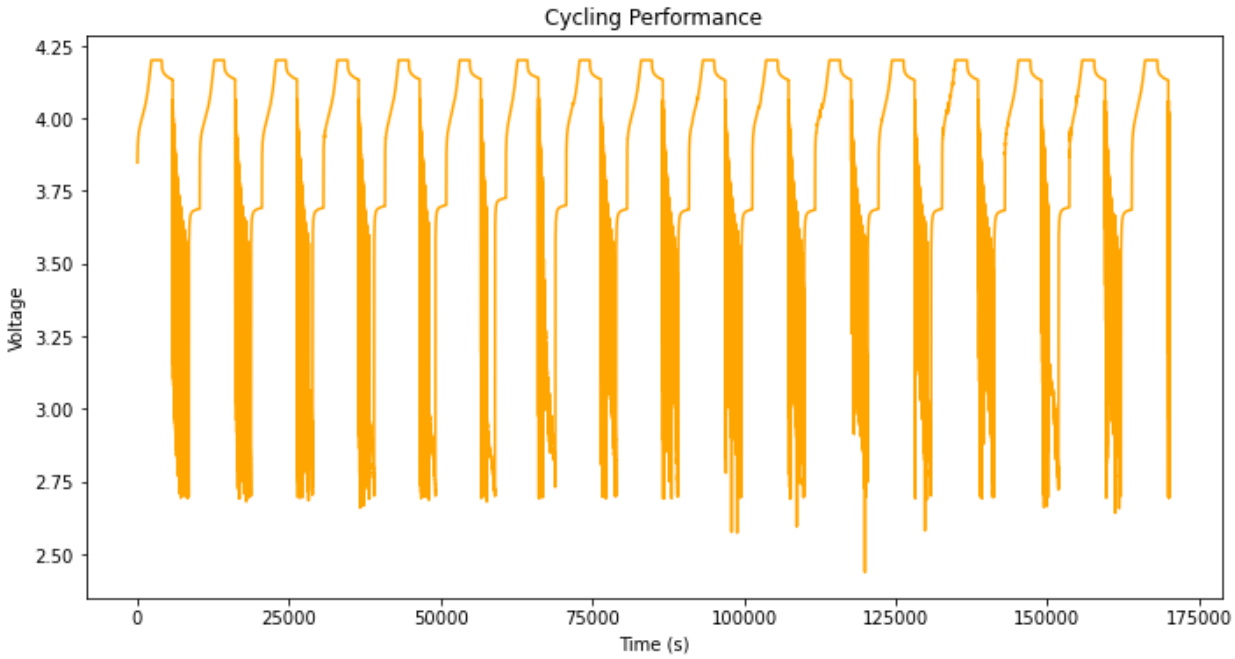

Figure 36. The performance of the cartridge cell during OCV rest after five cycles, showing stable voltage

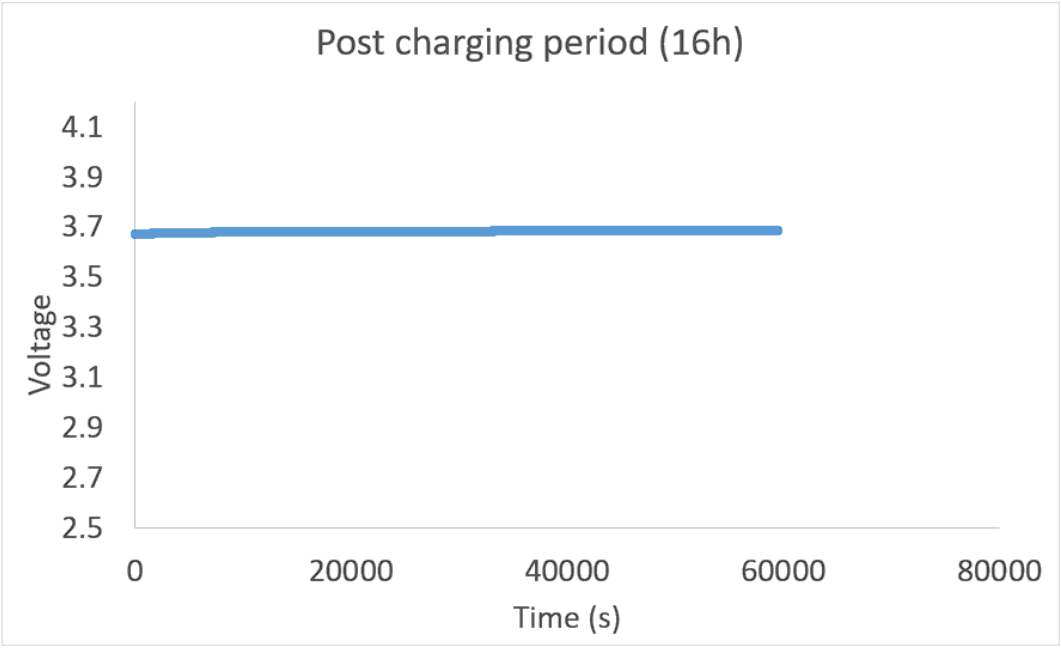

Cycle number	Charge capacity (mAh)	Discharge capacity (mAh)	Coulombic Efficiency
1	6.27	5.18	82.5%
2	5.97	5.89	98.6%
3	5.68	5.20	91.5%
4	5.25	5.23	99.6%
5	5.25	5.23	99.6%
6	5.24	5.24	99.8%
7	5.24	5.24	100.0%
8	5.16	5.20	100.9%
9	5.23	5.21	99.5%
10	5.21	5.20	99.9%
11	5.18	5.17	99.8%
12	5.11	5.09	99.6%

.

Table 13. The charge and discharge capacities of each cycle and the Coulombic efficiency of the cartridge cell during constant current discharge testing.

4.4 Reference

66. Komaba, S., Kumagai, N. & Kataoka, Y. *Influence of Manganese(II), Cobalt(II), and Nickel(II) Additives in Electrolyte on Performance of Graphite Anode for Lithium-Ion Batteries*. *Electrochimica Acta* vol. 47 www.elsevier.com/locate/electacta (2002).

67. Allen, J. P., O'Keefe, C. A. & Grey, C. P. Quantifying Dissolved Transition Metals in Battery Electrolyte Solutions with NMR Paramagnetic Relaxation Enhancement. *The Journal of Physical Chemistry C* (2023) doi:10.1021/acs.jpcc.3c01396.

68. Burlamacchi, L. & Tiezzi, E. *PROTON SPIN RELAXATION TIMES (Tt; T2) AND Mn Z+ COMPLEXES IN SOLUTION: PMR AND PULSED NMR STUDIES**. vol. 31 (1969).

69. Böttjer, T., Lehmann, G. & Stockhausen, M. *An Electron Paramagnetic Resonance Study of Mn 2 + Ions Doped in Langbeinites The Cubic (High Temperature) Phase of Some Langbeinites, A 2 B 2 + (S0 4) 3 with 11 Different Combi-Nations of A and B Type Cations, Doped with Mn 2+*. *Z. Naturforsch* vol. 47 (1992).

70. Furman, G. B., Goren, S. D., Meerovich, V. M. & Sokolovsky, V. L. Dipolar nuclear polarization via the spin diffusion of a dipole order. *Journal of Magnetic Resonance* **320**, (2020).

71. Krachkovskiy, S. A., Foster, J. M., Bazak, J. D., Balcom, B. J. & Goward, G. R. *Operando* Mapping of Li Concentration Profiles and Phase Transformations in Graphite Electrodes by Magnetic Resonance Imaging and Nuclear Magnetic Resonance Spectroscopy. *Journal of Physical Chemistry C* **122**, 21784–21791 (2018).

72. McShane, E. J., Bergstrom H., *et al.* Quantifying Graphite Solid-Electrolyte Interphase Chemistry and its Impact on Fast Charging. *ACS Energy Lett* **7**, 2734–2744 (2022).

73. Liu, J. & Wang, X. Investigating effects of pulse charging on performance of Li-ion batteries at low temperature. *J Power Sources* **574**, (2023).

74. Liu, G. & Lu, W. A Model of Concurrent Lithium Dendrite Growth, SEI Growth, SEI Penetration and Regrowth. *J Electrochem Soc* **164**, A1826–A1833 (2017).

75. Sanders, K. J., Ciezki, A. A., Berno, A., Halalay, I. C. & Goward, G. R. Quantitative *Operando* 7Li NMR Investigations of Silicon Anode Evolution during Fast Charging and Extended Cycling. *J Am Chem Soc* **145**, 21502–21513 (2023).

76. Van Meerten, S. G. J., Franssen, W. M. J. & Kentgens, A. P. M. ssNake: A cross-platform open-source NMR data processing and fitting application. *Journal of Magnetic Resonance* **301**, 56–66 (2019).

77. Sanders, K. J., Aguilera A., Keffer J *et al.* Transient lithium metal plating on graphite: *Operando* 7Li nuclear magnetic resonance investigation of a battery cell using a novel RF probe. *Carbon N Y* **189**, 377–385 (2022).

Chapter5

Outlook

5.1 Summary & Conclusion

The entire work mainly focuses on testing the performance of point batteries using nuclear magnetic resonance and electrochemical measurement instruments. Manganese ions are given attention due to their significant negative impacts on batteries. With increasing demands for efficiency and durability in batteries, manganese ions, which can form as efficiency contaminants after prolonged charging, are particularly important. This study only preliminarily analyzes the impact of manganese ions on the electrolyte, though transition metals like manganese can also harm other components of the battery.

Chapter 3 primarily discusses the use of PFG-NMR (^{7}Li) to test the effects of different concentrations of manganese ions on the diffusion coefficient of lithium in the electrolyte. The study tested two concentrations, 0.01 M and 0.05 M, based on the possible concentrations of manganese ions that might occur in the battery, and controlled within measurable T1 and T2 relaxation times. Results showed, as hypothesized, that manganese ions cause a decrease in the diffusion coefficient of the electrolyte, and this trend becomes more pronounced with increasing concentration. Charge and discharge tests were also conducted using these two groups of electrolytes, and results indicated that 0.05 M of contaminants hinder the battery's charge and discharge cycles. This experiment also tested the diffusion coefficient of the battery before and after charging and discharging at room temperature. For the uncontaminated electrolyte, the diffusion coefficient decreased by 6% before and after charging and discharging, while with 0.01 M manganese ions, the battery could still charge successfully, but the diffusion coefficient decreased more significantly (25%) after successful charging. Both sets of experimental data demonstrate that manganese ions compete with lithium ions in the electrolyte, and this competition becomes more evident after charging and discharging. This chapter also discusses other tested transition metals, copper ions and iron ions. Experimental data show that iron ions

may have similar effects to manganese ions, but copper ions cause significant decreases at a concentration of 0.01 M. It was observed in temperature variation experiments that the introduction of the three transition metals did not change the activation energy of lithium diffusion, so the effects of copper ions need further research, and the stable oxidation state of iron ions in the electrolyte also requires further discussion. In the context of electrochemistry, in environments containing manganese ions, high concentrations of manganese ions have shown a significant drop in discharge capacity within the first 10 cycles. In contrast, 0.01 M manganese ions do not cause noticeable changes in discharge capacity.

Chapter 4 mainly describes the design of cartridge cells for *operando* experiments. This allows the transition from only discussing the electrolyte to observing the entire battery components. The testing began with collecting the constant current charge and discharge performance of lithium metal as the anode. The collected experimental data (NMR and electrochemical) serve as reference data for all subsequent tests. A control experiment was conducted to test the effects of pulse discharge on the battery. Comparative reference data showed that within the first five charge-discharge cycles, pulse discharge did not significantly affect the electrolyte and lithium metal. However, it showed different growth rates of mossy lithium during constant voltage charging compared to constant current periods; the impact on CEI and SEI was reflected in the discharge phase, where constant current discharge initially caused the integral to decrease, while pulse discharge showed an initial rise then a decrease. Both experiments indicated that pulse discharge alters the battery's morphology. Further experiments are needed to refine the impact of pulse discharge on SEI and CEI separately. *Operando* experimental data demonstrated the stability of the cartridge in half-cell tests, but testing transition metal manganese ions under this setup still poses challenges due to paramagnetic effects that may cause bulk magnetic susceptibility shifts (BMS), leading to displacement and broadening of measured components during testing.

5.2 Future Plan

The impact of transition metal manganese on the electrolyte is just one aspect; its effect on the solid electrolyte interface (SEI) is also worth discussing. Additionally, the protective mechanisms against manganese ion dissolution are a promising area for further research. It is currently understood that crown structure complex compounds can mitigate the dissolution of manganese ions and show benefits in electrochemical performance, but their impact on the diffusion coefficient has not been discussed. Moreover, the oxidation state of manganese ions varies under different conditions. X-ray microscopes might be helpful in testing oxidation states, as this technology could track and quantify the changes in the oxidation states of trivalent and divalent manganese ions. On the other hand, for *operando* experiments, the observed changes in CEI (cathode electrolyte interface) and SEI can be initially studied by altering the upper cutoff voltage during testing to observe CEI variations. Different upper cutoff voltages might change the growth of CEI during the discharge process. Similarly, for discussing solid-state electrolyte interfaces, X-ray tomography could potentially observe changes before and after experiments. This technology can visualize the thickness of the anode and possibly the formation of mossy lithium. The application of manganese ion-containing electrolytes in *operando* experiments still poses challenges and requires further testing to demonstrate feasibility.

Appendix

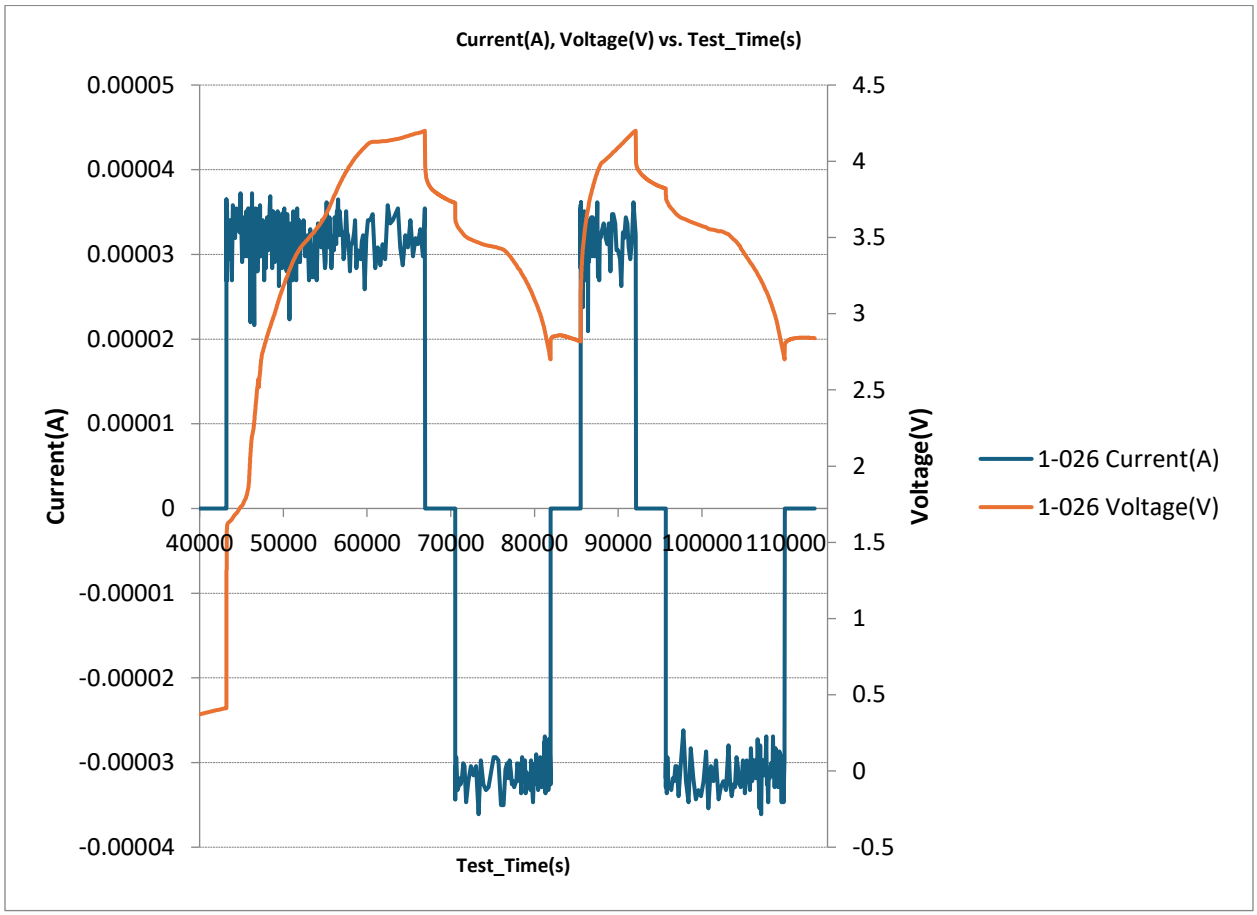

Appendix Figure 1 0.01M Mn-additive electrolyte charging and discharging cycle performance with C-rate C/20

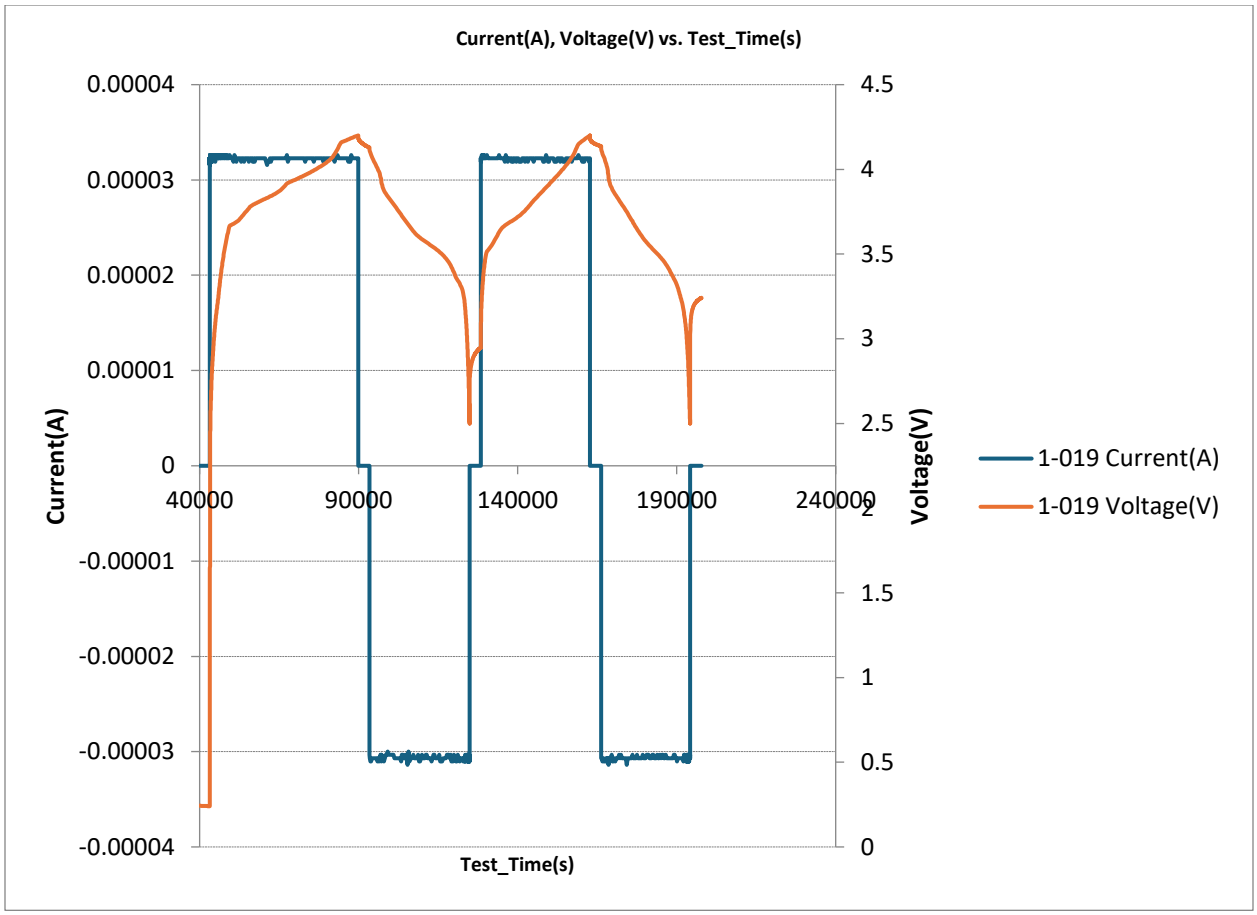

Appendix Figure 2 Reference electrolyte charging and discharging cycle performance with C-rate C/20